Wind profiles from dual-Doppler lidar in the complex terrain around Stuttgart

Master Thesis in Meteorology
by

Niklas Wittkamp

August 2019

INSTITUTE FOR METEOROLOGY AND CLIMATE RESEARCH
KARLSRUHE INSTITUTE OF TECHNOLOGY (KIT)

Advisor:	Prof. Dr. Christoph Kottmeier
Second Advisor:	Prof. Dr. Michael Kunz

Abstract

The flow in the atmospheric boundary layer (ABL) over cities is crucial for the urban climate, as it can reduce concentrations of emitted air pollutants and heat by ventilation. Especially over cities in orographically structured terrain the wind field in the ABL is a complex interaction between processes on the large scale, mesoscale and microscale. The city of Stuttgart in southern Germany is a good example for a city where bad air quality is linked to the topography. Stuttgart is located in a valley basin, which is joined by a narrow valley and opens to the larger Neckar valley. This thesis aims to determine characteristic flow features in the ABL around Stuttgart and to investigate how the flow features depend on the large scale wind and atmospheric stratification. The analysis is mainly based on wind measurements by dual-Doppler lidar. Applying the virtual tower (VT) technique, vertical profiles of the horizontal wind are retrieved at 6 positions in the Neckar valley and at the opening of the Stuttgart basin, on 36 days in summer 2017. The observational data set is complemented by a profiling Doppler lidar, a microwave radiometer, a ceilometer and near-surface measurements as well as radiosoundings. This is the first time that the three-dimensional distribution of the wind in the ABL near Stuttgart is analysed in detail using observational data. Also it is the first time that the VT technique is applied to investigate the wind field in orographically complex, urban terrain. Another aim of this thesis is therefore to prove the applicability of the VT technique under such conditions.

To obtain reliable wind information, an intense processing and quality control is necessary, which leads to the removal of 28 % of the raw data, and yields horizontal wind vectors at the 6 VTs for 9 to 16 height levels at a temporal resolution of around 15 min. For a statistical analysis hourly averages are calculated to reduce temporal variability.

In a case study under fair weather conditions the flow is found to be coupled throughout the convective boundary layer (CBL) during daytime, while during nighttime in the stable boundary layer (SBL) a decoupling of the flow above and below the mean ridge height is observed. Above the ridge height a low-level jet is observed with similar strength and wind direction at all locations. Below the ridge height a strong thermally driven down-valley wind forms in the Neckar valley, while a weak outflow from the Stuttgart basin into the Neckar valley is observed. The influence of the topography on the horizontal wind field is further analysed statistically for the whole measurement period, using all available VT measurements combined with temperature and humidity measurements from the microwave radiometer. For the statistical analysis two height levels are chosen for all VTs, one to represent the topographically influenced wind below the ridge height and the other one representing the ambient wind above. A coupling of the flow below and above the mean ridge height under convective conditions and a decoupling under stable conditions was observed as a characteristic feature at all locations for the whole period. The occurrence and degree of coupling and decoupling is found to be strongly depending on the bulk Richardson number. The analysis suggests a critical bulk Richardson number of around 1.25. For lower bulk Richard-

son numbers, the flow is coupled due to buoyancy-driven or shear-driven turbulence. For bulk Richardson numbers higher than 1.25, the low-level wind is decoupled from the ambient wind.
This thesis demonstrates that the VT technique can be used over complex urban terrain to obtain high quality horizontal wind profiles, which can be used to study the temporal evolution of the horizontal wind field. This data set can also be used to evaluate high resolution urban climate models. Down-valley winds are a common phenomenon in the area around Stuttgart, which probably are important for the ventilation of the city under stable stratification. They are likely to play an important role for the urban climate, as they can reduce pollutant concentrations in the city during nighttime.

Zusammenfassung

Die Strömung in der atmosphärischen Grenzschicht in Städten ist entscheidend für das Stadtklima, da sie die Konzentrationen von Luftschadstoffen und Wärme durch Belüftung reduzieren kann. Insbesondere in Städten in orografisch gegliedertem Gelände ist das Windfeld in der atmosphärischen Grenzschicht eine komplexe Wechselwirkung zwischen Prozessen auf großer Skala, Meso- und Mikroskala. Stuttgart in Süddeutschland ist ein gutes Beispiel für eine Stadt, in der schlechte Luftqualität eng mit der Topographie verknüpft ist. Stuttgart liegt in einem Talkessel, in welchen ein enges Tal mündet und der sich zum größeren Neckartal öffnet. Diese Arbeit zielt darauf ab, charakteristische Strömungsmerkmale in der atmosphärischen Grenzschicht um Stuttgart zu bestimmen und zu untersuchen, wie die Strömungsmerkmale vom großräumigen Wind und der atmosphärischen Schichtung abhängen. Die Analyse basiert hauptsächlich auf Windmessungen mit Dual-Doppler Lidar. Mithilfe der Methode der virtuellen Masten, werden vertikale Profile des horizontalen Windes im Neckartal und an der Öffnung des Stuttgarter Kessels im Sommer 2017 an 6 Positionen und 36 Tagen gewonnen. Der Beobachtungsdatensatz wird durch ein Profile messendes Doppler Lidar, ein Mikrowellenradiometer, ein Ceilometer und Bodennahe Messwerte sowie Radiosonden ergänzt. Erstmals wird die dreidimensionale Verteilung des Windes in der atmosphärischen Grenzschicht bei Stuttgart anhand von Beobachtungsdaten detailliert analysiert. Außerdem ist es auch das erste Mal, dass die Methode der virtuelle Masten zur Untersuchung des Windfeldes in orographisch komplexem, urbanem Gelände eingesetzt wird. Ein weiteres Ziel dieser Arbeit ist es daher, die Anwendbarkeit der virtuellen Masten Methode unter solchen Bedingungen zu zeigen.

Um zuverlässige Windinformationen zu erhalten, ist eine intensive Verarbeitung und Qualitätskontrolle erforderlich. Diese führt zur Entfernung von 28 % der Rohdaten und ergibt horizontale Windvektoren an den 6 virtuellen Masten auf jeweils 9 bis 16 Höhenstufen, bei einer zeitlichen Auflösung von etwa 15 min. Für eine statistische Analyse werden Stundenmittelwerte berechnet, um die zeitliche Variabilität zu reduzieren.

In einer Fallstudie unter Schönwetterbedingungen wird festgestellt, dass die Strömung tagsüber in der konvektiven Grenzschicht gekoppelt ist, während nachts in der stabilen Grenzschicht eine Entkopplung der Strömung über und unter der mittleren Grathöhe des umgebenden Geländes beobachtet wird. Oberhalb der Grathöhe wird an allen Positionen ein Grenzschichtstrahlstrom (Low-Level Jet) mit ähnlicher Stärke und Windrichtung beobachtet. Unterhalb der Grathöhe bildet sich im Neckartal ein starker thermisch angetriebener Talabwind aus, während ein schwacher Abfluss aus dem Stuttgarter Becken in das Neckartal beobachtet wird. Der Einfluss der Topographie auf das horizontale Windfeld wird weitergehend für den gesamten Messzeitraum statistisch analysiert, wobei alle verfügbaren Messungen an virtuellen Masten in Kombination mit Temperatur- und Feuchtigkeitsmessungen des Mikrowellenradiometers verwendet werden. Für die statistische Analyse werden für alle virtuellen Masten zwei Höhenstufen gewählt, eine zur Darstellung des topographisch beeinflussten Windes unterhalb der Grathöhe und die andere zur Darstellung des

Umgebungswindes darüber. Eine Kopplung der Strömung unterhalb und oberhalb der mittleren Grathöhe unter konvektiven Bedingungen und eine Entkopplung unter stabilen Bedingungen wurde als charakteristisches Merkmal an allen Standorten für den gesamten Zeitraum beobachtet. Das Auftreten und der Grad der Kopplung und Entkopplung ist stark abhängig von der Bulk-Richardson-Zahl. Die Analyse deutet auf eine kritische Bulk-Richardson-Zahl von etwa 1,25 hin. Bei niedrigeren Richardson-Zahlen wird die Strömung aufgrund von auftriebs- oder schergetriebenen Turbulenzen gekoppelt. Bei Bulk-Richardson-Zahlen größer als 1,25 ist der Wind auf der niedrigeren Höhe vom Umgebungswind entkoppelt.

Diese Arbeit zeigt, dass die Methode der virtuellen Masten über komplexem städtischen Gelände verwendet werden kann, um qualitativ hochwertige Profile des Horizontalwindes zu erhalten, die verwendet werden können, um die zeitliche Entwicklung des horizontalen Windfelds zu untersuchen. Dieser Datensatz kann auch zur Evaluation hochauflösender Stadtklimamodelle verwendet werden. Talabwinde sind im Raum Stuttgart ein häufiges Phänomen, das wahrscheinlich für die Belüftung der Stadt unter stabiler Schichtung wichtig ist. Sie spielen wahrscheinlich eine wichtige Rolle für das Stadtklima, da sie die Schadstoffkonzentration in der Nacht reduzieren können.

Contents

1 Introduction

Cities are centres of human population and activity, therefore emissions of atmospheric pollutants and heat can be intense. Especially cities located in mountainous terrain often suffer from bad air quality. This is associated with the complex flow in the urban atmospheric boundary layer (ABL), which is influenced by processes ranging from the large scale down to the microscale. They include synoptic scale pressure systems, mesoscale topographic and thermal effects, and microscale influences from buildings and human activities (Steyn et al., 2013). The flow conditions in the urban boundary layer (urban ABL) are crucial for the living conditions in cities, because they control the ventilation, and thereby immissions of pollutants and heat.

Atmospheric processes and flow over urban areas in complex terrain have been investigated previously in field experiments and numerical model studies. Among others, observational studies have been conducted in the Lower Fraser Valley in Canada, in the Upper Rhine Valley in Germany, and in the Salt Lake City Valley in the USA: Steyn et al. (1997) investigated Ozone and pollutants in the Lower Fraser Valley and found that the dominating pollutant types differ in winter- and summertime. Pollutants are distributed in the area by a complex circulation in the urban ABL influenced by interactions between the close-by sea, mountains and the city. In the Upper Rhine Valley the effects of the topography on the structure of the ABL and the dispersion of pollutants was examined. Kalthoff et al. (1998) investigated the diurnal and spatial variation of the ABL and found that during daytime, the height of the convective boundary layer (CBL) in complex terrain follows the underlying orography and that pollutant concentrations are strongly dependent on the CBL height. Kossmann et al. (1998) analysed the CBL structure in the area of the transition from the broad Rhine Valley to the mountains of the northern Black Forest. They found a terrain following height of the CBL in the morning, but in the course of the day large scale advection as well as mesoscale mountain slope flows influenced the CBL, so that in the afternoon the CBL height was rather homogeneous and did not follow the terrain any more. In the Salt Lake City Valley, a densely populated area bordered by the Great Salt Lake on one side and surrounded by mountain ranges, the complex interaction between processes on the different scales was investigated during tracer experiments (e.g. Allwine et al., 2002), and the accumulation of pollutants and flow interactions during persistent stable wintertime conditions have been studied in a large field campaign (Lareau et al., 2013). All these studies examined ABL processes above and around cities located in broad valleys of widths on the order of 20 km and more. Up to now observational studies in narrow, densely populated valleys with a complex topographic structure are rare.

Reliable knowledge on the urban climate is crucial for sustainable urban development in times of climate change and air pollution issues. Nowadays urban climate models are being developed, which are able to resolve whole cities down to single buildings (Scherer et al., 2019b). These numerical models can be a highly valuable tool for city planners and politicians to assess the impacts of new buildings or neighbourhoods on the urban climate, or to cope with existing problems of

bad air quality and heat stress. To evaluate high-resolution urban climate models, highly resolved comprehensive observational data of temperature, humidity and wind in the ABL are necessary amongst others. Due to the importance for ventilation, wind measurements with high temporal and spatial resolution are particularly important. This issue is currently addressed by the large project $[UC]^2$ - Urban Climate Under Change, funded by the German Federal Ministry of Education and Research (BMBF) (Scherer et al., 2019b). The aims of the project are to develop the building resolving urban climate model PALM-4U (Maronga et al., 2019) and to gather comprehensive three-dimensional observational data to validate and test the model (Scherer et al., 2019a).

The possibilities of observing the wind field in the ABL by traditional in-situ measurements, like anemometers mounted on measurement towers or tethered balloons are rather limited in urban areas, with regard to spatial coverage, positioning and expenses. The CBL reaches an average height of 1 km to 2 km above the ground (e.g. Stull, 1988), i.e. in particular during daytime, large parts of the ABL are very challenging to be monitored using in-situ methods. Barlow (2014) states that "the upper 90 % of the UBL [(urban ABL)] (mixed and residual layers) remains under-researched". This gap can be closed using remote sensing techniques like Doppler lidar. Single Doppler lidar devices are able to provide wind vector profiles, if the flow can be assumed to be horizontally homogeneous. However, this assumption does not generally apply over complex terrain (Bingöl et al., 2009). Considerably more accurate horizontal wind information in complex flow can be retrieved combining two Doppler lidar devices using the dual-Doppler method (Pauscher et al., 2016; Choukulkar et al., 2017). The dual-Doppler lidar method was first applied by Rothermel et al. (1985), who showed the general applicability of the method and found good agreement with other measurements. The method was developed further in recent years. Newsom et al. (2005), Drechsel et al. (2009) and Träumner et al. (2015) used retrieval algorithms to get wind fields from intersecting Doppler-lidar scans. Collier et al. (2005) and Röhner and Träumner (2013) measured two-dimensional turbulence using dual-Doppler lidar and received good results for both flat urban terrain and inhomogeneous agricultural terrain. Stawiarski et al. (2013) conducted an extensive error analysis, showing opportunities and limitations of Doppler-lidar measurements.

Vertical profiles of the horizontal wind can be obtained from dual-Doppler lidar measurements, with the so-called virtual tower (VT) technique. The VT technique was first used by Calhoun et al. (2006) who measured continuous profiles of the mean horizontal wind over Oklahoma City, a city in flat terrain in the USA. Damian et al. (2014) observed a low-level jet over flat agricultural area in the Rhine Valley and found a good agreement of the VT measurements with measurements from a meteorological mast and a tethered-balloon probe. Newman et al. (2016) showed that the VT technique achieves better results than single profiling lidar measurements in homogeneous terrain in the Great Plains in the US. The VT technique has considerable advantages over traditional in situ measurements: vertical profiles can be measured from close to the ground up to the boundary layer top, VTs can be freely positioned within the limitations by the instrument setup geometry, they are applicable in densely built-up areas, as well as in complex terrain and as a remote sensing technique they do not disturb the flow. However, to retrieve high-quality horizontal wind profiles from VT measurements a very high synchronization of the scanning Doppler lidars is necessary and the retrieval requires a thorough quality control and careful processing. To get information on the horizontal distribution of the wind, several VTs have to be placed at different locations in the investigation area, which strongly increases the demands for the synchronization and the

complexity of the scan pattern. While the VT technique is a very promising approach, it has so far not been used to study the three-dimensional distribution of the horizontal wind field over urban complex terrain.

One of the target areas of the $[UC]^2$ project is the city of Stuttgart in south-western Germany. It is a very good example for a large city located in mountainous terrain which suffers from frequent air quality issues (Scherer et al., 2019a). The city centre is located within a valley basin, which is joined by a small valley and has a narrow opening to a larger valley, with widths of the basin and the valley on the order of 2 km, i.e. they are much smaller than previously studied urban areas. The whole area is densely populated, with a lot of industry. Besides the high emission of pollutants, the topography and its impact on the wind field in the urban ABL is a main factor for the air quality issues in Stuttgart. Up to now there have only been very few studies of the urban ABL of Stuttgart. Coarsely resolved numerical simulations have been conducted by Schädler and Lohmeyer (1996) to assess the impacts of a planned new main railway station in the city centre on the urban climate. They found that cold air down-slope and down-valley flows are essential for the air quality in the city centre. They also observed that the ventilation is worse in areas with high buildings. Tethered balloon measurements have been conducted by Vogt (1999), who verified the existence and strength of the modelled cold air down-slope and down-valley flows. These studies indicate the significance of the wind field for the urban climate of Stuttgart, but detailed, three-dimensional observations of the flow in the urban ABL are still missing.

Extensive meteorological measurements were taken in and around the city of Stuttgart in the years 2017 and 2018 within the framework of the $[UC]^2$ project (Scherer et al., 2019a) in order to provide a comprehensive data set for process and long-term studies, as well as to deliver a high-quality data set for model evaluation. The VT method was applied to probe the horizontal wind field at different locations near Stuttgart in summer 2017. It is the first time that VTs are used to study flow characteristics in an urban environment in complex terrain.

Thus, three objectives are addressed in this study, with the first one being more technical:

1. Is it possible to use the VT method to derive mesoscale flow characteristics in the ABL in highly complex urban terrain? What processing steps are necessary?

2. What flow characteristics do occur in the ABL near Stuttgart and how are they influenced by the orography?

3. How does the flow depend on large-scale wind and atmospheric stratification?

To answer these questions measurements from a surface station, a microwave radiometer, a ceilometer and radiosondes are used in addition to the VT measurements.

In the following section, the theoretical background on the ABL in urban terrain, as well as topographic influences on the wind field are given. In Sect. 3 the used instrumentation and the field campaign are described. The dual-Doppler lidar technique, the method to derive VTs, and the data processing are explained in Sect. 4. In Sect. 5, a case study is analysed in detail and a statistical analysis of the wind field is conducted. A summary and conclusions are given in Sect. 6.

2 Theory on the atmospheric boundary layer in complex terrain

2.1 The atmospheric boundary layer

The lowest layer of the troposphere, which is directly influenced by the surface of the earth is called the atmospheric boundary layer (ABL). The ABL can be defined as the part of the atmosphere that responds to surface forcings within a timescale of one hour or less (Stull, 1988). The surface forcings include friction, vertical heat and moisture transport, aerosol and pollution emissions and flow modification by the terrain. The vertical transport in the ABL is mainly due to turbulence. Depending on the thermodynamic and dynamic conditions, the ABL has a depth between some hundreds of metres to a few kilometres. The part of the troposphere above the ABL, which is less affected by the ground, is called the free atmosphere. The following description of the characteristics of the ABL in this section is based on Stull (1988).
The conditions in the ABL are largely controlled by the conditions at the surface. Heating of the surface due to the absorption of solar radiation during the day and cooling due to outgoing longwave radiation during the night causes a diurnal cycle of the surface temperature. This leads to a typical diurnal cycle of the ABL over flat homogeneous terrain under undisturbed conditions with two distinct ABL regimes (Fig. 2.1): during daytime, the convective boundary layer (CBL) forms and during nighttime, the stable boundary layer (SBL) and the residual layer above characterize the ABL. The main difference between the two regimes is the vertical transport by turbulence. While in the CBL the air is well mixed throughout the layer due to convection, vertical movement is limited and sporadic in the SBL. This is caused by the different thermal stratification in the layers, which controls the buoyancy of the air. Buoyancy is one of the driving forces for turbulence in the CBL and can be described by the virtual potential temperature (θ_v).

2.1.1 The virtual potential temperature

Air parcels rise because they are less dense than the surrounding air, i.e. they are positively buoyant. In dry air, the potential temperature is a measure for the density of an air parcel. The potential temperature (θ) of an air parcel is the temperature air would have, if it was brought to a reference pressure adiabatically. According to Stull (1988) it is defined as:

$$\theta = T \left(\frac{P_0}{P} \right)^{0.286} , \tag{2.1}$$

with the actual temperature of the air T, the air pressure P and the reference pressure P_0, which is usually set to 1000 hPa. The exponent 0.286 is the quotient of the gas constant of dry air and the specific heat of dry air.

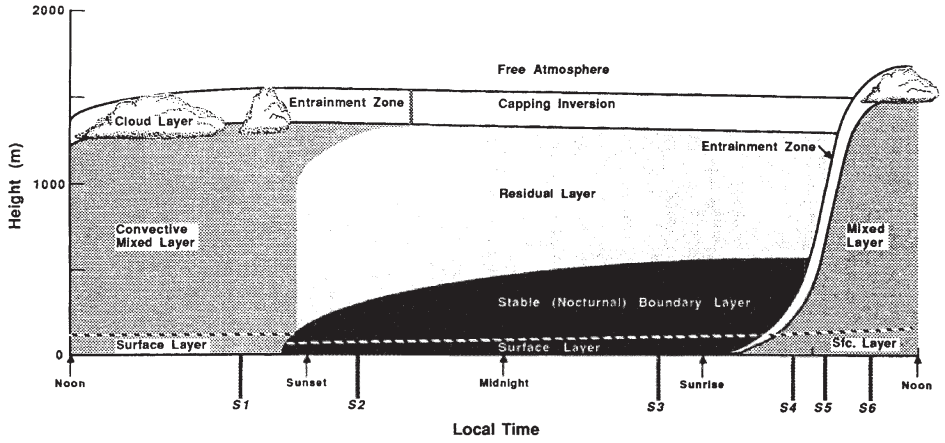

Figure 2.1: Typical diurnal cycle of the ABL over flat, homogeneous terrain in high pressure regions (copied from Stull, 1988, p. 11).

In dry air the potential temperature is a measure for the density: the higher the potential temperature, the lower the density of the air parcel. The difference of the potential temperature of a dry air parcel and the (dry) surrounding air determines the buoyancy of the air parcel: the higher the potential temperature of the air parcel is compared to the surrounding air, the higher is its buoyancy. If the specific humidity of the air is relatively constant with height the potential temperature can also be used as a measure for the density of moist air.
However, if the distribution of moisture with height is inhomogeneous the potential temperature is not an adequate measure for density. Then, the virtual potential temperature has to be used a measure of the density of air that includes moisture. It is defined for an unsaturated air parcel as:

$$\theta_v = \theta \cdot (1 + 0.61r) \,, \tag{2.2}$$

with the water vapour mixing ratio r (Stull, 1988).

2.1.2 The convective boundary layer

The CBL is characterised by convection, i.e. buoyancy driven turbulence. The source of convection is usually a vertical potential temperature difference. The temperature difference results from advection of cold air over warmer ground or from solar heating of the ground in the course of the day. The air in the surface layer (SL), roughly the lowest 10 % of the CBL, is heated from the ground (Figs. 2.1 and 2.2). In the SL, the air is warmer than above, i.e. the virtual potential temperature in the SL decreases with height (Fig. 2.2). As the virtual potential temperature is a measure for density (Sect.2.1.1), the air at the surface is more buoyant than the air above and so the stratification is statically unstable. Any small trigger mechanism like ground inhomogeneity may initiate convection, i.e. thermals of warm air moving upwards and thermals of cold air moving downwards. Above the unstable SL there is the mixed layer (ML) (Fig. 2.1). In the ML the virtual potential temperature is roughly constant with height, and lower than in the SL (Fig. 2.2). Warm thermals originating at the ground move upwards through the ML, because they are more buoyant than the air around. By up and downward movements the warm air from the SL is mixed throughout the ML and heats the ML. The ML is topped by an inversion, the so-called entrainment

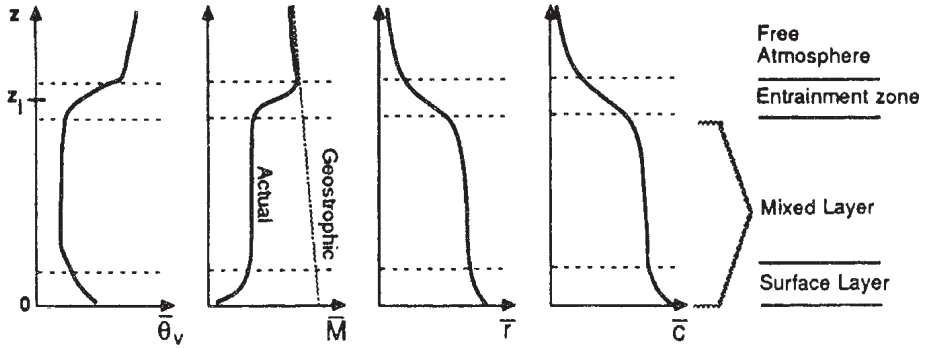

Figure 2.2: Typical profiles in the CBL of mean virtual potential temperature $\bar{\theta}_v$, wind speed $\bar{M}$, water vapour mixing ratio $\bar{q}$ and concentration of pollutants $\bar{c}$ (copied from Stull, 1988, p. 13).

zone (Fig. 2.1 and 2.2). In this entrainment zone, the upward moving air parcels are mixed with the free atmosphere. As the potential temperature of the free atmosphere is higher than in the ML it is less dense and therefore the upward movements are inhibited.

Under high pressure over flat, homogeneous terrain the typical evolution of a CBL starts in the morning shortly after sunrise, when due to insolation, the ground becomes warmer than the air above (Fig. 2.1). The air in the lowest few centimetres above the surface within the so-called microlayer, is heated by thermal conduction from the ground. It becomes warmer than the air above resulting in unstable stratification and the onset of convection. A ML starts to build up with a capping inversion above. Rising thermals of warm air heat the ML and penetrate into the capping inversion of the entrainment zone, where they are slowed down and mixed with the free atmosphere. Due to entrainment at the top the ML grows in the course of the day reaching a maximum height in the afternoon (Fig. 2.1). If the height of the capping inversion exceeds the lifting condensation level fair weather clouds (cumulus humils) may form. Towards the evening, solar heating of the ground is reduced and the ground cools as outgoing thermal radiation dominates over insolation. As the temperature difference of the ground and the air in the mixed layer decreases convection decays and eventually ends, when the ground gets cooler than the air above. From then on a stable layer forms at the ground (Sect. 2.1.3).

The mean horizontal wind speed in the ML is relatively constant with height, as momentum is well mixed in the layer due to convection (Fig. 2.2). Due to surface friction the wind speed is smaller than the geostrophic speed. The reduction of wind speed leads to a reduction of the Coriolis force, so the wind direction is slightly rotated cyclonically relative to the geostrophic wind, resulting in flow towards the low pressure, crossing the isobars in a small angle. Towards the ground wind speeds approach zero, correspondingly the wind directions are rotated cyclonically even more. In the entrainment zone wind speed and direction rapidly approach the geostrophic wind. Concentrations of pollutants and passive tracers, like water vapour, are relatively constant in the ML due to convective mixing and usually increase towards the ground, where their sources are. In the entrainment zone they usually decrease to small values in the free atmosphere (Fig. 2.2). As the capping inversion prevents vertical movement pollutants are often trapped below and can accumulate in the ABL during periods with high pressure conditions.

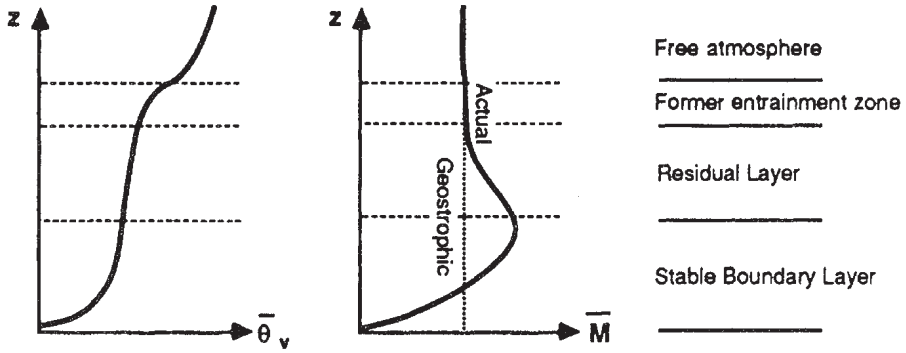

Figure 2.3: Typical profiles in the SBL of mean virtual potential temperature $\bar{\theta}_v$ and wind speed $\bar{M}$. The wind profile shows a LLJ at the top of the stable layer (copied from Stull, 1988, p. 16).

2.1.3 The stable boundary layer

In contrast to the CBL, vertical movement of air is limited in the SBL. A SBL forms when the air is warmer than the ground, which is the case if warm air is advected over a cold surface, or if the ground cools, usually during nighttime due to thermal long-wave emission. A thermal heat flux from the air towards the ground cools the air in the lowest layer, which reduces the virtual potential temperature and thus the buoyancy. In the SBL the virtual potential temperature increases with height, so the buoyancy decreases with height and the vertical movement is suppressed. Therefore it is called statically stable stratification.

Typically a SBL starts to form in the evening shortly before sunset, when the ground gets cooler than the air in the mixed layer above (Fig. 2.1). Downward heat flux in the lowest layer leads to the formation of a stable layer above the surface (Fig. 2.3). Throughout the night the stable layer grows, but as vertical movement is suppressed, the SBL grows much slower than the CBL during the day. The stable stratification also limits vertical transport of momentum, so the wind speed within the SBL decreases strongly towards the ground (Fig. 2.3). Towards the top of the stable layer the wind speed increases to geostrophic or often even becomes super-geostrophic, leading to strong wind shear within the layer, which may causes turbulence. Shear induced turbulence is the driver for the downward (turbulent) heat flux, by which the SBL grows. The probability of the occurrence of turbulence can be estimated using the Richardson number (Sect. 2.1.4). Above the SBL there is a neutrally stratified layer, which is a residual of the ML of the day, therefore it is called the residual layer. The former entrainment zone of the CBL is still visible as a capping inversion above the residual layer (Fig. 2.3).

A common phenomenon in the SBL is a maximum of wind speed around the top of the stable layer, which often becomes super-geostrophic: the low-level jet (LLJ) (Fig. 2.3). Stull (1988) defines a LLJ as a maximum in wind speed, which is more than $2\,\mathrm{m\,s^{-1}}$ faster than the wind above and occurs within the lowest 1500 m above the surface. A LLJ can have many different causes like baroclinity associated with synoptic conditions or sloping terrain, flow distortion by mountains, land sea breezes or inertial oscillations. Best understood is the process of the inertial oscillation in the SBL, which was first explained by Blackadar (1957). In the ML wind speed is subgeostrophic due to frictional drag. In the SBL, surface friction is reduced strongly compared to the ML. Thus, during the formation of the SBL in the evening the wind in the residual layer increases

towards geostrophic. In the ML, pressure gradient force Coriolis force and frictional force are in equilibrium. The rapid reduction of frictional force during the formation of a SBL causes an imbalance between pressure gradient force and Coriolis force and the flow is accelerated. This leads to an inertial oscillation, during which the wind speed oscillates around the geostrophic value. In mid-latitudes the period of the inertial oscillation is around 17 h, i.e. the maximum of the LLJ is expected around 8.5 h after the formation of the SBL. An example for a LLJ associated with baroclinity induced by sloping terrain is the common occurrence of a strong low-level wind over the Great Plains in the central USA, blowing parallelly to the contour lines of the terrain (Whiteman, 2000).

2.1.4 The Richardson number

Vertical mixing in the ABL is usually related to turbulence. The thermal stratification determines if the ABL the statically stable or unstable. In the CBL, which is statically unstable, vertical movement is enhanced, in the neutral boundary layer it is unaffected, and in the SBL, which is statically stable, vertical movement is suppressed. However, the existence of turbulence also depends on the vertical wind shear. Shear can cause turbulence even if the stratification is statically stable. The probability of turbulence can be investigated using the Richardson number. The Richardson number is the ratio of the buoyant production/consumption term of turbulent kinetic energy to the shear production/loss term (see Stull, 1988). For two discrete height levels the bulk Richardson number is defined as:

$$R_B = \frac{g\,\Delta\theta_v\,\Delta z}{\theta_v\,\left[(\Delta u)^2 + (\Delta v)^2\right]}\,, \tag{2.3}$$

with the gravitational acceleration g, and the differences between the two layers of the virtual potential temperature $\Delta\theta_v$, height difference Δz, and the vectorial components of the horizontal wind Δu (northwards) and Δv (eastwards). Values of virtual temperature and wind components in the equation are mean values.

The bulk Richardson number can be interpreted as a measure for dynamic stability and therefore the probability of turbulence. The higher the Richardson number, the more dynamically stable is the situation, and the more unlikely turbulence is to occur (Fig. 2.4). As a critical Richardson number $Ri_c = 0.25$ has been determined empirically for the gradient Richardson number (Stull,

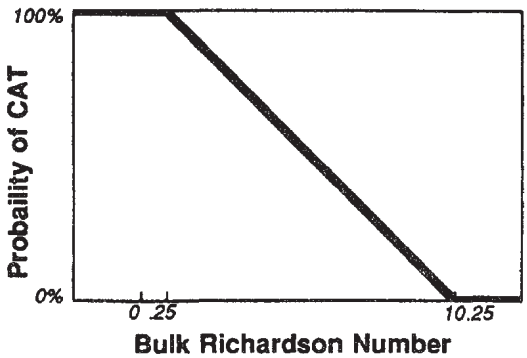

Figure 2.4: Empirical relationship between the bulk Richardson number and the probability of turbulence (clear air turbulence, CAT). The critical Richardson number of 0.25 is marked on the x-axis (copied from Stull, 1988, p. 178).

1988). If the bulk Richardson number is negative the conditions are statically unstable. For values between zero and the critical value, the stratification is statically stable, but the flow is dynamically unstable. For bulk Richardson numbers below the critical value, turbulence is most likely to occur (Fig. 2.4). For values larger than the critical value, it is unlikely that turbulence develops, as the thermal stratification is strongly stable and the flow is dynamically stable.

As the bulk Richardson number determines the probability and strength of vertical mixing it can be used to investigate the interaction of the flow at different heights. For dynamically unstable flow, vertical momentum transport is strong, i.e. wind direction and speed are similar throughout the ABL and the flow is coupled. For dynamically stable flow the vertical momentum transport is suppressed and the flow can decouple between lower and higher altitudes.

2.2 The urban boundary layer

The processes occurring in the urban boundary layer are in general similar to the ones in the ABL over rural terrain, but human activities in cities influence the urban boundary layer in several ways. In contrast to natural surfaces cities are characterised by heterogeneity on small scales, consisting of buildings, streets, and park areas, etc. of different shapes and sizes. These anthropogenic structures have different thermodynamic and dynamic properties than natural surface cover. Additionally, human activity such as transport and industry emit heat and pollutants into the urban boundary layer. General characteristics of the urban boundary layer according to Barlow (2014) are described in the following.

When wind flows over changes in surface properties like roughness, internal boundary layers form, i.e. layers influenced by the roughness elements in the new area, that grow in height with the distance downstream of the change. Regarding internal boundary layers, horizontal scales in the urban boundary layer can be defined such as street (10 m to 100 m), neighbourhood (100 m to 1000 m), and city (10 km to 20 km). These can be seen as scales below which the heterogeneous

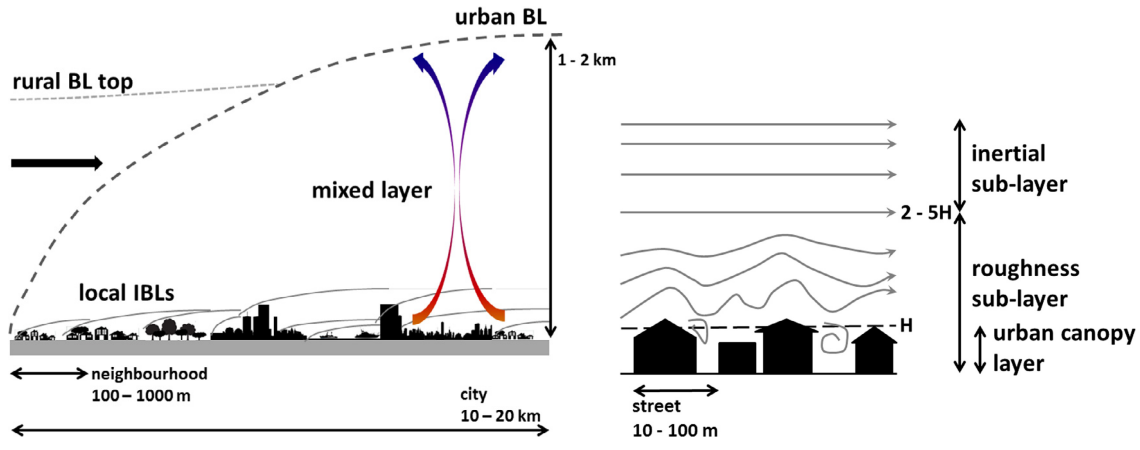

Figure 2.5: Sketches of the urban boundary layer. (a) shows the modification of a rural ABL flowing over urban terrain under convective conditions. Internal boundary layers (IBLs) form over areas of different surface roughness. The vertical axis is exaggerated. (b) gives an idea on how the wind field is influenced in the different layers. The dashed line marks the mean building height H (both figures copied from Barlow, 2014, p. 220).

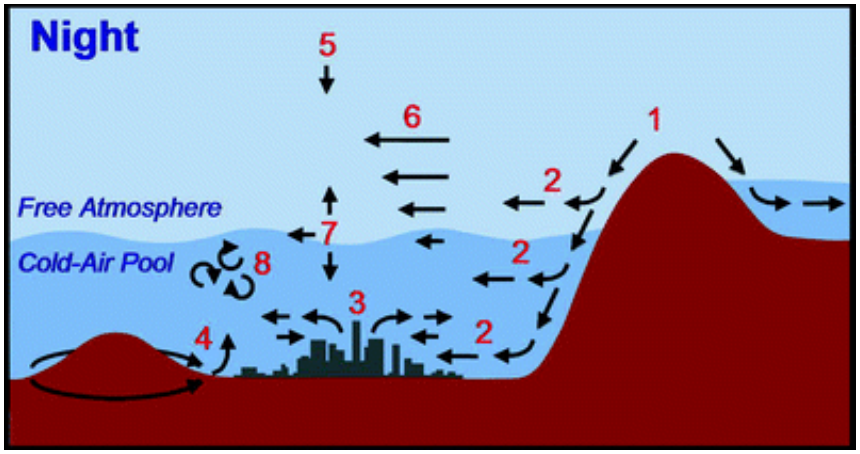

Figure 2.6: Sketch of processes occurring in the wind field of the urban boundary layer in complex terrain, during nighttime (Jerome Fast, copied from Steyn et al. (2013), p. 262). Down slope flow (1), detrainment of slope flow (2), urban heat island circulation (3), terrain induced convergence and divergence (4), mesoscale subsidence (5), regional wind systems (6), gravity waves (7), shear driven turbulence (8).

structures become homogeneous, i.e. a city consists of several differently built-up neighbourhoods, which can be seen as homogeneous areas of different surface roughness on the city scale (Fig. 2.5a).

The energy balance over urban areas differs from rural conditions. Sensible heat flux is generally larger due to the surface materials and increased surface areas due to buildings. Anthropogenic heat sources additionally increase the flux. This is the reason for the so-called urban heat island, which can drive mesoscale thermal circulations similar to the land-sea breeze. The urban heat island increases convection, therefore the urban CBL is deeper than the CBL over rural terrain (Fig. 2.5a). Also artificial materials used in cities (concrete, etc.) have a high heat capacity, so the thermal inertia of a city is higher than of a rural area. This causes urban areas to cool down slower than rural areas after sunset, which slows down the formation of the nocturnal SBL and can sometimes even preserve a shallow convective layer throughout the night. Latent heat flux in urban areas is generally smaller due to soil-sealing and little vegetation. Compared to vegetated rural areas, where a large part of the incoming solar energy evaporates water, the lack of water sources in cities increases the sensible heat flux in urban areas.

Roughness elements in cities, like buildings, are large and cause flow distortions that produce turbulence and frictional drag on the flow. In the roughness sub-layer, with a depth of 2 to 5 times the mean building height, the flow is strongly spatially inhomogeneous and can be dominated by turbulence (Fig. 2.5b). Above, in the inertial sub-layer, turbulence is more horizontally homogeneous and fluxes vary only little with height. The inertial sub-layer behaves similar to the SL of the standard ABL with increasing wind speed with height. Above the inertial sub-layer the urban boundary layer behaves similar to the normal ABL although fluxes may vary.

In complex terrain, the flow in the urban boundary layer is affected by the topography in addition to the urban influences. An important factor determining the wind field in the urban boundary layer in complex terrain are topographically and thermally induced flows (Fig. 2.6). An overview of the most important flow modifications related to the the topography are treated in Sect. 2.3.

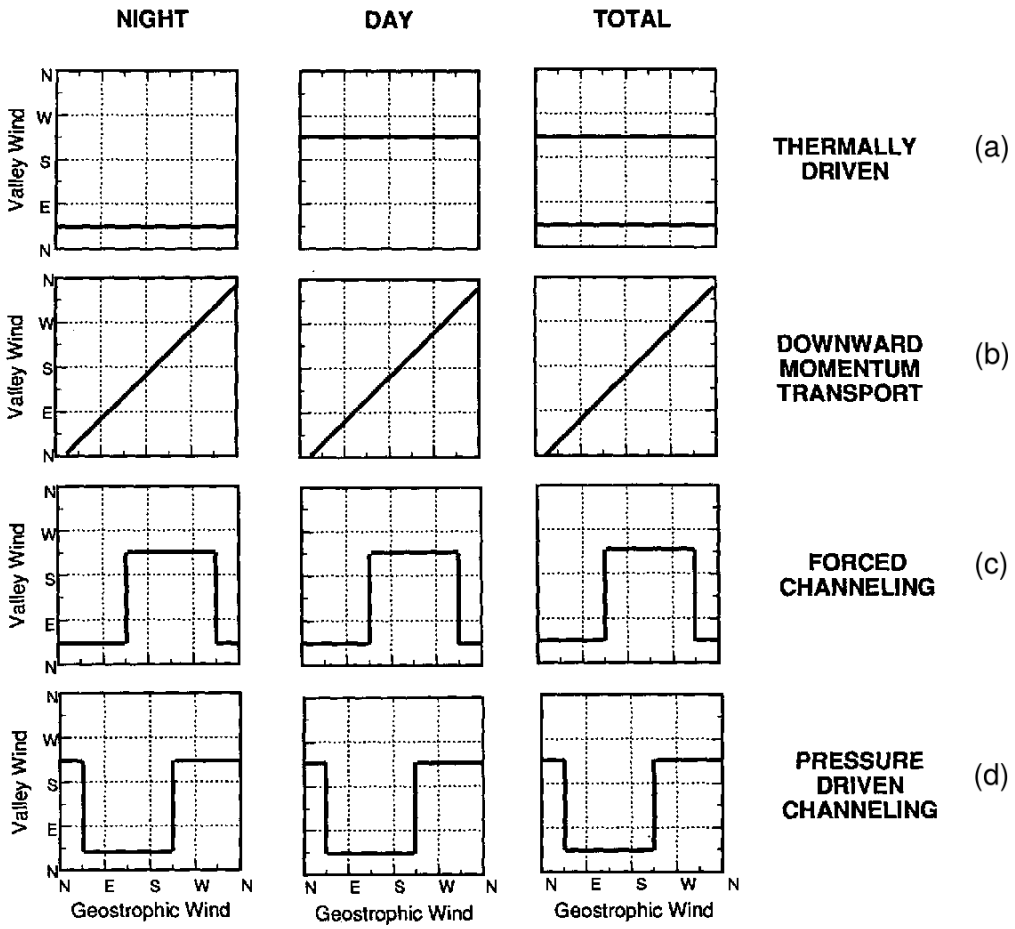

Figure 2.7: Relationships of the wind directions above a valley (geostrophic) and in the valley for different forcing mechanisms. The valley in this example runs from northeast to southwest, i.e. a northeasterly wind flows down-valley and southwesterly wind flows up-valley (copied from Whiteman and Doran, 1993).

2.3 Flow modifications in valleys

The flow within valleys is influenced by synoptic conditions, the topography and thermal effects. Whiteman and Doran (1993) proposed four forcing mechanisms that control the wind in valleys. The relationship of the geostrophic or the ambient wind direction above the valley, to the wind directions in the valley, resulting from these different forcings, are depicted in Fig. 2.7 for an exemplary valley oriented from northeast to southwest. The processes are introduced in the following.

The first mechanism Whiteman and Doran (1993) proposed is thermal forcing. After sunset the ground cools due to thermal emission, which cools the air above, leading to the formation of a stable layer. In a valley the cool, dense air flows down the slopes and forms a cold air pool at the bottom of the valley (Fig. 2.6). The air in the valley is colder than the air outside the valley at the same level, resulting in a horizontal pressure gradient (Fig. 2.8a). The pressure gradient drives down-valley winds at nighttime during stably stratified periods. During daytime the air within the valley warms faster than the surrounding air due to the contact to the slopes and the smaller volume of air within the valley. This results in a pressure gradient opposite to the one at night, resulting

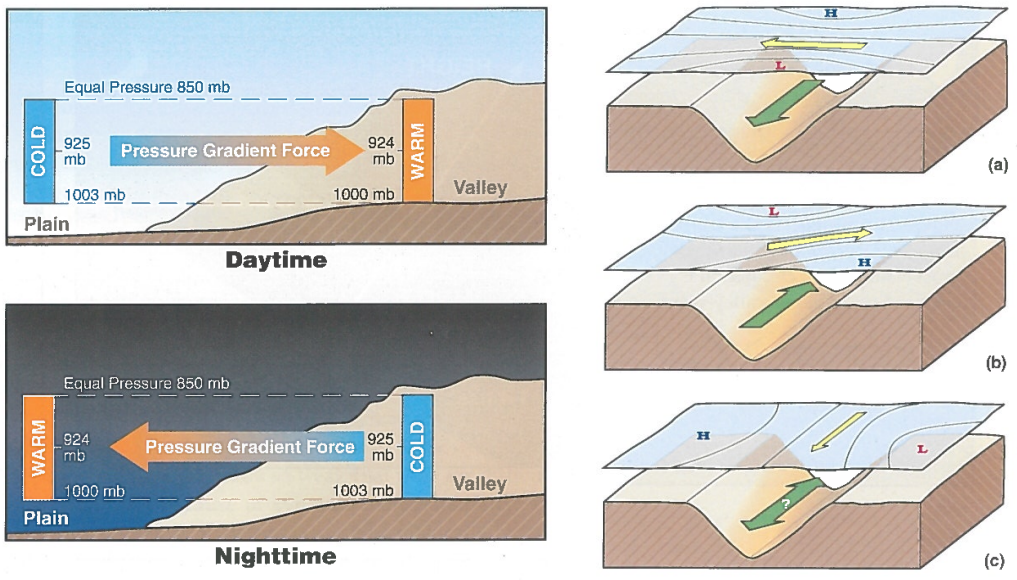

(a) (b)

Figure 2.8: Forcing mechanisms of valley winds. (a) shows the principle of thermally driven up- and down-valley winds during day and night. (b) sketches pressure driven channelling depending on the pressure gradient parallel to the valley axis. The yellow arrow indicates the synoptic or ambient wind, the green arrow denotes the corresponding valley wind (figures copied from Whiteman, 2000, p. 188 and p. 185).

in up-valley flow (Fig. 2.8a). These thermally driven circulations under idealised conditions are independent from the ambient flow above the valleys, and the valley wind direction only changes from day to night (Fig. 2.7a). The flow at the lower level is decoupled from the ambient wind. As decoupling is more probable for positive bulk Richardson numbers, i.e. statically stable conditions, down-valley winds are expected to be more pronounced than up-valley winds.

A second mechanism controlling the valley wind is downward momentum transport. Vertical mixing due to turbulence in the CBL or at strong wind shear results in valley winds similar to geostrophic winds above. Due to surface friction and sheltering of the terrain, the valley winds are weaker and the wind directions are slightly turned cyclonically due to reduced Coriolis force. Downward momentum transport is most likely to occur under unstable or neutral conditions in wide valleys with low sidewalls. Under these conditions thermally driven up-valley winds are expected to be small and dominated by downward momentum transport (Fig. 2.7b). Vertical momentum transport couples the flow throughout the ABL, i.d. the bulk Richardson number is smaller than the critical value.

In narrower valleys under unstable or neutral conditions, forced channelling may occur. Momentum is vertically mixed by turbulence, but winds are channelled by the valley, i.e. winds blow either up- or down-valley. The valley wind under forced channelling conditions depends on the projection of the ambient wind on the valley axis. The wind will blow up or down the valley and abruptly change sign, when geostrophic wind direction cross a line orthogonal to the valley axis (Fig. 2.7c).

If neither downward momentum transport, nor thermal effects have a strong impact on the valley flow, pressure driven channelling may occur. In this process wind in the valley flows along the val-

ley axis in the direction of the strongest pressure gradient force (Fig. 2.8b). The flow is strongest when the pressure gradient points along the valley axis, and correspondingly the geostrophic wind blows orthogonally to the valley. The flow direction changes between up-valley and down-valley if the geostrophic wind shifts across the valley axis. This means that the wind direction relationship is the similar to forced channelling, but shifted by 90° (Fig. 2.7d). During pressure driven channelling so-called countercurrents can occur, when the wind in the valley blows opposite to the along valley wind component of the geostrophic wind above. Pressure driven channelling is most likely to occur during statically stable conditions, i.e. for positive bulk Richardson numbers, as the low-level wind is decoupled from the ambient wind.

3 Measurement setup and devices

3.1 Field campaign and investigation area

The data analysed in this thesis was gathered in the orographically structured area around the city of Stuttgart in southwestern Germany during summer 2017. The field campaign in Stuttgart was part of the research programme "[UC]^2 - Urban Climate Under Change" (Scherer et al., 2019a,b). The programme is funded by the German Federal Ministry of Education and Research (BMBF) and has the aim to gain knowledge on the atmosphere over urban terrain and create a powerful urban climate model to be applied by researchers and municipalities (Maronga et al., 2019).
The topography of the region and the measurement sites are shown in Figure 3.1. The investigated area is characterised by the relatively broad Neckar valley, which is orientated southeast-northwest and the Stuttgart basin ("Stuttgarter Kessel"), a bowl shaped valley oriented southwest-northeast with a narrow opening to the Neckar valley. The Neckar valley has an approximate width of about

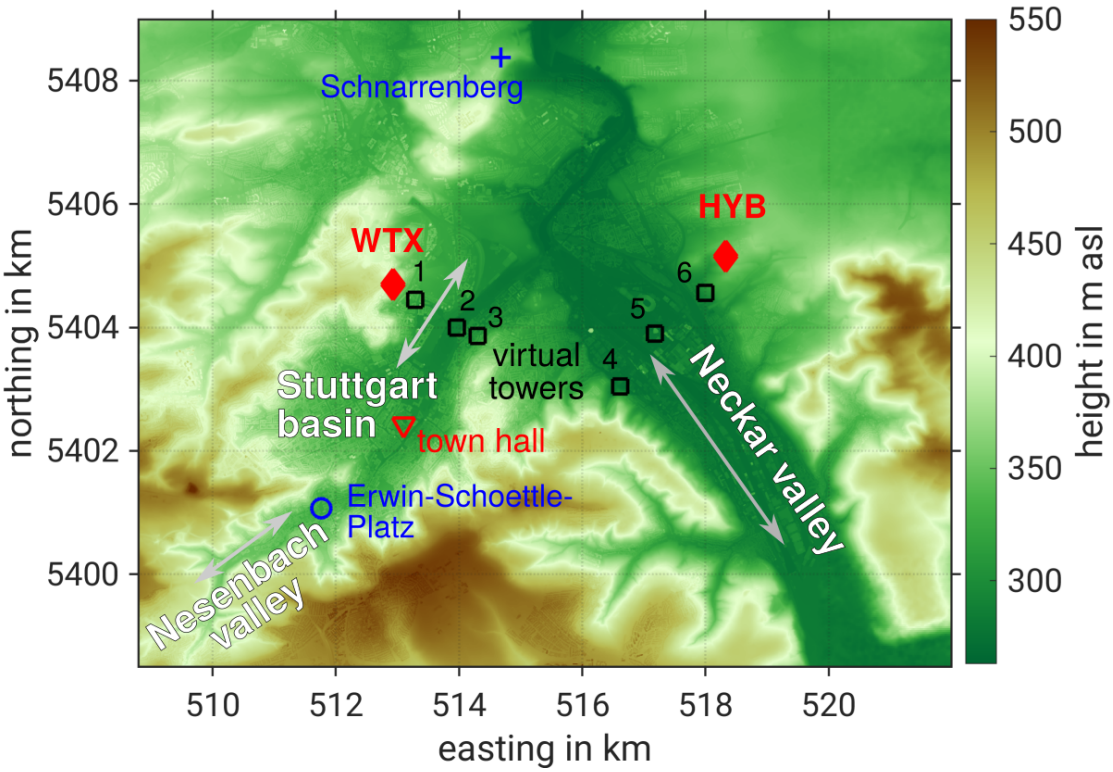

Figure 3.1: Topographic height (terrain, plus building height) and measurement sites in and around the city of Stuttgart. HYB and WTX are Doppler lidars used for the VT measurements. A third, profiling Doppler lidar (Windcube) and a microwave radiometer were installed on top of the town hall. Radiosondes were launched from Erwin-Schoettle-Platz during IOPs and near-surface data was taken from a meteorological station at Schnarrenberg. Topographic data provided by the German Aerospace Centre (DLR). The arrows indicate the general orientation of the valleys. Coordinate system: UTM (ETRS89) zone 32U.

2 km. The Stuttgart basin has a size of approximately 3 km × 2 km and from the southeast the narrow Nesenbach valley joins the basin. The valley bottoms are at heights of 250 m to 350 m above mean sea level (m asl), while the ridge height of the surrounding hills is about 520 m asl. The Neckar Valley is deepest south of around 5403 km northing, as the hills confining the east side of the valley decrease in height by about 150 m towards the north.

Several instruments were deployed in the investigation area to measure wind, temperature and humidity. The investigation area with the measurement sites is displayed in Fig. 3.1, and locations and altitudes are given in Tab. 3.1. The coordinate system used is Universal Transverse Mercator (UTM), based on the European Terrestrial Reference System 1989 (ETRS89) with the Geodetic Reference System 1980 (GRS 80) spheroid, zone 32U. The topographic data was provided by the German Aerospace Center (DLR). The three Doppler-lidars and the microwave radiometer are part of the mobile integrated atmospheric observation platform KITcube (Kalthoff et al., 2013). Two WindTracer Doppler lidars (HYB, WTX) were set-up on the slopes to measure profiles of the horizontal wind using the VT technique (e.g. Damian et al., 2014). The HYB device was positioned on the eastern slope of the Neckar valley, while WTX was located opposite on the northern hillside of the Stuttgart basin's opening to the Neckar valley (Fig. 3.1). A third Doppler lidar (Windcube) measured wind profiles in the city centre in the Stuttgart basin on the roof of the town hall, using the DBS (Doppler beam swinging) technique (e.g. Werner, 2005). To gain information on atmospheric stability, continuous temperature and humidity profiles from a microwave radiometer (MWR) were used, which was installed on top of the tower of the town hall in the Stuttgart basin. Radiosondes were launched by the German Weather Service (DWD) during intense observation periods (IOPs), at the Erwin-Schoettle-Platz in the southeast of the city centre, where the Nesenbach valley joins the Stuttgart basin. Near-surface and ceilometer data were used from a meteorological station operated by the DWD at Schnarrenberg, on a hill north of the city centre (Fig. 3.1).

The data used here were collected from July to September 2017. Dual-Doppler lidar measurements to generate VTs were carried out on 36 days during three periods: 14 to 25 July, 3 to 18 August and 29 August to 5 September. Within these periods, measurements from the Windcube were available on 22 days, while microwave radiometer data were available on 17 days (Tab. 3.1). Four IOP days with radiosoundings fell into this period, with a total of 15 launches. Near-surface data

Table 3.1: Location and altitude of the used devices in the UTM (ETRS89) coordinate system zone 32U and availability during the days when VTs were measured with the Doppler lidars WTX and HYB.

device	easting (m)	northing (m)	height (m asl)	available days
lidar "WTX"	512 924	5 404 697	392	36
lidar "HYB "	518 332	5 405 157	357	36
lidar "Windcube"	513 099	5 402 426	325	22
microwave radiometer	513 074	5 402 466	357	17
radiosondes	511 762	5 401 069	322	4 (15 launches)
meteorological station	514 679	5 408 377	366	36

from the meteorological station were available for the whole period. More detailed information on the devices is given in the following sections.

3.2 Doppler lidar devices

3.2.1 Doppler lidar principle

Doppler lidar (light detection and ranging) is a remote sensing technology to gain information on the position and speed of an object relative to the measuring device by detecting backscatter from a pulsed laser beam. The principle of Doppler lidar for wind measurement is described in Werner (2005) and sketched in Fig. 3.2.

A Doppler lidar device consists of a pulsed laser source and a detector for backscattered light. The detector on the one hand has a high sampling rate and on the other hand can determine the wavelength (or frequency) of the received light.

When a short laser pulse emitted from the device is scattered by an object (e.g. dust particles, aerosols), the part of the light that is scattered back to the device is measured by the detector. The timespan Δt between the emission of light and the arrival of the backscattered light is recorded and gives information on the distance of the object to the lidar. It is the time that the light needs to travel from the source to the object and back again to the detector. As the light has to travel the distance between the device and the scattering object twice and the speed of light in air c is known, the distance d is:

$$d = \frac{\Delta t \cdot c}{2} \,. \tag{3.1}$$

If the backscattering object moves relative to the device the frequency of the scattered light is Doppler shifted, i.e. due to the Doppler effect the frequency of the scattered light differs from the emitted light. This frequency shift Δf can be measured by the detector and depends on the speed of the object (v_r) relative to the device:

$$f - f_0 = \Delta f = f_0 \frac{2v_r}{c} \,, \tag{3.2}$$

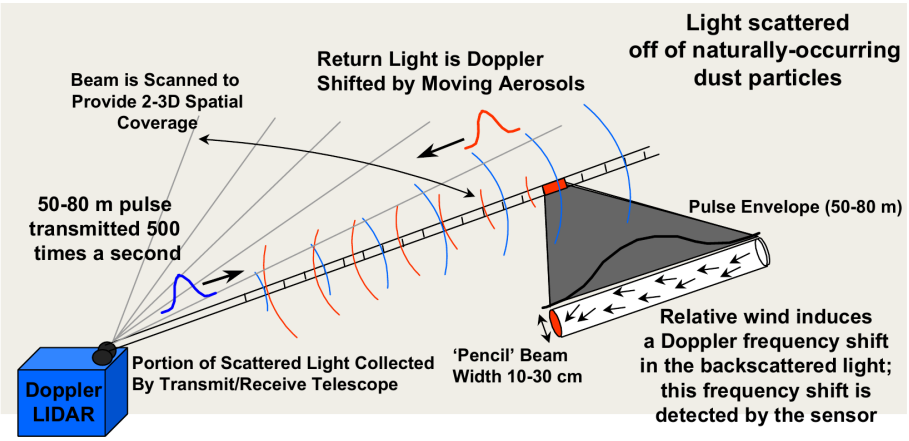

Figure 3.2: Measurement Principle of Doppler lidar (copied from Barr, 2008, p. 85). Laser pulses are emitted by the Doppler lidar and scattered by aerosols. Aerosols moving relative to the device induce a frequency shift of the backscattered light, which is detected by the device.

with the emission frequency f_0 and the Doppler shifted frequency of the backscattered light f. To detect Δf the returned signal is mixed with a signal of a reference frequency (heterodyne detection), and the velocity of the moving target is then determined by a Fourier-transform (Werner, 2005).

In the ABL, the largest part of light is scattered by aerosols, which means that Doppler lidars generally measure the speed of aerosols. As they are assumed to be small enough to move along with the air, their movement resembles the actual wind at their location (e.g. Grund et al., 2001).

Figure 3.2 sketches the principle of a Doppler lidar for wind measurement. The Doppler lidar device emits coherent laser light which is depicted by the blue wave fronts. Along the beam the emitted light is scattered by moving aerosols. The backscattered light depicted as the red wave fronts is detected by the device. If the backscattered light was scattered by aerosols that moved relatively to the device, it has experienced a Doppler frequency shift, from which the wind speed can be derived.

What has to be considered is that Doppler lidar cannot measure exact radial velocities of a single aerosol at one point in space. Due to the finite laser pulse length and beam width, the backscattered light recorded at a point in time originates from a volume of air, i.e. an accumulation of many aerosols ("pulse envelope" in Fig. 3.2). Therefore the radial velocities measured with a Doppler lidar are always volume averages over the pulse volume. Doppler lidars can only measure radial velocity, i.e. the velocity in direction of the laser beam. From this radial velocity the atmospheric wind components can be retrieved applying different methods described below.

3.2.2 WindTracers

The main focus of this thesis is the analysis of horizontal wind profiles derived with the VT technique. These are performed by two lidars of the type "WindTracer", manufactured by Lockheed Martin. The two systems are called "HYB", which was manufactured in 2004 and "WTX", manufactured in 2009. Technical properties and used settings of the devices are listed in Table 3.2.

The devices emit infrared laser pulses of a pulse length of 300 ns (WTX) and 370 ns (HYB) (Tab. 3.2), which means that the length of the pulse volumes is around 90 m and 111 m. The minimum physical spatial resolution is therefore 45 m and 56 m, respectively. The backscatter signal is sampled by the detectors at a rate of 250 MHz, resulting in a theoretical resolution of 0.6 m along the beam. The number of samples used for the calculation of the Doppler-shift with the Fourier transform determine the range gate length. Here it was set to 69.5 m for both devices, meaning that the radial winds are averages for bins of this length. The accumulation frequency was set to 10 Hz. The maximum measurement range was 12 km, depending on the atmospheric conditions.

Both lidar systems are equipped with a freely configurable two-axis scanner making it possible to perform synchronized scans with the two devices which is required for the performing of dual-Doppler measurements. From their positions on the slopes the two devices had a good view on the opening of the Stuttgart basin as well as on the Neckar valley at Bad Cannstatt, allowing the placement of 6 VTs along two cross-section lines through the valleys (see Fig. 3.1). As the dual-Doppler lidar measurements conducted with the two WindTracer lidars are the focus of this thesis, the method is described in detail in a separate Section (Sect. 4.1).

Table 3.2: Technical properties and settings of the “WindTracer” Doppler lidar devices.

	WTX	HYB
laser type	Er:YAG	TM:LuAG
wavelength in µm	1.617	2.023
pulse length in ns	300	370
pulse energy in mJ	2.7	2.0
pulse repetition frequency in Hz	750	500
sampling rate in MHz	250	250
accumulation frequency in Hz	10	10
range gate width in m	69.5	69.5

3.2.3 Windcube

A third, vertically profiling Doppler lidar was used to get information on the wind in the city centre. The “Windcube WLS8-3” manufactured by Leosphere automatically determines wind profiles over the device, using the Doppler beam swinging (DBS) technique. The DBS technique is a method to obtain three-dimensional wind vectors from one Doppler lidar device, using radial velocities at different beam angles (Werner, 2005). In a DBS scan, a Doppler lidar measures radial velocities in at least 3 linearly independent directions. These are usually arranged in a cone above the device at fixed elevation angles and discretely changing azimuth angles. As a comparison, in the similar velocity azimuth display (VAD) scan technique, the azimuth angles are shifted continuously. Assuming horizontally homogeneous flow through the cone, the measurements at three directions contain all components of the three-dimensional wind. The radial velocities measured in the different directions are projections of the wind vector on the corresponding lidar beam direction. Three-dimensional wind vectors can be calculated from the radial velocities similar to the proceeding for the dual-Doppler technique, which is described in Sect. 4.1.

The Windcube performed DBS scans consisting of 4 measurements of radial velocities at an elevation angle of 14.84° in azimuth steps of 90°. The device software outputs wind vectors in heights of 40 m to 600 m above the device in steps of 20 m at a temporal resolution of 10 min.

The Windcube was located on the rooftop of the town hall to measure wind profiles in the centre of Stuttgart (Fig. 3.1, Tab. 3.1). As the rooftop was about 28 m above the ground, the Windcube measured wind profiles starting above the surrounding buildings.

3.3 Other instruments

3.3.1 Microwave radiometer

A MWR manufactured by Radiometer Physics (humidity and temprature profiler “HATPRO”), was set up in the city centre on the tower of the town hall. It measured atmospheric emission at 14 frequencies in the microwave range, from which temperature profiles were retrieved using

an algorithm provided by the University of Cologne (Löhnert and Crewell, 2003; Löhnert et al., 2009). Details on the features of the device are given in Rose et al. (2005).
To increase the resolution of the temperature profiles in the boundary layer, so called boundary layer scans were performed at a fixed azimuth angle and varying, low elevation angles. Assuming horizontal homogeneity around the radiometer it is possible to retrieve temperature profiles with a vertical resolution of 50 m close to the ground, increasing towards 200 m at the top of the ABL (Crewell and Löhnert, 2007).
To obtain information on the atmospheric stability, potential temperature profiles were calculated from the retrieved temperatures and pressure profiles. The pressure profiles were calculated from in-situ pressure measurements at the device's housing using the barometric equation.
As the radiometer was installed on the tower of the town hall in a height of 60 m above the ground, the retrieved temperature profiles reflected the average stratification in the boundary layer above the buildings in the Stuttgart basin.

3.3.2 Radiosoundings

On 4 days during IOPs, radiosondes were launched by the DWD from Erwin-Schoettle-Platz in the southeast of the city centre, where the Nesenbach valley joins the Stuttgart basin (Fig. 3.1). The Vaisala Radiosondes "RS92" measured vertical profiles of pressure, temperature, relative humidity and wind speed and direction, with a vertical resolution of 5 m to 10 m, depending on the rising speed of the balloon. The radiosonde data from two consecutive days were used in the case study in Sect. 5.1, to investigate the thermal stratification using potential temperature profiles calculated from temperature and pressure, and to compare the VT measurements to wind profiles from the radiosoundings.

3.3.3 Meteorological surface station

The DWD operates a meteorological station at Schnarrenberg, a hill north of the city centre overlooking the Neckar valley (Fig. 3.1). Standard meteorological parameters such as temperature, pressure, humidity, precipitation and radiation are monitored at the station. The data are available with a temporal resolution of 10 min. A ceilometer was also operated at the station. Quick-look graphics from the ceilometer data were provided by the DWD, which are used in the case study in Sect. 5.1.

4 Method and processing

4.1 Dual-Doppler lidar method

A single Doppler lidar can only measure one wind component, the radial velocity relative to the device. Obtaining other atmospheric wind components from one device is only possible by using the VAD/DBS technique (see Sect. 3.2.3) with the assumption of horizontally homogeneous flow. However in topographically structured terrain, like valleys with densely built-up areas, this assumption is not applicable (Bingöl et al., 2009). To gain information on the two-dimensional atmospheric wind, the measurements of two lidar devices can be combined using the dual-Doppler method.

The principle of the dual-Doppler lidar method is to use two lidars to measure radial velocities at the same point in space from two different positions, i.e. the lidar beams cross at one point under a certain intersection angle. The two radial velocities contain information on two linearly independent wind components at the specific point. These can be calculated using vector algebra. In the following the dual-Doppler lidar method is described for the geometry that is used in this thesis. In Sect. 4.1.1 the geometrical principles of the dual-Doppler technique are explained, and in Sect. 4.1.2 an approach to arrange the measurements in space to get information on wind profiles, so-called virtual towers (VTs), is introduced.

4.1.1 Dual-Doppler lidar technique

The radial velocity $v_{r,i}$, which is measured by Doppler lidar i, is a projection of the three-dimensional wind vector $\vec{u}$ on the lidar beam direction unit vector $\vec{e}_i$. The wind vector $\vec{u}$ consists of the three wind components u (eastwards), v (northwards) and w (upwards). The direction of the lidar beam can be described by an azimuth angle α_i and an elevation angle ϕ_i. With this we obtain:

$$v_{r,i} = \vec{u} \cdot \vec{e}_i = \begin{pmatrix} u \\ v \\ w \end{pmatrix} \cdot \begin{pmatrix} \cos\phi_i \cdot \sin\alpha_i \\ \cos\phi_i \cdot \cos\alpha_i \\ \sin\phi_i \end{pmatrix} , \tag{4.1}$$

$$v_{r,i} = u \cdot \cos\phi_i \cdot \sin\alpha_i + v \cdot \cos\phi_i \cdot \cos\alpha_i + w \cdot \sin\phi_i \, . \tag{4.2}$$

This is an equation with three unknowns (u,v,w), so it can be solved using three independent equations. Measuring radial velocities at the same spot with two lidars ($i = 1,2$) yields two equations, so the system of equations is underdetermined. However, if one is interested in the horizontal wind $\vec{u}_h$, consisting of components u and v, rather than the vertical wind component, the system can be solved if a suitable geometry is chosen.

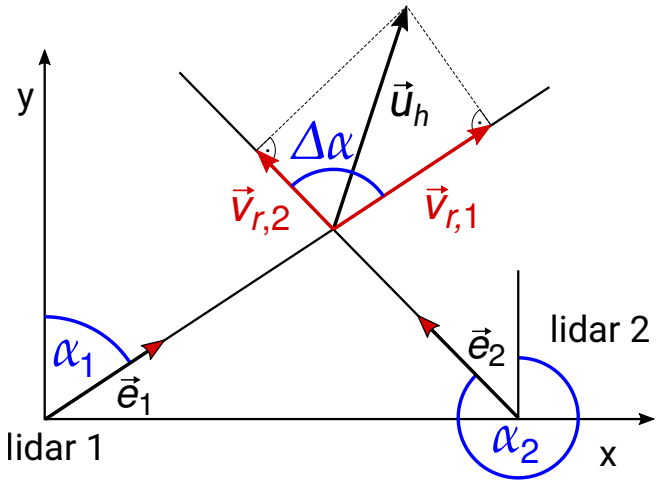

Figure 4.1: Principle of wind vector relations in dual-Doppler lidar measurements. Sketch for $\phi_{1,2} = 0°$ in top view, x-axis pointing eastwards, y-axis pointing northwards. The unit vectors of the lidar beam direction $\vec{e}_{1,2}$ are defined by the azimuth angles $\alpha_{1,2}$, the two beams intersect at the intersection angle $\Delta\alpha$. The lidar radial velocity vectors $\vec{v}_{r,1,2}$ are the parts of the horizontal wind vector $\vec{u}_h$ that are pointing in the lidar beam directions. The values of the radial velocities $v_{r,1,2}$ are the projection of the horizontal wind on the lidar beam direction vectors (Eq. 4.2).

If the positions of the two lidars are exactly on a horizontal plane with the observed point, i.e. the elevation angles are zero ($\phi_1 = \phi_2 = 0°$), the radial velocities do not contain any information on the vertical wind ($\sin\phi_i = 0$). In this case the equation system is determined and can be solved for the actual horizontal wind. The case of zero elevation angles is sketched in Fig. 4.1 in top view.

Although $\phi_{1,2} = 0°$ is only given when measuring in a horizontal plane, Eq. 4.2 can still be solved for other cases under certain assumptions. If the elevation angles are relatively small and/or the vertical wind speed is generally small, the terms $w \cdot \sin\phi_{1,2}$ can be neglected, resulting in a determined equation system for the horizontal wind. In the stable boundary layer the assumption of small vertical wind is valid, but in the CBL vertical wind speed may be large. Typical measurement errors resulting from non-zero elevation angles at different vertical wind speeds are displayed in Tab. 4.1. For the estimation of the errors, hypothetical radial velocities are calculated from typi-

Table 4.1: Errors of the horizontal wind speed calculated from dual-Doppler measurements, depending on the elevation angle ϕ and the vertical wind speed w. Errors are calculated exemplarily for a horizontal wind speed of $5\,\mathrm{m\,s^{-1}}$ and vertical wind speeds typically observed in the SBL ($0.1\,\mathrm{m\,s^{-1}}$) and in the CBL ($2\,\mathrm{m\,s^{-1}}$) (Stull, 1988). The used elevation angles are the mean, median, maximum and minimum of the actual values of the geometry used in this study (Sect. 4.2.1, Fig. 4.4). For the calculation of the errors one horizontal wind component is used and the lidar beam is assumed to be pointing in the same direction. The absolute errors are given in the table, with the relative errors in brackets.

elevation angle ϕ	SBL ($w = 0.1\,\mathrm{m\,s^{-1}}$)	CBL ($w = 2\,\mathrm{m\,s^{-1}}$)
8.4° (ϕ_{mean})	$0.015\,\mathrm{m\,s^{-1}}$ (0.3 %)	$0.297\,\mathrm{m\,s^{-1}}$ (5.9 %)
3.1° (ϕ_{median})	$0.005\,\mathrm{m\,s^{-1}}$ (0.1 %)	$0.107\,\mathrm{m\,s^{-1}}$ (2.1 %)
56.8° (ϕ_{max})	$0.153\,\mathrm{m\,s^{-1}}$ (3.1 %)	$3.053\,\mathrm{m\,s^{-1}}$ (61.1 %)
0° (ϕ_{min})	$0\,\mathrm{m\,s^{-1}}$ (0 %)	$0\,\mathrm{m\,s^{-1}}$ (0 %)

cally occurring horizontal and vertical wind speeds at different elevation angles for one horizontal component using Eq. 4.2. Then, Eq. 4.2 is solved for the horizontal wind component, assuming the vertical wind to be $0\,\mathrm{m\,s^{-1}}$ and the calculated wind speed is compared to the original. Due to small vertical wind speed in the SBL the resulting errors are generally small, even at large elevation angles. In the CBL, vertical wind speed can be considerably higher, which adds errors to the measurements increasing with larger elevation angles. At large elevation angles the error becomes large if strong updraughts in the CBL are observed. However, the largest elevation angles in this study occur when the wind is measured at the highest measurement levels, which are expected to be around the top of the CBL, where the vertical wind decreases at the capping inversion (Sect. 2.1.2).

Thus, with two lidars ($i = 1,2$) and neglecting the vertical component, Eq. 4.2 can be solved for the horizontal wind components u and v:

$$u = \frac{v_{r,1}\cos\phi_2\cos\alpha_2 - v_{r,2}\cos\phi_1\cos\alpha_1}{\cos\phi_1\cos\phi_2\sin(\alpha_1-\alpha_2)}\,, \tag{4.3}$$

$$v = \frac{-v_{r,1}\cos\phi_2\sin\alpha_2 + v_{r,2}\cos\phi_1\sin\alpha_1}{\cos\phi_1\cos\phi_2\sin(\alpha_1-\alpha_2)}\,. \tag{4.4}$$

To minimize the effects the propagation of the individual lidar errors due to uncorrelated noise, the azimuthal intersecting angle $\Delta\alpha$ of the two lidar beams should be close to rectangular. Based on considerations of Stawiarski et al. (2013), Träumner et al. (2015) found intersection angles between 30° and 150° to be reasonable, which was considered for the VT setup.

Due to finite lengths of the laser pulses, lidar radial velocities are not point measurements but always volume averages. Horizontal wind components retrieved from dual-Doppler measurements are therefore a combination of radial velocities measured in two crossing range gates in this case of a length of approximately 70 m each and a width of approximately 20 cm (Barr, 2008).

4.1.2 Virtual towers

The idea of a VT is to obtain measurements in the atmosphere along a vertical profile, as if they were carried out by instruments on a meteorological measurement tower. In our case we aim to retrieve profiles of the horizontal wind. This was realised by the successive measurement of the horizontal wind in different heights along a profile, using the dual-Doppler lidar method (Sect. 4.1.1), i.e. the beams of the lidars cross at different heights with increasing elevation angles. Figure 4.2 shows how a VT using two lidar devices can be realised.

There are several ways of lidar scan patterns to perform VT measurements. Calhoun et al. (2006) used intersecting range-height indicator scans, i.e. scans at fixed azimuth and continuously varying elevation angle, to measure profiles of the mean wind. This method allows a rather high temporal resolution but is less accurate, as the radial velocities are not necessarily measured at the same time. Collier et al. (2005) measured at four discrete heights for a longer time (700 s) to get information on turbulence. This method has a high accuracy at cost of temporal resolution, i.e. repetition rate.

In this thesis an approach is used by which it is possible to get information on the horizontal as well as on the vertical variability of the horizontal, wind field, with a relatively high repetition rate

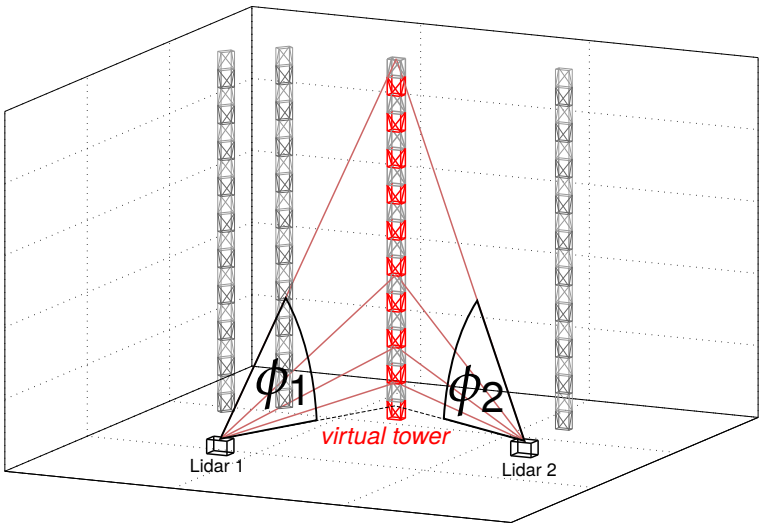

Figure 4.2: Sketch of a VT retrieved with the dual-Doppler lidar method (adapted from Damian (2012), p. 23). The laser beams of lidars 1 and 2 are intersecting at several discrete heights of the VT. During the scan of one VT the azimuth angles are fixed, while the elevation angles $\phi_{1,2}$ are varied.

Table 4.2: Location of VTs, terrain height at the positions, and measurement height range in the UTM (ETRS89) coordinate system zone 32U.

	easting (m)	northing (m)	ground height (m asl)	measurement range (m asl)
VT 1	513 290	5 404 451	316	361 - 787
VT 2	513 963	5 404 000	287	339 - 2309
VT 3	514 299	5 403 861	302	347 - 787
VT 4	516 617	5 403 043	275	341 - 781
VT 5	517 182	5 403 903	278	303 - 2273
VT 6	517 996	5 404 559	301	333 - 773

(around 15 min). Therefore six VTs were placed in the investigation area of Stuttgart, each VT consisting of 9 to 16 discrete measurement heights (Fig. 3.1 and 4.3). Two lines of three VTs each were spanned: one across the opening of the Stuttgart basin to the Neckar valley (VT 1 - 3), and one across the Neckar valley (VT 4 - 6) (Fig. 3.1). All towers consisted of 9 measurement heights between heights of 300 m asl to 800 m asl, with the lowest height 30 m to 50 m above the ground and with increasing vertical spacing upwards. The VTs in the middle of the valley (VT 2 and 5) had 7 additional measurement heights up to a height of 2300 m asl (around 2000 m above the ground). The exact locations and the measurement height range of each VT are given in Tab. 4.2 and the three-dimensional layout of the VTs and measurement heights are displayed over the topography of the area in Fig. 4.3.

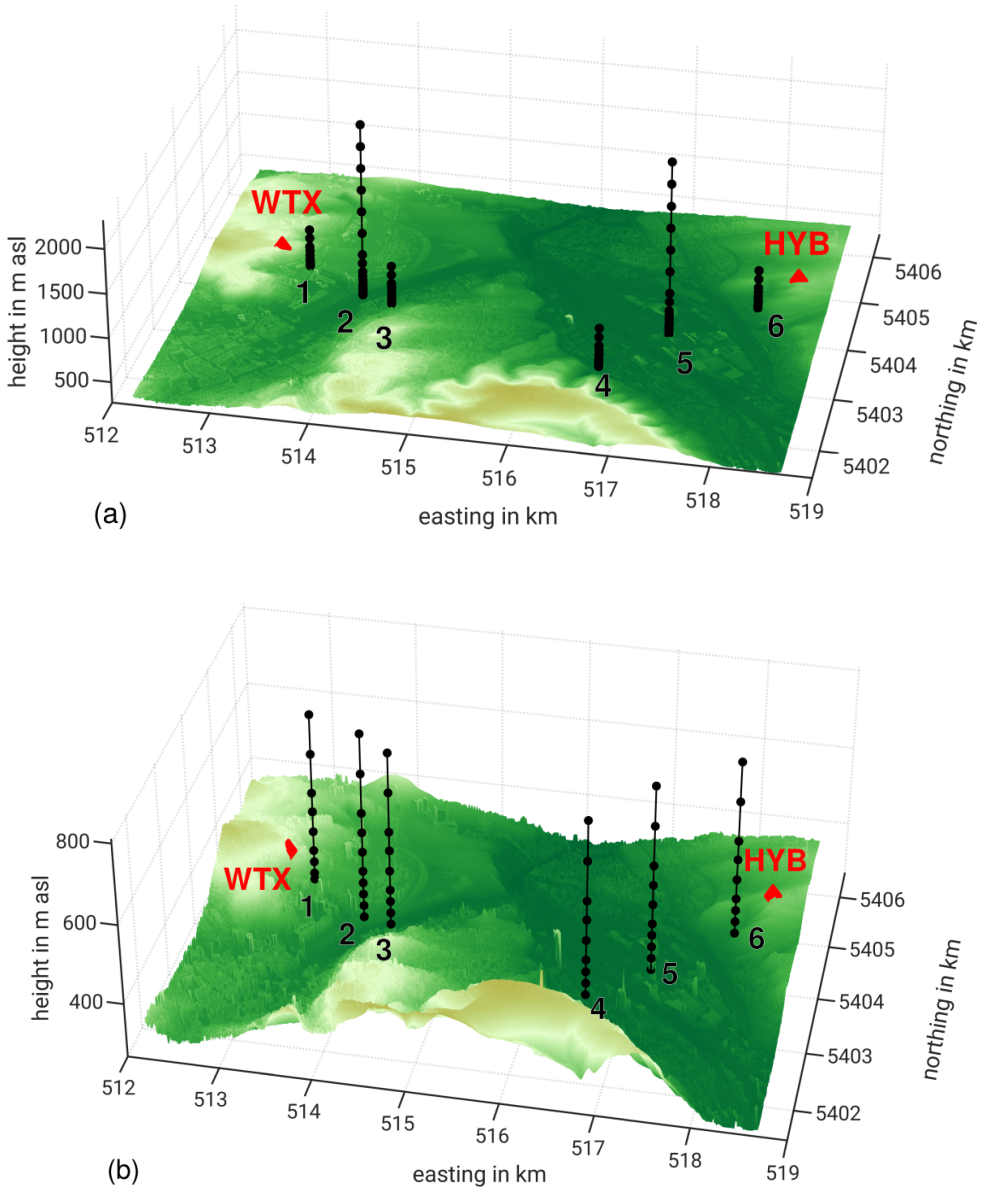

Figure 4.3: Arrangement of the 6 VTs with measurement heights (circles) in space. (a) shows all measurement heights above the topography of the area true to scale. In (b) only the measurement heights up to 800 m asl are displayed, with the height axis elongated by a factor of 5 compared to the horizontal axes. Topographic data and coordinate system as in Fig. 3.1.

4.2 Processing steps

One important aim of this thesis is to assess the applicability of the VT technique, to analyse flow characteristics over complex urban terrain. Therefore several processing steps are necessary to retrieve high-quality profiles of the horizontal wind. The following section describes the steps taken to obtain average profiles of the horizontal wind from the raw output of the Doppler-lidar devices HYB and WTX (see Sect. 3.2 for device descriptions).
The lidars provide raw data at an accumulation frequency of 10 Hz. The output information used was:

- time stamps in UTC (Coordinated Universal Time)
- azimuth and elevation angles of the lidar beam direction
- signal-to-noise ratio for every range gate
- radial velocity for every range gate calculated from the Doppler frequency shift of backscattered light.

4.2.1 Dual-Doppler scan pattern

Vertical profiles of the horizontal wind were measured at six VTs in the area around Stuttgart. The method and locations of the VTs are described in Sect. 4.1 and visualized in Fig. 4.3. The VTs consisted of 9 to 16 fixed measurement heights. The two lidar devices performed temporally synchronized scans, measuring simultaneously for 10 s at every measurement height of each tower, i.e. with an accumulation frequency of 10 Hz, 100 values are available at each height. The scan

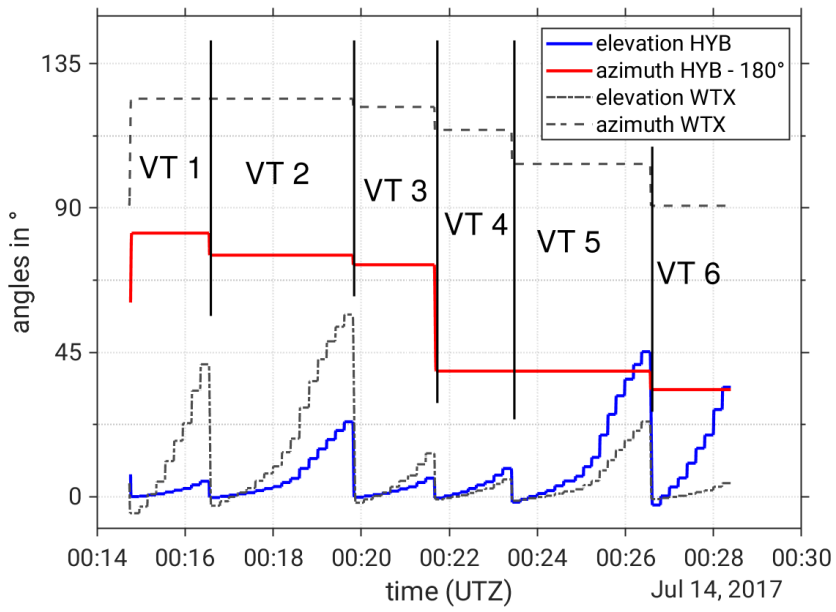

Figure 4.4: Lidar beam angles of Doppler lidars performing a complete scan of all VTs. The blue line shows the elevation angle of HYB, the red line the corresponding azimuth angle, with 180° subtracted for better visibility. The angles of WTX are displayed as the dashed lines. The black vertical lines mark the boundaries of the time periods, during which one VT is scanned.

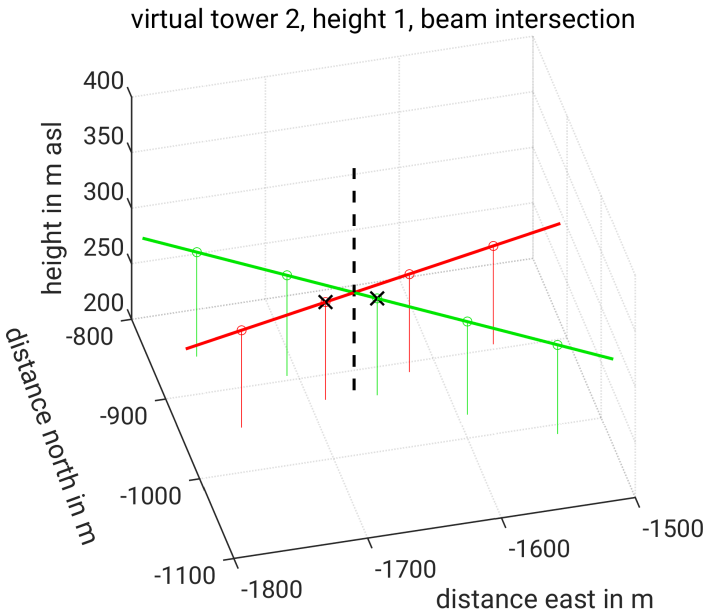

Figure 4.5: Intersection of lidar beams and range gates corresponding to a measurement height of a VT. The laser beams of the two lidars WTX in green and HYB in red intersect at a VT, indicated by the dashed black line. The circles with stems show the range gate centres, and the range gates with their centres closest to the VT are marked with a black 'x'. Horizontal coordinates are the distance from the WTX site.

started from the lowest height of the VT 1, proceeded upwards through all measurement heights of this tower, and continued with VT 2 to VT 6, scanning each tower from bottom to top. In total 68 heights were scanned. It took the two lidar devices approximately 15 min to complete one scan cycle, so the resulting data are 10 s measurement periods at every VT height level, all 15 min.

To illustrate a scan cycle the azimuth and elevation angles of a complete scan of both devices are displayed in Fig. 4.4. During the scanning of one VT the azimuth angles stay constant. The elevation angles increase for each tower, where every step represents the 10 s measuring period at one height level.

4.2.2 Identification of range gates for virtual towers

The first step to gain quality controlled wind speed profiles from the lidar output was to identify the range gates for HYB and WTX corresponding to the different height levels of the VTs. As shown in Fig. 4.4 every measurement height of each tower is characterized by a certain combination of azimuth and elevation angle, given by its location in space.

After the respective angles are identified the corresponding range gate has to be selected. It was chosen as the one closest to the measurement point of the VT. In Fig. 4.5 the intersection of the laser beams at a measurement point of a VT is depicted and the nearest range gates are marked by the crosses. The radial velocity measurements in these range gates are used in the following processing steps.

4.2.3 Filtering of raw data

The radial velocities at the selected range gates were filtered in three steps, in order to eliminate random noise and outliers before the calculation of the horizontal wind components. The effects of the filtering steps are displayed exemplarily in Fig. 4.6 for the radial velocities measured by one device at one VT height level on one day. First, a maximum radial velocity threshold filter was applied, followed by a signal-to-noise ratio (SNR) filter and finally an outlier filter based on the median absolute deviation (MAD) was used.

1. *Maximum radial velocity threshold.* Some radial velocity values occurred that were unrealistically high. To eliminate these measurements the maximum allowed absolute value of the radial velocity was set to $15\,\mathrm{m\,s^{-1}}$. Figure 4.6a shows the total amount of measurements at one range gate as grey dots. Especially during nighttime the radial velocities are very noisy, varying between $-50\,\mathrm{m\,s^{-1}}$ to $60\,\mathrm{m\,s^{-1}}$. After setting the threshold for absolute radial velocity (indicated by the red lines), the blue dots show the remaining data. 91 % of the raw data of all days remain after filtering with the maximum radial velocity threshold.

2. *SNR threshold.* Besides the signal of backscattered light a lidar device also detects atmospheric background radiation. The background radiation does not contain desired information and is regarded as noise. The SNR is the ratio of the detected backscatter signal compared to the signal of the background radiation when there is no backscattering. The SNR is given in dB, a logarithmic pseudo-unit to express ratios (e.g. Adler, 2014):

$$SNR = 10 \cdot \lg \frac{signal}{noise} \mathrm{dB}\ . \tag{4.5}$$

   To remove random noise, the data was filtered by setting a minimum threshold for the SNR. Measurements with SNRs below the threshold are filtered out. Due to different specifications of the two devices different minimum SNR thresholds were chosen of $-7\,\mathrm{dB}$ for HYB and $-8\,\mathrm{dB}$ for WTX, which gave reasonable results (see Adler et al., 2019).

   In the time series of the radial velocities in Fig. 4.6b the data prior to SNR filtering, depicted in grey, is still very noisy, in particular during nighttime. Application of a minimum SNR threshold, marked as the red line in the scatterplot, removes a lot of the apparently randomly distributed values. The blue dots that indicate the remaining data show a reasonable course over the day, but still contain some outliers. This is because the SNR filter thresholds of the devices were chosen not very strict, in order to keep as much information as possible. If the SNR threshold is chosen to high, realistic values might be filtered out, depending on the daily conditions. After filtering by SNR threshold 82 % of all raw data remain.

3. *Outlier filtering.* The final filtering step was the removal of outliers using a median absolute deviation (MAD) threshold. The MAD is a measure of the variability of a measurement series, that is, unlike the standard deviation, robust to outliers (e.g. Machiwal and Jha, 2012). It is defined as:

$$\mathrm{MAD} = \widetilde{|x_i - \tilde{x}|}\ . \tag{4.6}$$

   The MAD is the median (denoted by $\tilde{}$) of the absolute deviations of the single values x_i from the median of the whole series $\tilde{x}$.

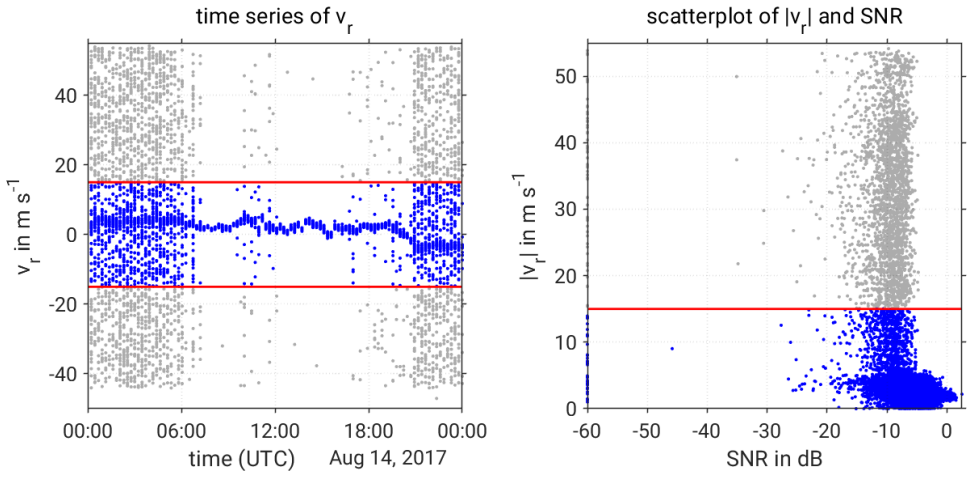

(a) 1st filtering step: maximum radial velocity threshold; red lines indicating threshold of 15 m s^{-1}

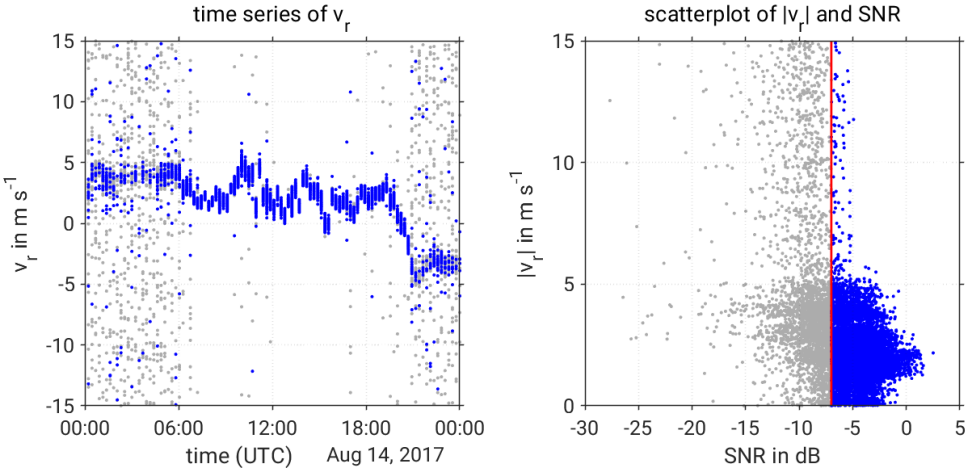

(b) 2nd filtering step: minimum SNR threshold; red line indicating threshold of −7 dB

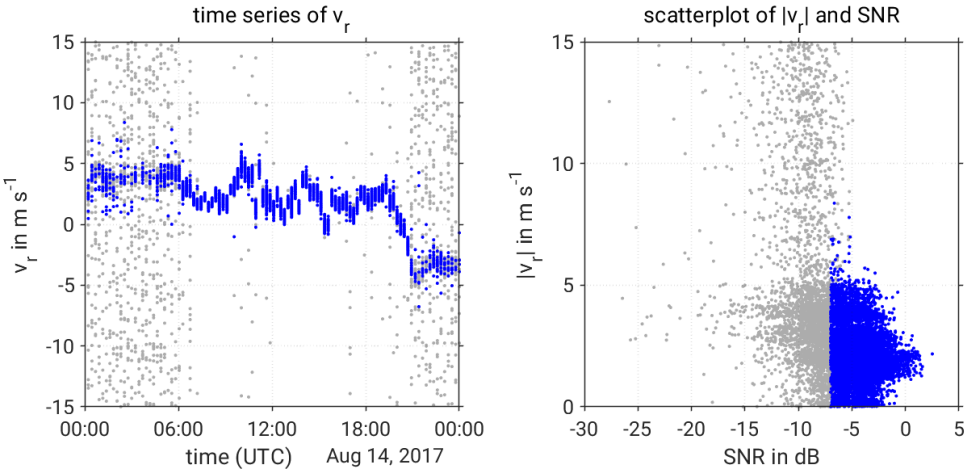

(c) 3rd filtering step: MAD based outlier filter

Figure 4.6: Filtering of raw radial velocity data: example for HYB, range gate at VT 2 height level 8 on 14 August 2017. Effects of the successive application of the filtering steps are displayed from top to bottom. The figures on the left show the time series of the radial velocity (v_r), the figures on the right are scatterplots of the absolute radial velocity $|v_r|$ against the SNR. The raw data are plotted as grey dots, blue dots mark the data that remain after each filtering step. The radial velocity data which remain after the three filtering steps (c) are used to calculate the horizontal winds.

Values are regarded as outliers $x_{i,out}$ if their absolute deviation from the median exceeds a certain multiple n of the MAD:

$$|x_{i,out} - \tilde{x}| > n \cdot \text{MAD} \tag{4.7}$$

The MAD threshold n was empirically determined to be 6 for HYB and 6.7 for WTX, which gave best results.

To take into account that the mean wind can change over the day the MAD was not calculated for whole days but for an moving window of a fixed amount of values around the timestamp of interest. Each window contained 900 values plus the value that was checked for being an outlier in the centre of the window. This means that data of roughly 1.75 h were used in one window.

As can be seen in Fig. 4.6c the MAD filter removes most of the outliers remaining after the SNR filtering. The remaining radial velocities are regarded as quality controlled. After the application of this third filtering step 81 % of the raw data remain and are used to calculate horizontal wind components.

After applying these 3 filtering steps in general good quality data remained. However some outliers may still exist for certain periods, as the filtering is a trade-off between keeping a maximum amount of good data and using the same thresholds for all days.

4.2.4 Calculation of horizontal wind vectors and temporal averaging

The filtered radial velocities are averaged over each 10 s measurement period to get the mean radial wind for each measurement height of each VT. The periods are not long enough to retrieve information on turbulence. The horizontal wind components were then calculated from the averaged radial velocities of both devices using Eq. 4.3 and 4.4. The horizontal wind values are thus

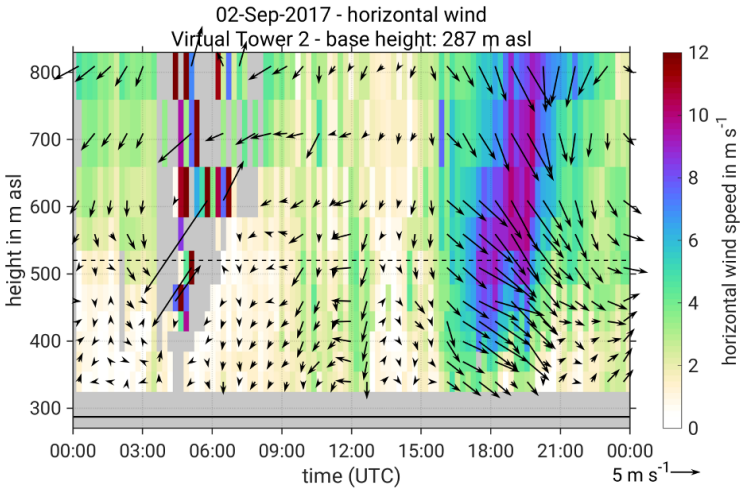

Figure 4.7: Example of horizontal wind profiles at VT 2 on 2 September 2017. The colour shading shows the horizontal wind speed at every 10 s measurement interval, grey areas indicate missing values which did not pass the filter criteria from Sect. 4.2.3. The arrows represent horizontal wind vectors at every third measurement interval. The solid black line at the bottom indicates the terrain height at the VT site, the dashed line marks the mean ridge height.

averages over 10 s, with every measurement height at a different timestamp. This means that every value reflects rather instantaneous conditions, which may lead to a considerable variability in time and height in particular during convective conditions. To better represent the mean horizontal wind at each measurement height and to make the measurements from individual towers comparable to each other, hourly averages are calculated.

Figure 4.7 shows an example of the horizontal wind profiles at a VT as retrieved at this processing step. As can be seen, the retrieved wind in general looks reasonable. Until 16:00 UTC there are weak winds from variable directions. After 16:00 UTC strong northwesterly wind prevailed at all heights with maximum values of $10\,\mathrm{m\,s^{-1}}$. Between 4:00 UTC and 7:00 UTC, however, the horizontal wind is still noisy and shows unrealistic values from strongly varying directions. Some of this noise is related to low availability of radial velocities in the 10 s interval. After the 3-step filtering described in Sect. 4.2.3, the number of available data in the 10 s averaging intervals varied. Horizontal wind is calculated from the averages regardless of the available radial velocity data. This means that horizontal wind is calculated even if only 1 value out of a maximum of 100 is available. If only few values are available during the 10 s intervals it is likely that they are erroneous, even though they passed the 3-step filtering. Thus, the quality of a horizontal wind value is regarded to decrease with data availability in the interval. This is illustrated in Fig. 4.8. The time series of the u wind component (blue crosses) looks reasonable, except for the time between between around 4:00 UTC and 7:00 UTC, where the values seem to be randomly distributed between $-10\,\mathrm{m\,s^{-1}}$ and $10\,\mathrm{m\,s^{-1}}$. The availability of radial velocity measurements is very low especially for HYB during this time. In order to filter out those data with low availability

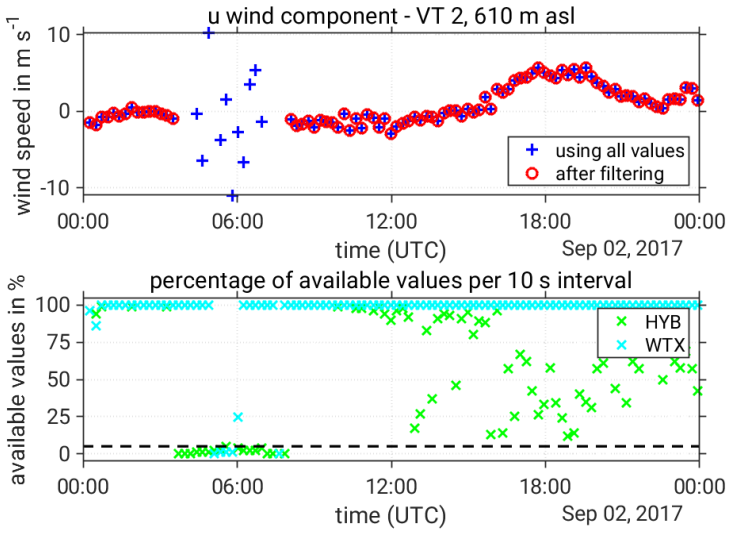

Figure 4.8: Example of a time series of the u wind component, and percentage of available data. Measurements are at the height 610 m asl from VT 2 on 2 September 2017, as in the previous example (Fig. 4.7). The top figure shows the time series of u of all 10 s measurement intervals as blue crosses, after the 3-step filtering described in Sect. 4.2.3. Red circles mark the data which remain after an additional filtering step based on data availability. The bottom figure shows the data availability within each 10 s measurement interval for the two devices, which remains after the 3-step filtering. The black dashed line marks the minimum threshold used for filtering due to data availability.

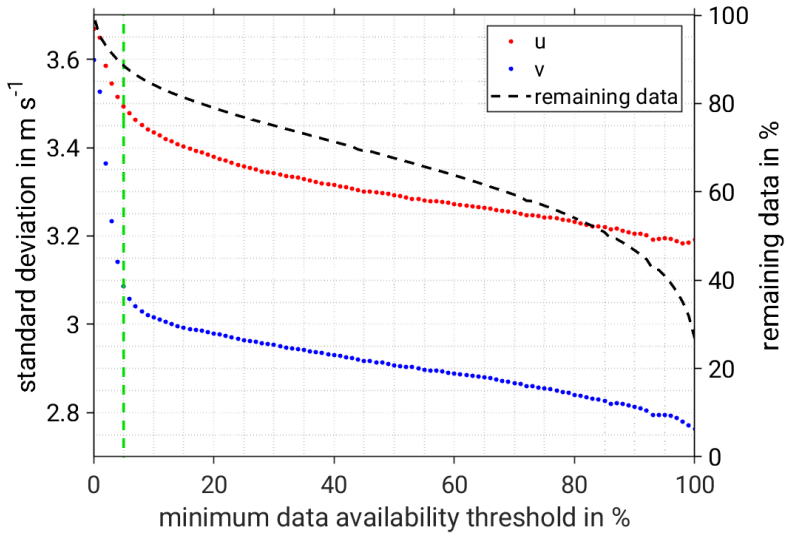

Figure 4.9: The effect of data availability of radial velocities on the standard deviation of the horizontal wind components. The left y-axis shows standard deviations of the wind components u and v calculated for all VTs and times. Red and blue dots show the values of the standard deviations after filtering out all intervals with data availability smaller than the percentage on the x-axis in 1 % steps. The dashed black line displays the percentage of data remaining after applying the minimum data availability thresholds (right y-axis). The threshold of minimum data availability per interval is set to 5 %, indicated by the dashed green line.

before calculating 1 h averages, a minimum threshold for data availability of radial velocity data has to be determined.

To decide which minimum threshold to choose for the data availability, the effects of filtering using different thresholds are compared in Fig. 4.9. Therefore the standard deviation of u and v is calculated for all measurement heights and all times. It is expected that values from intervals with low data availability increase the standard deviation of the data, as they are noisy and contain outliers (as in Fig. 4.8). If measurements from intervals with low availability are not considered, the standard deviation is expected to decrease. Standard deviations of u and v are calculated using different minimum thresholds for data availability. The minimum threshold ranges from 0 % (all data is used), up to 100 % (only measurement from intervals with 100 % data availability are used, i.e. not a single value was filtered out by the 3-step filter in Sect. 4.2.3). The filters were applied in 1 % steps. For example, the standard deviation of u at a minimum threshold of 20 % is around 3.4 $\mathrm{m\,s^{-1}}$. This value is calculated from all values from the 10 s intervals, at which both lidar devices have a data availability of at least 20 %.

In Fig. 4.9, it is evident that the standard deviations of u and v increase strongly, when considering values with less than 5 % data availability. Therefore, this value was chosen as minimum data availability threshold used for the filtering of the data before calculating the hourly averages. This fourth filter step removed additional 11 % of the data. As can be seen in the example in Fig. 4.8, the unrealistic wind values between 4:00 UTC and 7:00 UTC are removed after filtering with the 5 % data availability threshold.

After the application of the availability filter, hourly averages were calculated using the remaining values. As a scan duration was approximately 15 min an hourly average usually is calculated from four to five 10 s values, or less if periods are filtered out.

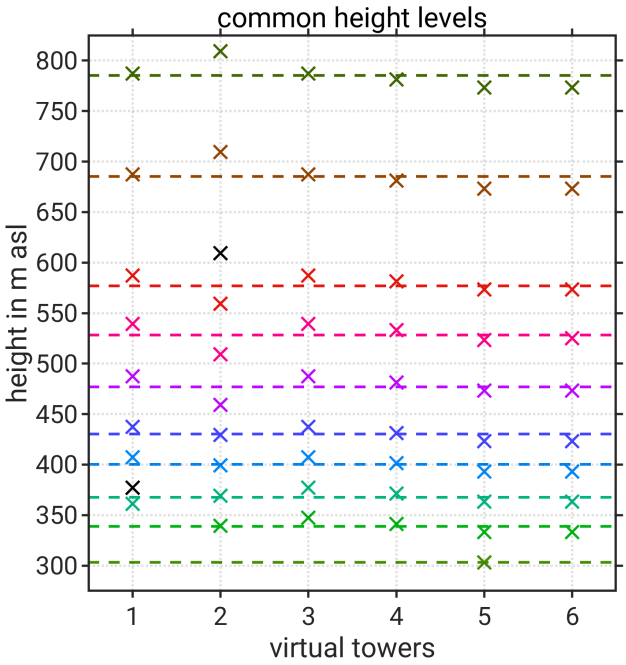

Figure 4.10: Lowest 10 common height levels of all VTs. The dashed lines mark the common height levels. The measurement heights of all six VTs are displayed as crosses above the VT number on the x-axis, with the same colour as the corresponding common height levels. The black crosses are measurement heights that were not assigned to the common height levels, as another height of the VT was closer to the corresponding common height level. The lowest level only contains one measurement height, because at the site of VT 5 the terrain height was significantly lower than at the other towers.

4.2.5 Determination of common height levels

The measurement heights of the VTs were assigned for every VT individually before the campaign. They are defined with respect to terrain height at the individual VT site, i.e. they are in general not at the same height above sea level. For the statistical analysis and to compare wind measurements at the different sites, common height levels in m asl were chosen for all towers, that were reasonably close to the actual heights. After assigning the measurement heights of the VTs to common height levels, the maximum distance of an actual height to the corresponding common height level was 24 m. The measurement heights of the VTs and the corresponding common height levels are displayed in Fig. 4.10, from the surface up to a height of about 800 m asl, the range in which there are measurements from all 6 VTs. The terrain height at the site of VT 1 was higher than at the other positions and its lowest measurement height corresponds to the 3rd common height level at about 365 m asl. As a result only 5 VTs are available at the second common height level at 340 m asl. The lowest common height level only contains VT 5, where the terrain height is lowest, and as there are no values to compare in this level, it is not used for the statistical analysis.

The measurements heights of the Windcube are evenly spaced at a distance of 20 m, with the lowest height at 365 m asl. For comparison with the VTs the height levels of the Windcube, which were closest to the corresponding VT common height levels are used.

5 Results

In the first part of this chapter, a case study is analysed in detail to better understand the dynamic and thermodynamic features in the ABL, which can be expected in the investigation area (Sect. 5.1). In the second part a statistical analysis is conducted, focusing on the flow characteristics (Sect. 5.2).

5.1 Case study

The horizontal wind field in the ABL is analysed qualitatively for a period from the noon of 14 August 2017 until noon of 15 August 2017. This period is chosen, as it is undisturbed by major large-scale influences, shows some interesting features and is within an IOP, which means that radiosounding data are available.

5.1.1 Synoptic situation

During the case study, the investigation area is under the influence of a high pressure system centred over eastern central Europe, as shown in the surface pressure chart in Fig. 5.1. A cold front is approaching from the west. In the morning of 15 August, a convergence line develops upstream of the cold front and on the early afternoon a convective cell with precipitation passes the investigation area, which is embedded in the convergence line (Fig. 5.2). The synoptic wind in 850 hPa turns from southeast over south to southwest in the course of the two days, as is shown in Fig. 5.3. It is regarded as the ambient wind, which is uninfluenced by topographic effects in the investigation area (as in Whiteman and Doran, 1993).

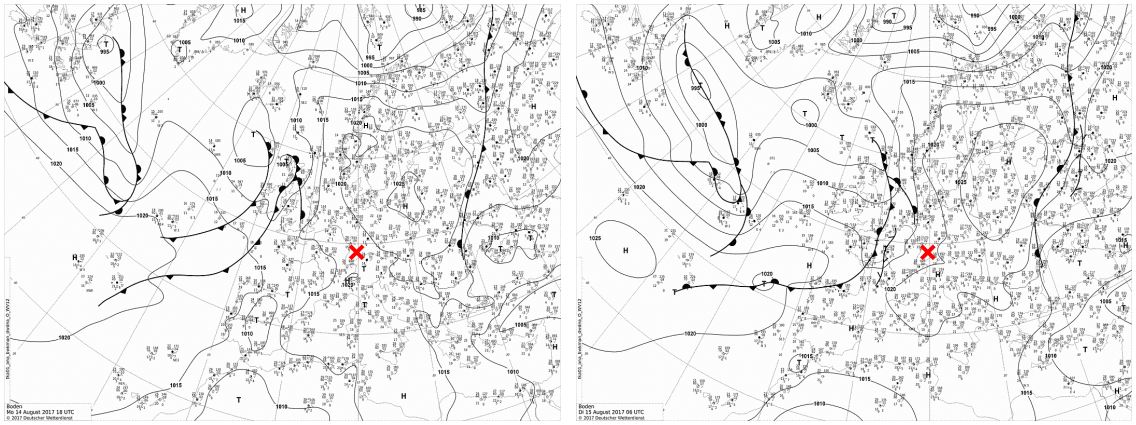

(a) 14 August 2017, 18:00 UTC (b) 15 August 2017, 06:00 UTC

Figure 5.1: Sea level pressure charts of Europe during the case study. Isobars are in steps of 5 hPa, the red cross marks the investigation area (wetter3.de, 2018b).

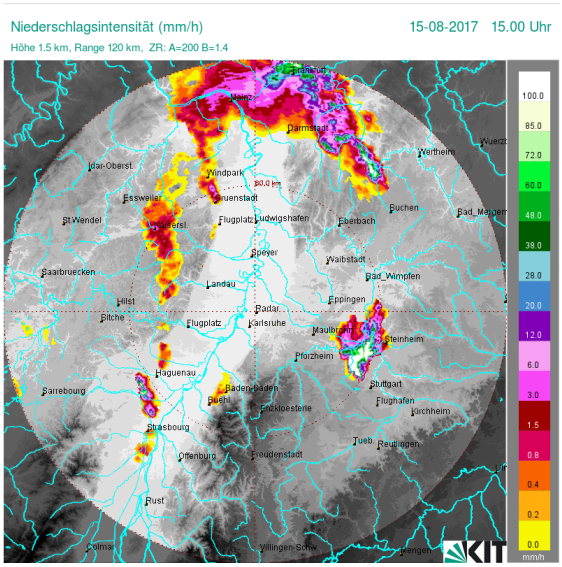

(a) 15 August 2017, 13:00 UTC

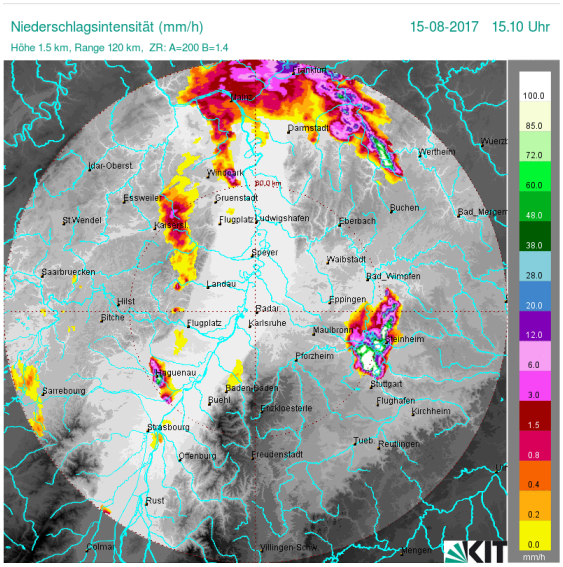

(b) 15 August 2017, 13:10 UTC

Figure 5.2: Radar images showing the precipitation rate. A convective cell passes the northern part of the investigation area around Stuttgart shortly after 13:00 UTC (imk-radar.de, 2019).

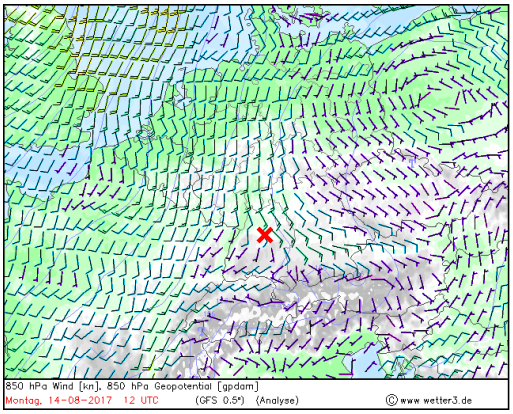

(a) 14 August 2017, 12:00 UTC

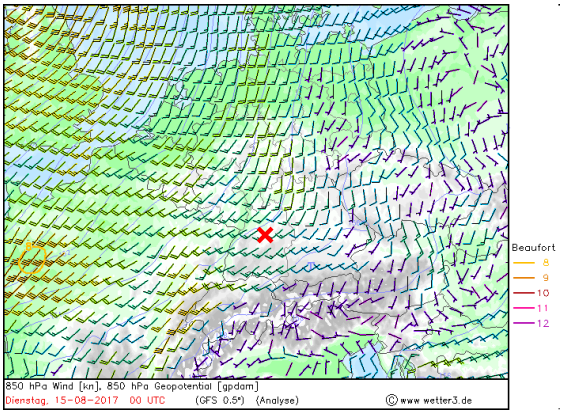

(b) 15 August 2017, 00:00 UTC

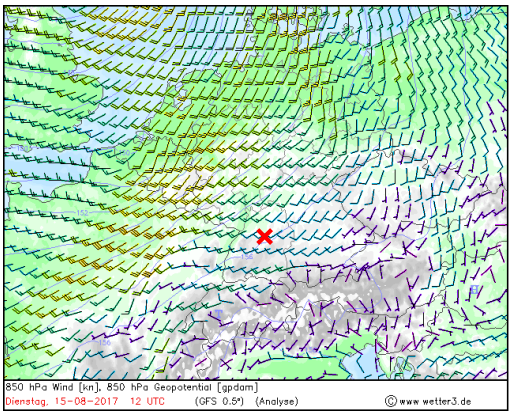

(c) 15 August 2017, 12:00 UTC

Figure 5.3: Spatial distribution of horizontal wind at 850 hPa (arrows) at different times during the case study. The investigation area is marked by the red cross (wetter3.de, 2018a).

5.1.2 Thermodynamic conditions in the atmospheric boundary layer

The two investigated days are generally characterised by fair weather conditions. It is mostly sunny during daytime with only few clouds, as can be seen in the measurements of global radiation at Schnarrenberg in Fig. 5.4a. The global radiation shows a diurnal cycle with a maximum near noon and some periods with lower values, caused by clouds. On 14 August and 15 August, respectively the temperature (Fig. 5.4b) reaches maximum values of 27 °C and 30 °C and shows a daily amplitude of more than 10 K. A conspicuous feature that appears both in the time series of global radiation and temperature is a minimum that occurs around 13:00 UTC on 15 August. This is connected to the precipitation event (Fig. 5.4e), which is caused by a convective cell that passed over the area at that time (Fig. 5.2). As we are interested in undisturbed conditions we chose the investigated period to end before the event. The beginning and end of the investigated period are marked in the figures by the dashed vertical lines.

The mean wind speed measured at Schnarrenberg in 12 m above the ground (Fig. 5.4c) shows a diurnal cycle on 14 August, starting with low values of less than 2 $\mathrm{m\,s^{-1}}$ in the morning, increasing to maximum values of more than 4 $\mathrm{m\,s^{-1}}$ around noon and decreasing again in the evening. From around 21:00 UTC onwards the wind speed starts to increase again, and stays at a relatively constant level between 3 $\mathrm{m\,s^{-1}}$ and 4 $\mathrm{m\,s^{-1}}$ until around 6:00 UTC on the 15 August. After that time the wind speed decreases slightly. The precipitation event is visible as distinct peak in wind speed. Wind directions (Fig. 5.4d) are rather constant from east-southeast in the morning of 14 August and turn to southeast until the morning of 15 August. After around 9:00 UTC the wind turns over west to north until the evening.

Attenuated backscatter from the ceilometer at Schnarrenberg is displayed in Fig. 5.5. On 14 August (Fig. 5.5a) backscatter increases in a layer adjacent to the surface, which grows in depth during the day. This indicates the evolution of the CBL with a high aerosol content, which grows up to a height of around 2 km asl around noon and temporarily even reaches up to 3 km asl in the afternoon around 17:00 UTC. Between 12:00 and 16:00 UTC, the CBL is sometimes capped by cumulus clouds. Shortly after sunset at 18:40 UTC, the height of the layer with high backscatter decreases. Throughout the night the properties of the airmasses below 3 km asl alternate between weak and stronger backscatter. After around 20:00 UTC an airmass with rather low backscatter dominates, which is replaced by an air mass with higher backscatter after around 21:00 UTC at a height between 1.5 km asl and 3 km asl. The higher backscatter can either be caused by higher aerosol content or higher relative humidity. Few clouds top the airmass with higher backscatter, with a cloud free period between around 22:00 UTC and 23:00 UTC. After around 2:00 UTC air with low backscatter appears, gradually penetrating downwards during the following hours, leading to a layer with low backscatter between around 0.8 km asl and 1.8 km asl. This layer is persistent until around 7:00 UTC. Above and below this layer backscatter is higher and clouds are visible at around 2.5 km asl. After 7:00 UTC backscatter is rather homogeneous and high up to 3 km asl. The rain event at 13:00 UTC is clearly visible as it extinguishes the backscatter signal at a low height.

The temporal development of the thermal stratification during the case study is displayed in Fig. 5.6. The graphic shows the potential temperature calculated from the MWR data. At the beginning of the investigated period, at noon the potential temperature is roughly constant up to

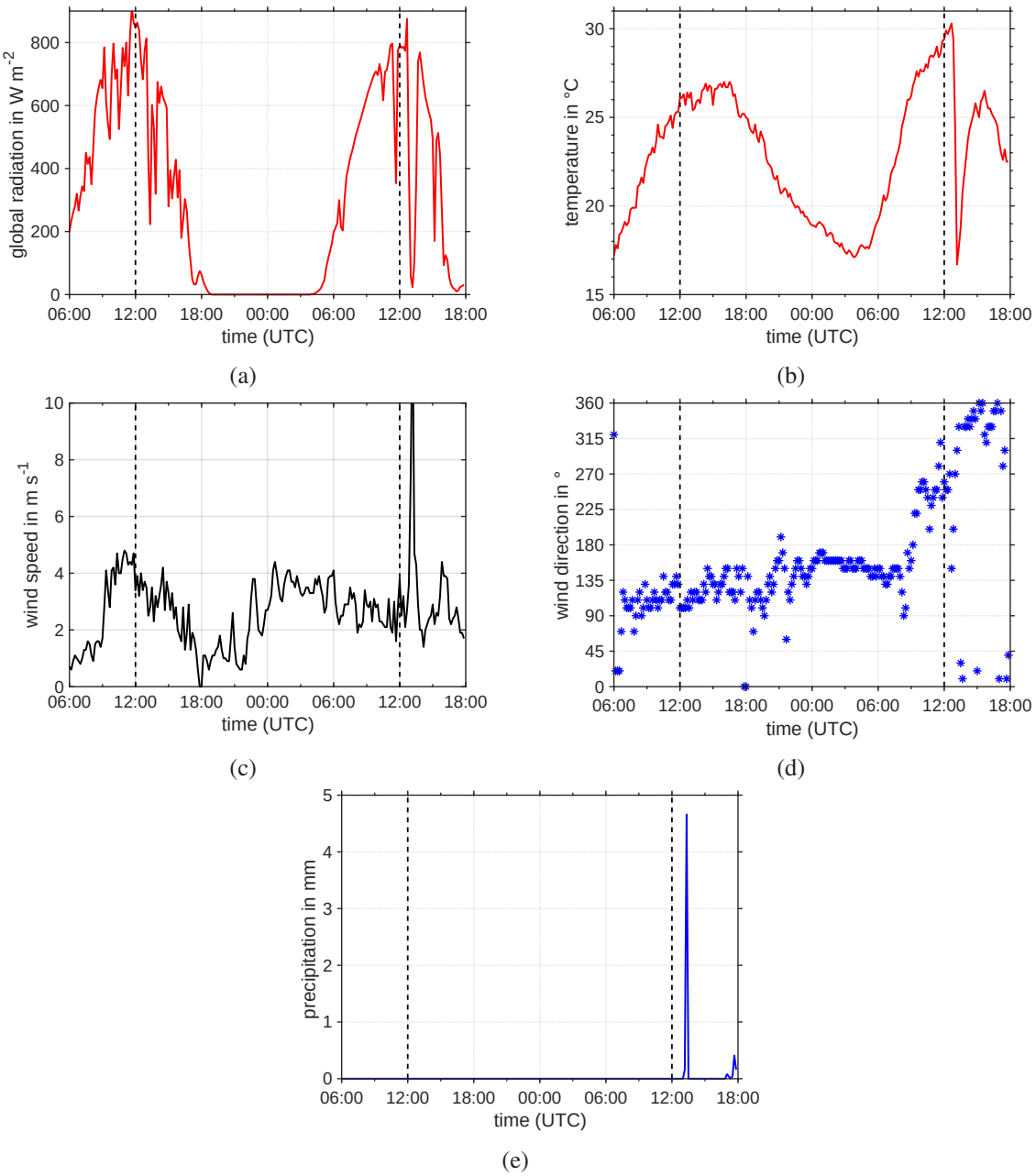

Figure 5.4: Near-surface data from Schnarrenberg. Measurements with 10 min resolution from the morning of 14 August until the afternoon of 15 August, time is given in UTC. The dashed black lines mark the investigated period of the case study. (a) global radiation, (b) temperature in 2 m height above ground, (c) mean horizontal wind speed and (d) wind direction, both measured 12 m above ground, (e) precipitation.

around 2000 m asl, from where it starts to increase with height. This neutrally stratified layer represents the CBL with a ML and acapping inversion on the top, which is also evident in the ceilometer measurements (Fig. 5.5a). The temperature in the whole layer increases slightly until 18:00 UTC (Fig. 5.6), when a colder, stably stratified layer starts to form near the ground. This nocturnal SBL starts to form shortly before sunset, grows in depth and strength throughout the night, and reaches up to around 1000 m asl at 3:00 UTC. The SBL stays relatively constant until 6:00 UTC in the morning, when its strength weakens but it starts to grow again up to around 1600 m asl at 9:00 UTC. Shortly after the surface inversion starts to form the potential temperature

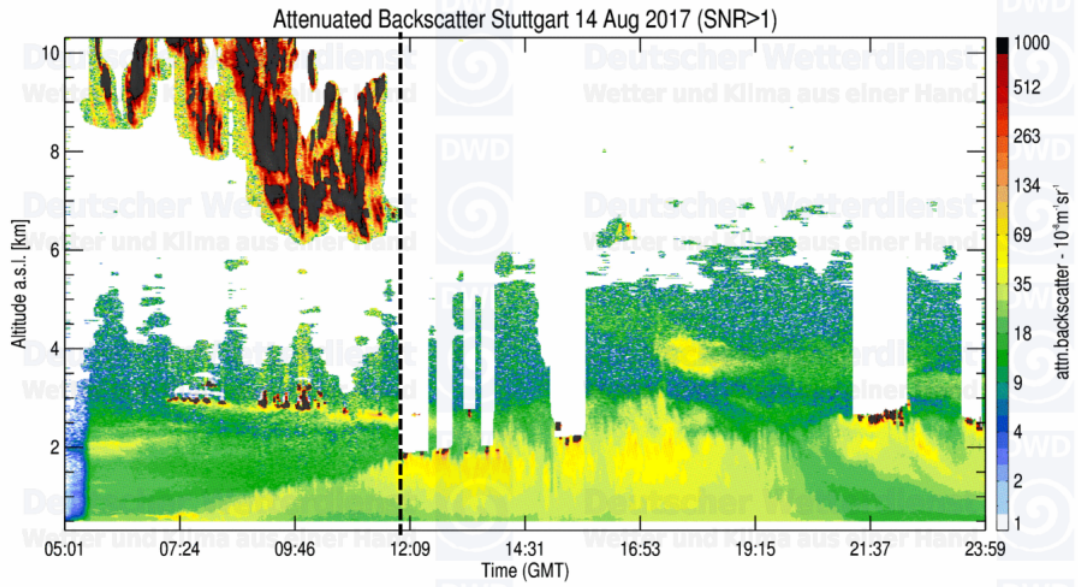

(a) 14 August

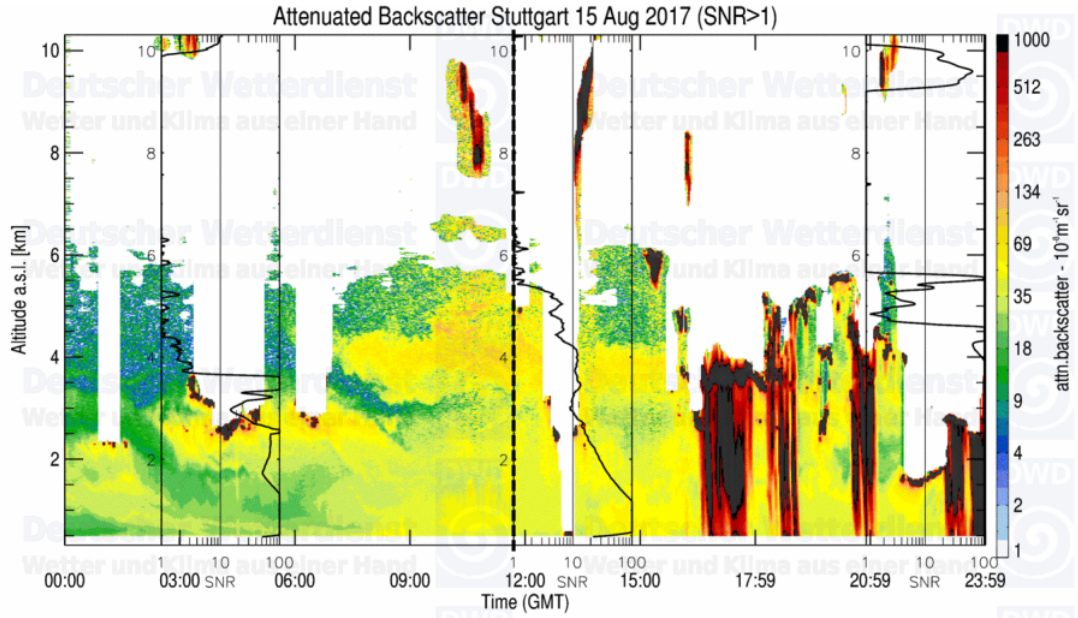

(b) 15 August

Figure 5.5: Attenuated backscatter from the ceilometer at Schnarrenberg (colour coded). The thick vertical dashed lines mark the beginning and end of the investigated period. Figures are provided by DWD (personal communication).

in the layer above increases compared to daytime. Between 20:00 UTC and midnight there is a layer of slightly lower potential temperature between about 1200 m asl to 2200 m asl. There is no clear evidence that the changes in temperature are linked to the air masses with different backscatter, as measured by the ceilometer (Fig. 5.5). After around 7:00 UTC the potential temperature increases in the SBL due to heating from below, and the developing CBL erodes the stable layer. By around 10:30 UTC the surface inversion is completely eroded and the potential temperature is rather constant with height within the ML of the CBL. Comparing the potential temperature in the CBL for the two days, it is evident that the temperature increased over the period, which is prob-

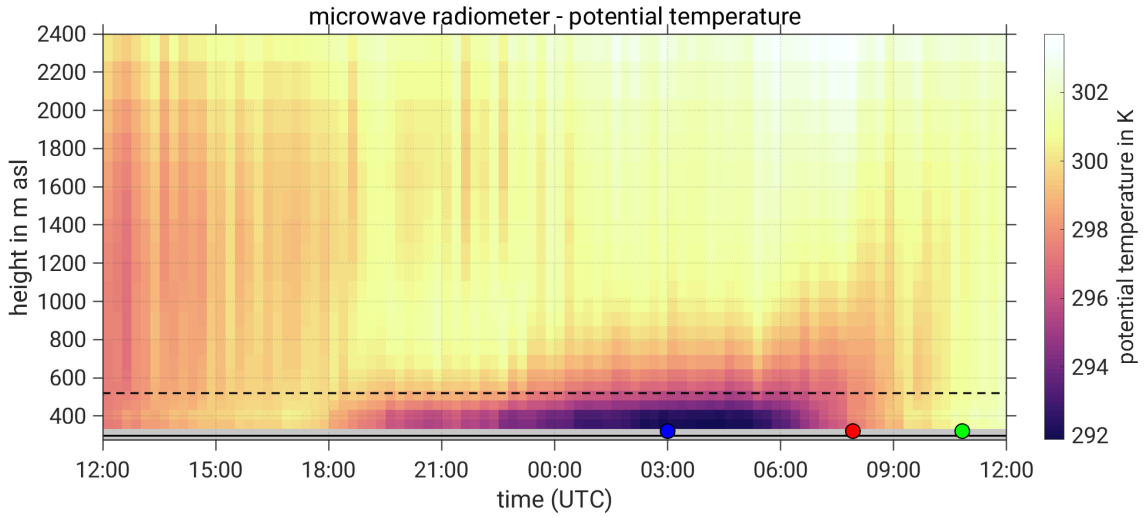

Figure 5.6: Evolution of potential temperature (colour coded) from microwave radiometer measurements during the case study from 14 to 15 August 2017. The coloured circles mark the radiosonde launching times, the dashed line indicates the mean ridge height of the surrounding hills and the solid line at the bottom marks the terrain height at the instrument location.

ably due to a change of airmass. This warming is also observed in the near surface measurements in Fig. 5.4b.

Three radiosondes were launched at Erwin-Schoettle-Platz during the investigated period, at 3:00 UTC, 7:55 UTC and 10:49 UTC on 15 August. The vertical structure of the thermal stratification observed in the MWR measurements (Fig. 5.6) can be examined in more detail, using the potential temperature from the radiosoundings in Fig. 5.7a. At 3:00 UTC the stable layer reaches up to 1700 m asl and consists of a strongly stable part below 700 m asl, i.e. a surface inversion of 400 m depth, and a weaker stably stratified part above. In the surface inversion, the vertical gradient of the potential temperature ($\frac{\partial\theta}{\partial z}$) is 2.25 K/100 m. Above, the gradient of the potential

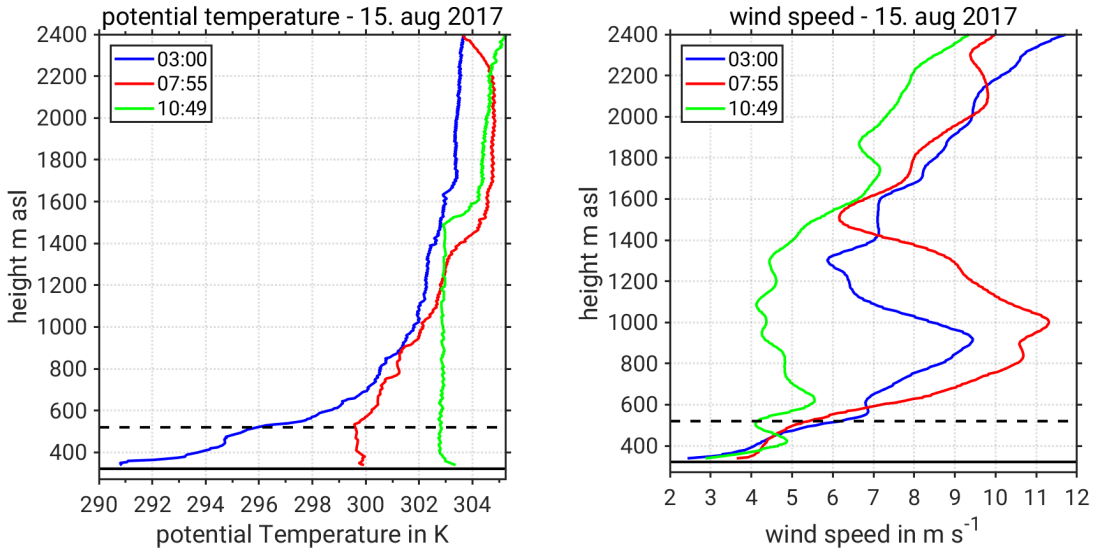

(a) (b)

Figure 5.7: Radiosoundings at Erwin-Schoettle-Platz on 15 August. The dashed line marks the mean ridge height of 520 m and the solid black line at the bottom indicates the terrain height at the launch site. Launching times are given in UTC.

temperature decreases with height, with the strongest curvature between 700 m asl and 1200 m asl. The radiosonde at 7:55 UTC shows a slightly unstable layer above the ground up to 500 m asl, and above a stable layer reaching up to 1700 m asl. The unstable layer at the bottom represents the developing CBL, which grows into the nocturnal stable layer. Above the stable layer the atmosphere warmed by about 2 K compared to the 3:00 UTC radiosounding, which agrees with the MWR measurements (Fig. 5.6). At 10:49 UTC the typical structure of a CBL has developed, with a unstably stratified surface layer (SL) ($\frac{\partial\theta}{\partial z} = -1\,\mathrm{K}/100\,\mathrm{m}$) in the lowest 100 m above the ground, and a neutrally stratified ML above, reaching up to 1500 m asl. Above there is a capping inversion layer ($\frac{\partial\theta}{\partial z} = 1\,\mathrm{K}/100\,\mathrm{m}$) with a depth of 100 m. The temperature above the CBL has changed little compared to the radiosounding at 7:55 UTC.

5.1.3 Temporal evolution of the horizontal wind

The temporal development of the horizontal wind at VTs 2 and 5 is depicted in Fig. 5.8. The two towers are chosen for their location in the middle of the valleys, i.e. they represent the flow within the valleys uninfluenced by the slopes, and also because they were measuring up to 2.4 km, i.e. higher than the VTs on the slopes.

In the CBL on 14 August, which reaches up to the highest measurement height of the VTs (Sect. 5.1.2), the horizontal wind is rather constant with height at both VTs. The wind speed is around $4\,\mathrm{m\,s^{-1}}$ from the southeast, and the wind direction turns slightly anticyclonic with height. Shortly before sunset at 18:40 UTC the horizontal wind near the surface decreases due to the evolution of the SBL (see Fig. 5.6). Around the same time the horizontal wind speed increases gradually from the top at 2400 m asl downwards at higher altitudes (Fig. 5.8). Around 20:00 UTC a maximum value of around $12\,\mathrm{m\,s^{-1}}$ is reached in a height between 1900 m asl and 2400 m asl. After a temporary decline in this layer the wind speed increases again after 22:00 UTC. These changes in horizontal wind speed could be related to the air mass changes visible in the ceilometer measurements (Fig. 5.5a, Sect. 5.1.2), although it is not possible to directly link changes in backscatter and horizontal wind speed.

Between 23:00 UTC and 2:00 UTC a low-level jet (LLJ) (see Sect. 2.1.3) forms directly above ridge height, at around 600 m asl, with maximum wind speeds of $7\,\mathrm{m\,s^{-1}}$. Shortly after 3:00 UTC, the horizontal wind speed significantly decreases between 900 m asl and 2000 m asl at both sites (Fig. 5.8). This decrease occurs rather simultaneously to the occurrence of an air mass with low backscatter (Fig. 5.5a, Sect. 5.1.2). At the same time, the wind speed increases between around 600 m asl and 800 m asl, resulting in a wind profile strongly resembling an LLJ. While an LLJ most commonly forms due to acceleration of the wind due to loss of friction in the SBL (Sect. 2.1.3), this LLJ profile forms when the wind accelerates in lower levels and the wind above decreases simultaneously. The LLJ stays constant until around 7:00 UTC in the morning and is nicely visible in both VTs, as well as in the radiosoundings (Fig. 5.7b). Its spatial extent is analysed in Sect. 5.1.4.

After about 7:00 UTC, the height of the LLJ maximum rises and is about 1300 m asl shortly before 9:00 UTC (Fig. 5.8). The LLJ maximum roughly coincides with the strongest gradient of potential temperature, as can be seen in Fig. 5.6 and 5.7a. After 9:00 UTC, the LLJ is neither recognisable at the VT sites, nor in the last radiosounding at 10:49 UTC (Fig. 5.7b). Starting at 8:00 UTC a

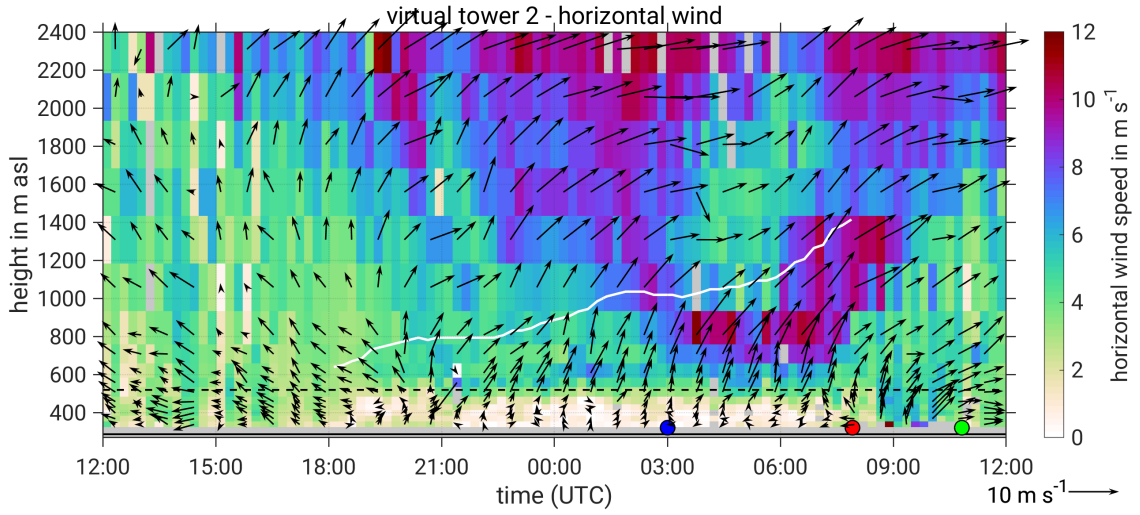

(a) VT 2 - opening of Stuttgart basin

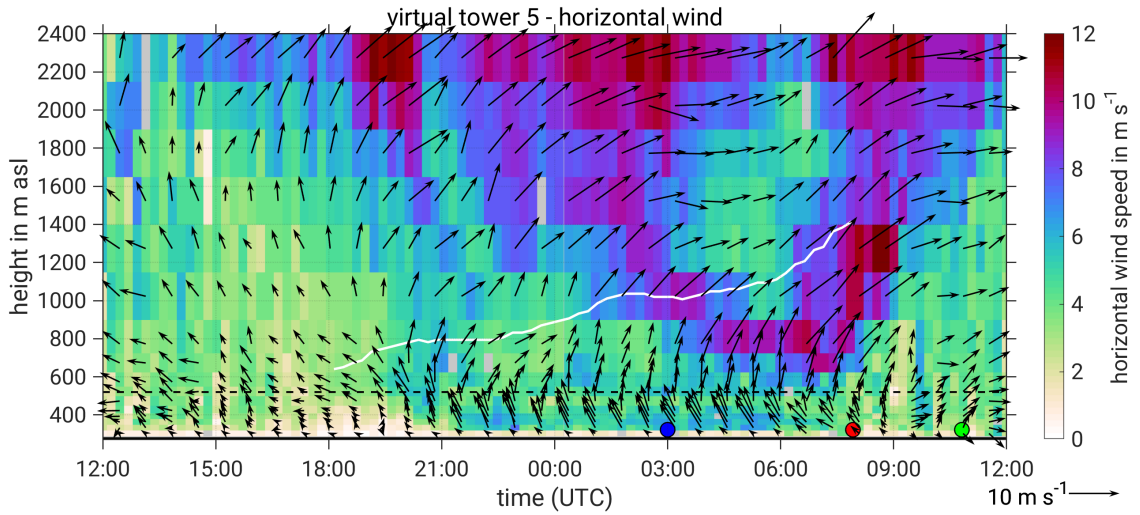

(b) VT 5 - Neckar valley

Figure 5.8: Evolution of horizontal wind profiles in the Neckar valley and the opening of the Stuttgart basin. The colour shading shows the horizontal wind speed at every 10 s measurement interval, grey fields are empty due to filtering. The arrows represent wind speed and direction at every third measurement interval, with north upwards and east to the right. Radiosonde launching times are indicated by the coloured circles. The height of the SBL as observed by the Ceilometer is marked by the white line. The dashed black line marks the mean ridge height of 520 m asl and the solid black line at the bottom indicates the height of the terrain at the VT location. The investigation time is from 12:00 UTC on 14 August until 12:00 UTC on 15 August, sunset was at 18:40 UTC and sunrise at 4:15 UTC.

layer with relatively constant horizontal wind of around 5 m s^{-1} from southeast develops in the CBL (Fig. 5.6). At 10:49 UTC, the CBL is well developed, with an unstable surface layer and a deep well-mixed layer, capped by an inversion at 1500 m asl (Sect. 5.1.2, Fig. 5.7a). The top of the CBL is visible in the VTs as the height where the wind speed rapidly increases with height compared to the more constant horizontal wind speed in the CBL below.

Profiles of horizontal wind are similar at VT 2 and VT 5 during the day in the CBL (Fig. 5.8), as well as during the night above the ridge height. However, below the ridge height considerable differences between the two VTs occur in the SBL. Around sunset at 18:40 UTC the wind below

the ridge height at both VTs decreases due to the development of the SBL and the end of downward mixing of momentum.

At VT 2 at the opening of the Stuttgart basin the horizontal wind speed stays weak during the night at around 1 m s^{-1} (Fig.5.8a). The wind direction varies, but southwesterly components dominate. This means that a light outflow from the Stuttgart basin into the Neckar valley takes place during the stably stratified period. In the morning after 8:00 UTC, when the CBL starts to form, the wind becomes stronger again, and the direction turns to the wind direction above, as momentum is transported downward. At VT 5 in the Neckar valley, the horizontal wind below the ridge height decreases around sunset as well as at VT 2, but shortly after 20:00 UTC the wind starts to increase again (Fig.5.8b). During the whole night until 7:00 UTC in the morning there is a strong and persistent wind of up to 7 m s^{-1}, blowing steadily from south-southeast. Between 21 UTC and 3 UTC the wind below ridge height is even stronger than the wind at ridge height. This corresponds to a thermally-driven down-valley wind (Sect. 2.3) in the Neckar valley. Once the stratification becomes unstable and a CBL starts to form at around 8:00 UTC (Fig. 5.6), the down-valley wind weakens and eventually is replaced by a flow from the southwest.

Three general flow patterns are observed at VT 2 and VT 5. In the CBL, downward momentum transport leads to similar wind speed and direction, with the winds at the surface a little weaker and slightly rotated cyclonically to the wind above the ridge height (Sect. 2.3). In the SBL an orographically induced, thermally driven down-valley wind develops below the ridge height in the Neckar valley (Sect. 2.3). These flow patterns occur as described by Whiteman and Doran (1993). Above the ridge hight an LLJ is observed in the SBL at both sites, which seems to be independent from the orography. While the flow in the CBL is coupled by turbulence due to convection the flow in the SBL is decoupled, with down-valley wind below, and LLJ above the ridge height.

5.1.4 Spatial distribution of the horizontal wind

To investigate the spatial extent of the phenomena observed in Sect. 5.1.3, horizontal sections of all available Doppler-lidar measurements were plotted at two heights, one below and one above the mean ridge height for stable and unstable conditions (Fig. 5.9). Every plot shows the horizontal wind measured at all VTs within one complete scan cycle (see Sect. 4.2.1), and additionally measurements from the Windcube lidar at the same time.

To take into account the observed differences of the horizontal wind above and below ridge height under stable conditions, two height levels are chosen to represent the different flow characteristics above and below the ridge height. 410 m asl is taken as the lower level, as it is well below the ridge height, but also high enough above the ground at all sites for not to be disturbed by local effects (e.g. buildings). The down-valley wind in the Neckar valley, occurs quite pronounced at this height (Fig. 5.8b). As higher level, 690 m asl was chosen, because in this height the LLJ could be observed at VT 2 and VT 5 (Fig. 5.8). Although the maximum of the LLJ appeared at a height around 800 m asl, 690 m asl was selected, because of the higher data availability of the VTs and the Windcube.

Horizontal sections were plotted at three times, to investigate the wind field under different stratification. Figure 5.9a displays the wind under stable conditions (see Fig. 5.6) around 0:30 UTC

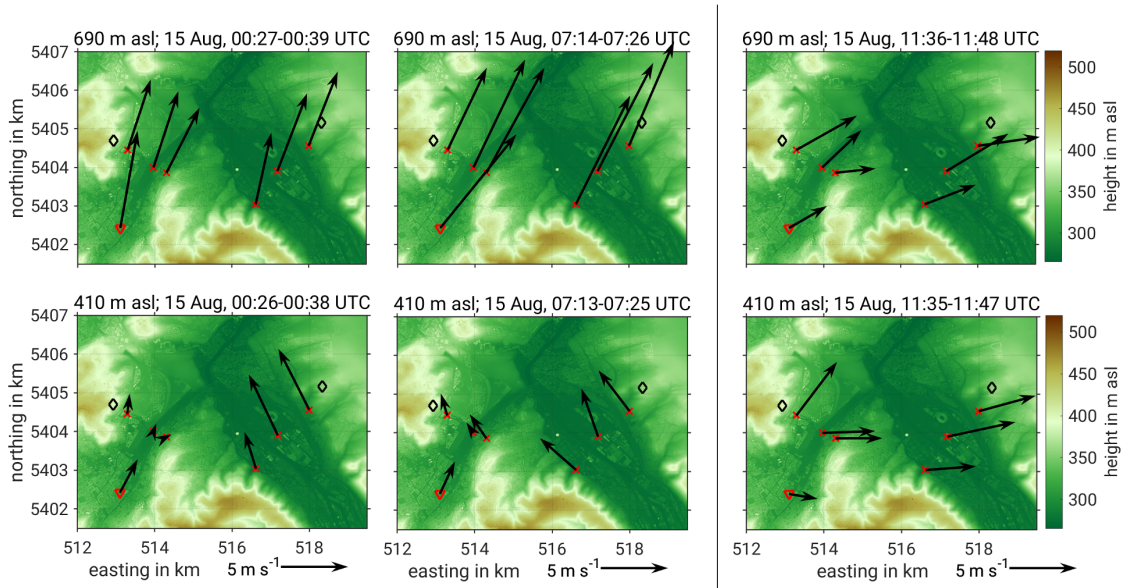

(a) around 0:30 UTC (b) around 7:15 UTC (c) around 11:45 UTC

Figure 5.9: Horizontal distribution of the horizontal wind in the investigation area. Measurements of horizontal wind at all six VTs and the Windcube displayed as vectors with origin at the measurement site, red crosses mark the VTs, red triangle the Windcube site. The colour shading shows the topographic height. The top figures show wind above the ridge height, at a height of approx. 690 m asl, the bottom figures are at 410 m asl, which is below the ridge height. All plots show measurements from one complete scan cycle.

because at this time a LLJ wind profile is observed for the first time in the night at VT 2 and VT 5, and also the down-valley wind is present at VT 5 (Fig. 5.8). Figure 5.9b shows the horizontal wind around 7:15 UTC, because at this time the LLJ is most pronounced in the higher level at VT 2 and VT 5 (Fig. 5.8), and the nocturnal down-valley wind systems are still present. In Fig. 5.9c) the wind is displayed around 11:45 UTC, when the two measurement heights are within the CBL (Fig. 5.6, 5.7a and 5.8).

At 0:30 UTC the LLJ can be observed at all sites above the ridge height (Fig. 5.9a). Horizontal wind speed and direction are similar, around 7 m s^{-1} from south-southwest, at all measurement locations. This indicates that the LLJ is a mesoscale phenomenon in the area, independent from the local topography. Below the ridge height a distinct down-valley wind of around 5 m s^{-1} occurs at VT 4, 5 and 6 in the Neckar valley. At VT 1, 2 and 3 a weak outflow of the Stuttgart basin is visible. In the city centre the Windcube shows an inflow into the basin from the Nesenbach valley. The winds at the low levels depend on the locations in the valley and are independent from the LLJ above, i.e. the winds at the low levels are decoupled from the wind above the ridge height.

At 7:15 UTC the LLJ is still visible at all sites above ridge height (Fig. 5.9b). The wind blows strongly from southwest with a wind speed of around 9 m s^{-1}. Below the ridge height the down-valley wind in the Neckar valley is still present, although it is slightly weaker than at 0:30 UTC. This could be connected to the evolution of a CBL that starts around that time (Fig. 5.6 and radiosounding at 7:55 UTC in Fig. 5.7a). At the opening of the Stuttgart basin at VT 1, 2 and 3 no outflow is observed at this time (Fig. 5.9b). Instead the wind increased slightly and turned to southeast, possibly influenced by the down-valley wind in the Neckar valley. In the basin, an

outflow of the Nesenbach valley is still observed at the town hall. The winds at the low level are still decoupled from the winds above ridge height.

At 11:45 UTC the horizontal wind in the CBL is generally similar in speed (around $5\,\mathrm{m\,s^{-1}}$) and direction (westerly) at all measurement locations and both heights (Fig. 5.9c). This is due to vertical mixing of momentum in the CBL. However, the variation in wind direction between the different locations is considerable probably due to turbulence within the CBL.

5.2 Topographic influence on the horizontal wind field

In the case study presented in Sect. 5.1, different flow characteristics are identified in the investigation area. During daytime, the horizontal wind is similar at all heights within the CBL. Under stable conditions during nighttime, a decoupling of the horizontal flow below and above the ridge height occurs. Below the ridge height the wind is strongly influenced by topography and mainly unaffected by the large-scale wind: a down-valley wind forms in the Neckar valley, a weak outflow from the Stuttgart basin occurs, and a down-valley wind from the Nesenbach valley is observed within the basin. Above the ridge height an LLJ exists throughout the investigation area.
The case study reveals a considerable influence of the topography on the wind field, which depends on atmospheric stratification and height. In the following, this topographic influence is investigated statistically for all available days of the campaign (36 in total, see Sect. 3.1). While the case study is characterised by undisturbed fair weather conditions and a moderate south-westerly large-scale wind, all days are included in the statistical analysis, such as synoptically influenced days and rain events.

5.2.1 Stratification classification

The atmospheric stratification controls the vertical momentum transport in the ABL (Sect. 2.1). As has been shown in the case study (Sect. 5.1), the atmospheric stratification has a strong impact on how the topography influences the wind field. Therefore, an objective criterion is defined to distinguish between stable and convective conditions.
The classification into stable and unstable/neutral situations is based on potential temperature profiles derived from MWR measurements (Sect. 3.3.1). The difference of the potential temperature between 200 m above the device and at the height of the device is calculated. Situations are regarded as stable if the difference exceeds 0.5 K, This empirical threshold is based on visual inspection of the time series of the potential temperature difference and on the profiles themselves. Due to the coarse vertical resolution and the uncertainty of the MWR profiles, convective conditions are not always linked to negative temperature differences.
As data from the MWR is available for only 17 days during the measurement period of the VTs (Tab. 3.1), the classification of the stratification can only be made for this time period. VT data of these 17 days are classified and used for the analyses in Sect. 5.2.3 and 5.2.4.

5.2.2 Height dependence of the topographic influence

In this section, the height dependence of the topographic influence on the horizontal wind field is investigated. As evident in the case study (Sect. 5.1), the topographic influence depends on height - in particular during stable conditions. To assess how strongly the different height levels of the VTs are influenced by the topography the spatial variability of the horizontal wind is examined. The idea is that at low heights the horizontal wind at the different VTs differs strongly due to the different topography surrounding the sites. At higher altitudes the horizontal wind is less affected by the topography and similar at all locations. To assess the spatial variability, spatial standard deviations of the hourly averaged horizontal wind components u and v are calculated. The spatial standard deviations are calculated for every timestamp and common height level over all VTs

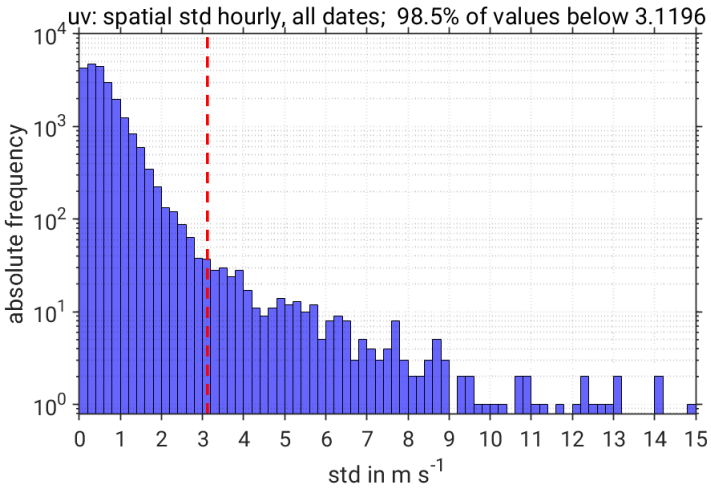

Figure 5.10: Histogram of the spatial standard deviations of the horizontal wind components u and v of all timestamps and heights. The absolute frequency is displayed logarithmically on the y-axis and the standard deviations are sorted into bins of 0.2 m s^{-1} width. Taking into account only the lowest 98.5 % of the values leads to the threshold of 3.12 m s^{-1}, marked by the dashed red line. 245 values i.e. 2.18 % of all values are removed by this filtering.

(for hourly averaging and common height levels see Sects. 4.2.4 and 4.2.5). For example, the spatial standard deviation of the u wind component at 400 m asl at 6:00 UTC on 15 August 2017 is the standard deviation of the 6 values of the u wind component from all VTs at 400 m asl at this timestamp.

Spatial variability, however, is not only caused by topographic effects, but also by turbulence, especially in the CBL during daytime. Turbulence in the CBL may lead to high, temporally fluctuating spatial standard deviations, whereas topographic effects are expected to cause lower, but more persistent spatial standard deviations. The valley wind in the Neckar valley and the outflow from the Stuttgart basin are generally evident at the 3 VTs each during stable conditions (VTs 3 to 6 for the valley wind and VT 1 to 3 for the outflow). Turbulence, however, may cause different wind directions at all 6 VTs. To focus on the topographic influence and to reduce the effect of turbulence, the highest values of the calculated spatial standard deviations are filtered out. Figure 5.10 shows the histogram of the spatial standard deviations of u and v of all timestamps. Keeping the lowest 98.5 % of the standard deviations of both u and v of all timestamps, i.e. filtering out the highest 1.5 %, gives reasonable results without losing too much data (2.18 % are lost in total). Taking the lowest 98.5 % of the values leads to a threshold of 3.12 m s^{-1} below which the standard deviations of both wind components are taken into account. The threshold is marked in the figure by the dashed red line. The spatial standard deviations that remain after filtering out the highest 1.5 % are used for the determination of the height dependence of the topographic influence. From these values daily composites (Fig. 5.11) and mean profiles are calculated (Fig. 5.13). In both figures the lowest common height level (300 m asl) is not taken into account, as it only represents one VT. The terrain at the site of VT 1 was higher than at the other sites, so the lowest measurement height of VT 1 is represented in the third common height level at 370 m asl (Sect. 4.2.5, Fig. 4.10). As the lowest measurement heights are influenced strongest by local effects at the ground, the spatial standard deviations at the third height level are increased due to the lowest measurement height of VT 1. Therefore, the lowest measurement height of VT 1 is not taken into account for

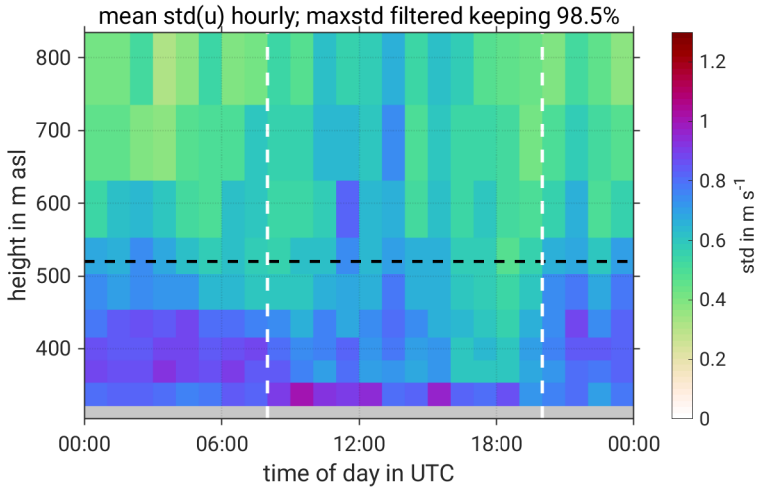

(a) spatial standard deviations of u

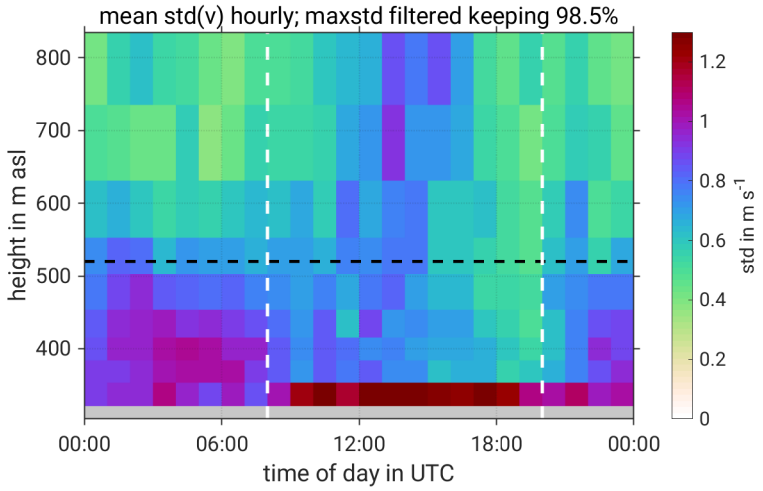

(b) spatial standard deviations of v

Figure 5.11: Daily composites of the spatial standard deviations of the horizontal wind components u (a) and v (b) of all timestamps. The dashed black line indicates the mean ridge height and the vertical, white dashed lines mark the average time, when stratification switches between stable and unstable/neutral near the surface (Sect. 5.2.1).

the calculation of the spatial standard deviations at the third common height level, and the values at the second common height level represent the lowest level above the ground.

Figure 5.11 shows daily composites of the profiles of the spatial standard deviations of u and v. Both figures show two distinct regimes, one during daytime between around 9:00 UTC in the morning until the evening at around 20:00 UTC and the other one during nighttime between around 20:00 UTC and 9:00 UTC. The two regimes are related to atmospheric stratification and roughly separated by the mean time when the stratification switches from stable to unstable/neutral in the morning around 8:00 UTC and from unstable/neutral to stable in the evening around 20:00 UTC (for the determination of atmospheric stratification see Sect. 5.2.1). This means that the first regime occurs in the CBL during daytime and the second regime in the SBL during nighttime.

The spatial standard deviations during daytime resemble the growth of the CBL. In the morning, a layer with high spatial standard deviations of around $0.8\,\mathrm{m\,s^{-1}}$ roughly reaches up to the ridge height. This layer grows upwards and reaches the highest measurement height at around

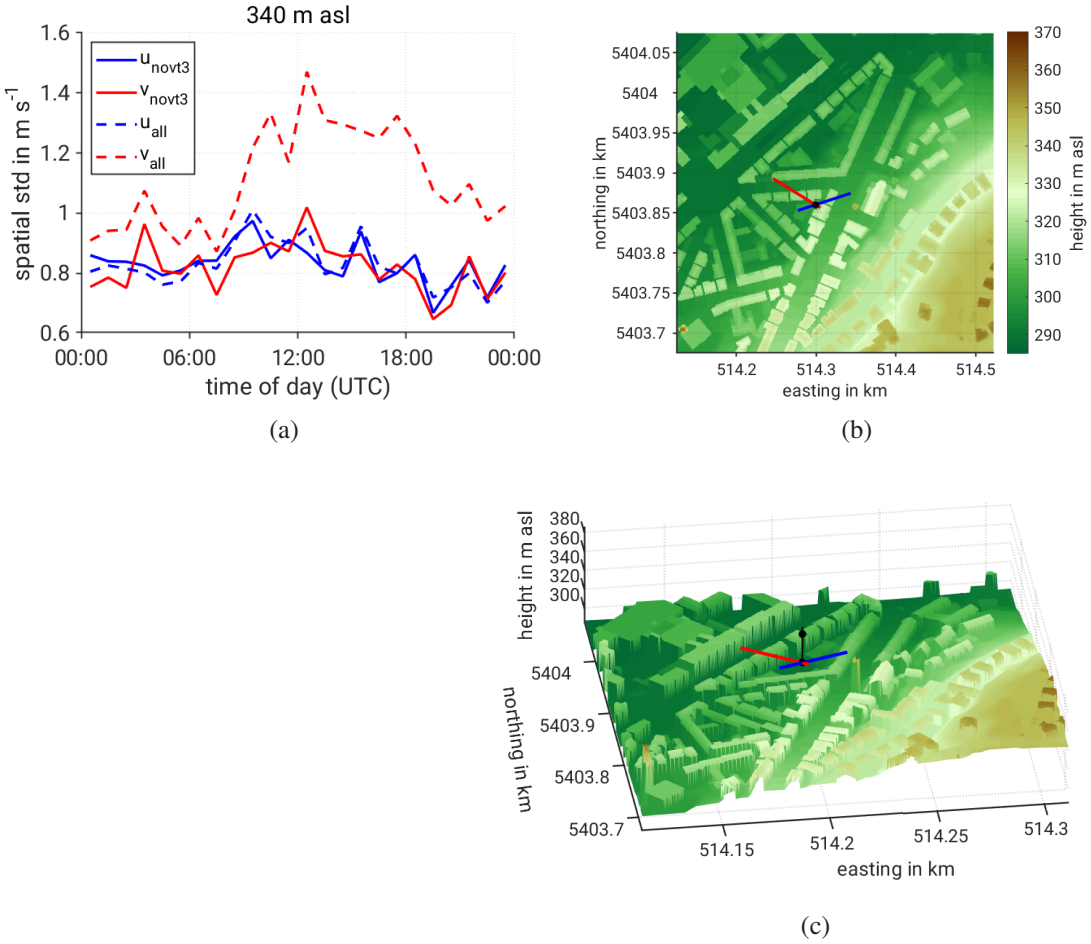

Figure 5.12: Origin of the high spatial standard deviations in the lowest level (Fig. 5.11). (a) shows the daily composite of spatial standard deviations of u (blue) and v (red) at the lowest measurement level. Dashed lines show the spatial standard deviations for all VTs as in Fig. 5.11, solid lines show the spatial standard deviations without VT 3. (b) and (c) display the topography around the lowest two measurement heights of VT 3 (black dots), range gates corresponding to the lowest measurement height are drawn as lines for HYB (blue) and WTX (red).

13:00 UTC. After 17:00 UTC, the values rapidly decrease to around 0.5 m s^{-1} at all levels and remain low until the stratification switches to stable.

During daytime, high spatial standard deviations occur at the lowest height (around 1 m s^{-1} for u and 1.3 m s^{-1} for v). This is most likely related to turbulence and local effects induced by buildings. These high spatial standard deviations of v at the lowest level are caused by the measurements at VT 3 (Fig. 5.12a). The spatial standard deviations of v are very large if they are calculated from all available VTs. In particular during daytime the difference is large, when the spatial standard deviation of v is nearly twice as high as for u. If VT 3 is not considered in the calculation, the spatial standard deviations are similar for u and v. The reason for this is probably the close proximity of the lowest measurement height of VT 3 to the surrounding buildings (Fig. 5.12b,c). The rooftops of the houses are only around 20 m below the measurement height, southeast of the VT the terrain rises and a church tower is located around 50 m east of the VT, with a height similar to the lowest measurement height. Therefore, influences from the buildings on the flow are expected to be strongest at wind from southerly to easterly direction. During nighttime down-valley flow is expected to occur commonly (Sect. 2.3), which would blow from southwest at the position of

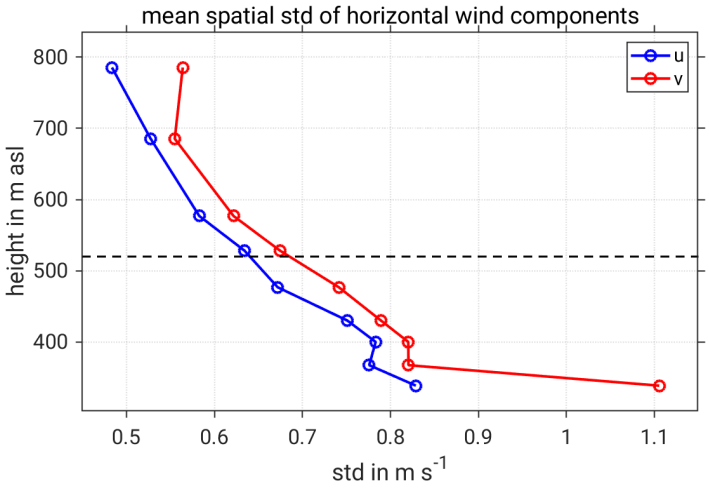

Figure 5.13: Mean vertical profiles of the spatial standard deviations of the horizontal wind components u and v of all timestamps. The dashed line indicates the mean ridge height.

VT 3 (see Fig. 3.1). Southwesterly down-valley wind would be little affected by the buildings, explaining the lower spatial standard deviations during nighttime. During daytime the wind direction is expected to be more variable due to downward momentum transport in the CBL (Sect. 2.3). Wind from southerly to easterly direction during daytime is expected to be strongly influenced by the topography and increase the spatial standard deviations. If the wind at VT 3 behaves in the expected manner is analysed in Sect. 5.2.3.

During nighttime, the spatial standard deviations are generally much larger below the ridge height than above. Above the ridge height the values are decreasing with height until around 650 m asl where they reach a minimum of around 0.5 m s^{-1}. Below the ridge height, between 350 m asl and 450 m asl, the spatial standard deviations have a maximum of 0.9 m s^{-1} for u and 1 m s^{-1} for v. The behaviour during stable nighttime conditions shows a significant topographic influence of the valleys on the flow below the ridge height, whereas the wind above is less influenced and more similar at all locations. During convective daytime conditions, no influence of the topography is evident in the figures, as possible influences are superposed by convection. This agrees with the findings of the case study (Sect. 5.1), for which the horizontal wind is roughly constant with height in the CBL and similar at all locations.

The mean profiles of the spatial standard deviation of u and v in Fig. 5.13 show a general decrease with height. In accordance with the daily composites (Fig. 5.11) the highest values occur at the lowest level (Fig. 5.13). At 400 m asl, the spatial standard deviations have a local maximum for both u and v. Above 400 m asl the values decrease monotonically until 685 m asl, where there is a minimum of the spatial standard deviations of v. This shows that the topography influences the horizontal wind field below the ridge height significantly, whereas the wind above is less influenced.

Based on these results, two height levels are determined for the further statistical analysis of the horizontal wind: the first height level shall represent a height where the wind is strongly influenced by topography, while the second height level shall reflect the ambient wind, which is mostly unaffected by the topography. The level at 400 m asl is chosen as the topographically influenced height level, as it shows high spatial standard deviations during stable conditions and a local max-

imum in the mean profiles. The second height level, representing the ambient wind, is chosen at 685 m asl, because the spatial standard deviations are considerably lower than below ridge height and the mean profile of v shows a local minimum. It is likely that the spatial variability of u and v would decrease even further with height. However, as the maximum common height level of all 6 VTs is below 800 m asl, this cannot be confirmed.

5.2.3 Distribution of wind directions

The distribution of horizontal wind under stable and unstable/neutral conditions at the two height levels at the different locations are analysed based on wind roses. Figure 5.12 shows wind roses of the horizontal wind at 685 m asl, i.e. at the level reflecting the ambient wind, at VTs 2 and 5 under stable (Fig. 5.14a,b) and unstable/neutral (Fig. 5.14c,d) conditions. To distinguish the stratification, the criterion described in Sect. 5.2.1 is used. Under stable conditions, the distribution of ambient wind direction and speed are similar at VT 2 and VT 5 (Figs. 5.12a,b). Varying wind directions occur, while westerly components are slightly dominating and northerly to easterly components are rare. Also under unstable/neutral conditions the ambient wind distributions at the two VTs show a similar behaviour (Figs. 5.14c,d). Northwesterly to southwesterly wind components dominate. The wind speed distributions are quite similar at the two locations. The similarity of the wind roses of the ambient wind at the two different locations under both stable and unstable/neutral conditions is in agreement with the results from Sect. 5.2.2.

The distributions of horizontal wind at 400 m asl vary considerably at the different locations under stable conditions (Figs. 5.15, 5.16). In the Stuttgart basin and in the outflow area (Windcube and VTs 1, 2 and 3, Fig. 5.15) the wind speed is generally weaker at 400 m asl (most values between 0 m s^{-1} to 2 m s^{-1}) than at 685 m asl (most values between 4 m s^{-1} to 6 m s^{-1}), as expected due to surface friction. Southwesterly wind prevails at all locations, while other wind directions occur considerably less frequent. At the Windcube site in the city centre of Stuttgart (Fig. 5.15c) southwesterly wind is observed in around 32 % of all cases, and 60 % of the time the wind comes from the southwestern sector. These predominant winds are directed from the Nesenbach valley towards the opening of the Stuttgart basin (See Fig. 3.1). This indicates the regular occurrence of a down-valley wind in the basin, probably linked to the down-valley wind in the Nesenbach valley. The general dominance of southwesterly winds at the opening of the Stuttgart basin, at VTs 1, 2 and 3 (Figs. 5.15a,b,d) also indicates the regular occurrence of down-valley winds at the basin opening under stable stratification, resulting in an outflow from the basin. Although similar wind directions prevail at the 3 VTs, some differences occur. At VT 1 (Fig. 5.15a) the distribution is broader and south-southwesterly wind dominates. This is probably related to the topography around the location of VT 1 (Fig. 3.1), with the slopes of the Stuttgart basin shielding flow from the southwest and the widening of the basin towards the Neckar valley leading to horizontally divergent flow. At VT 2 (Fig. 5.15b) the dominating wind directions are south-southwest to west-southwest, showing frequent outflow of the basin. At VT 3 (Fig. 5.15d) southwesterly wind dominates clearly, and more southerly directions are less frequent, probably due to the vicinity of this VT to the southeastern slope of the basin, which affects the outflow at this position (Fig. 3.1).

In the Neckar valley, south-southeasterly wind dominates under stable conditions as visible at VTs 4, 5 and 6 (Fig. 5.16), i.e. a down-valley wind exists (see Fig. 3.1). At VT 4 (Fig. 5.16c) the

distribution of wind directions is relatively broad. Besides the down-valley direction, also westerly directions are frequent, which is probably due to the location of VT 4 at the western slope of the Neckar valley, where flow is also affected by the slopes and the outflow of the Stuttgart basin. At VT 5, in the middle of the Neckar valley (Fig. 5.16a), the down-valley wind from south-southeast to southeast dominates. Down-valley wind from south-southeast (28 %) and southeast (12 %) occurs 40 % of the time. The down-valley wind at VT 5 is considerably stronger than at the other locations in the Stuttgart basin and at VT 4, with the most frequent values between 4 m s^{-1} to 6 m s^{-1}. At VT 6 (Fig. 5.16b) the down-valley wind is also very pronounced and strong, similar to VT 5. The main wind directions are a little more southerly than at VT 5 which is probably due to the slight widening of the valley at the location of VT 6, which causes slight divergence in the

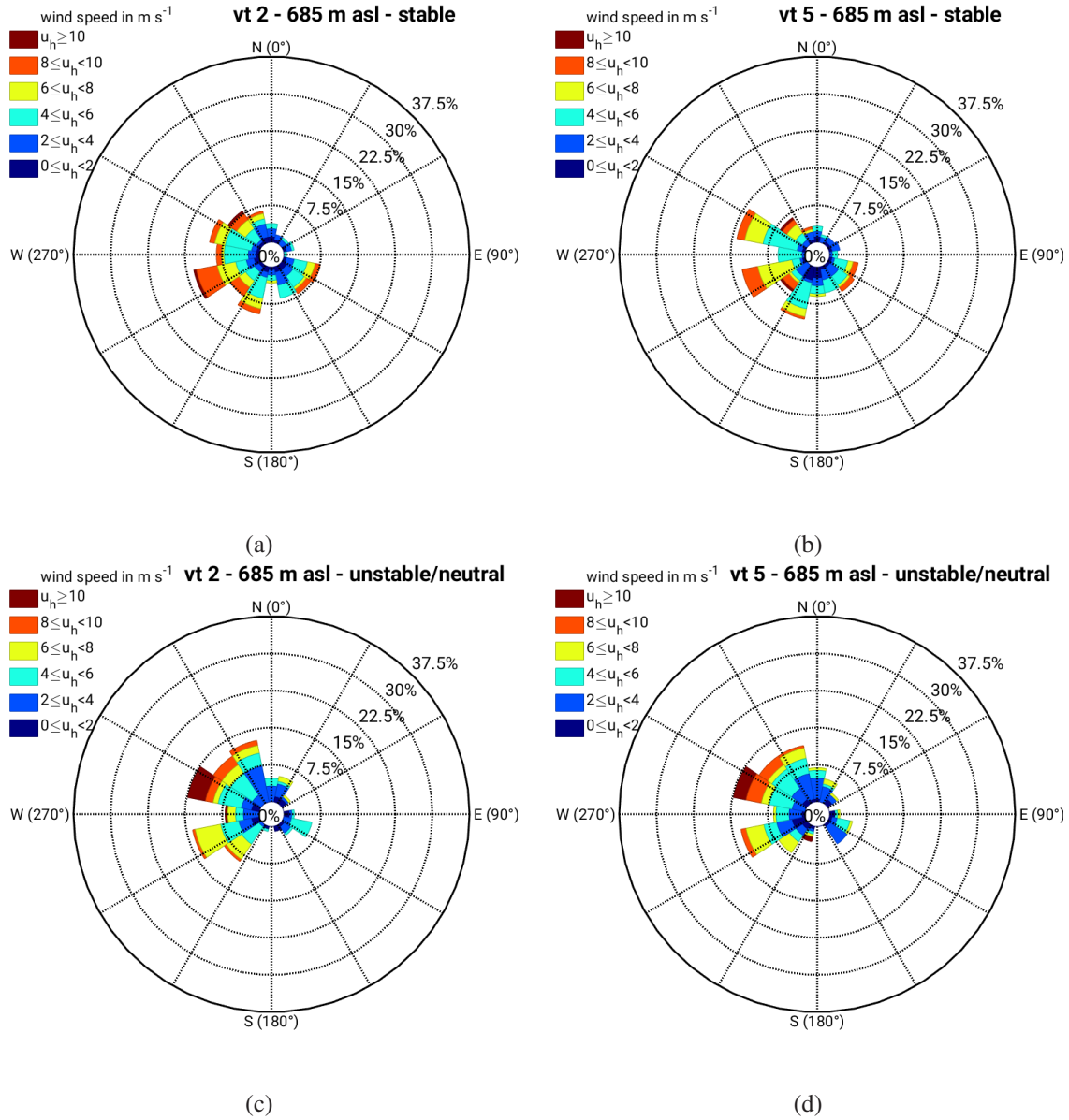

Figure 5.14: Wind roses at 685 m asl under stable conditions (a and b) and unstable/neutral conditions (c and d) at VT 2 (left) and VT 5 (right). Wind directions are divided into 16 sectors of 22.5° width and horizontal wind speed in 2 m s^{-1} bins. Data from 17 days are shown.

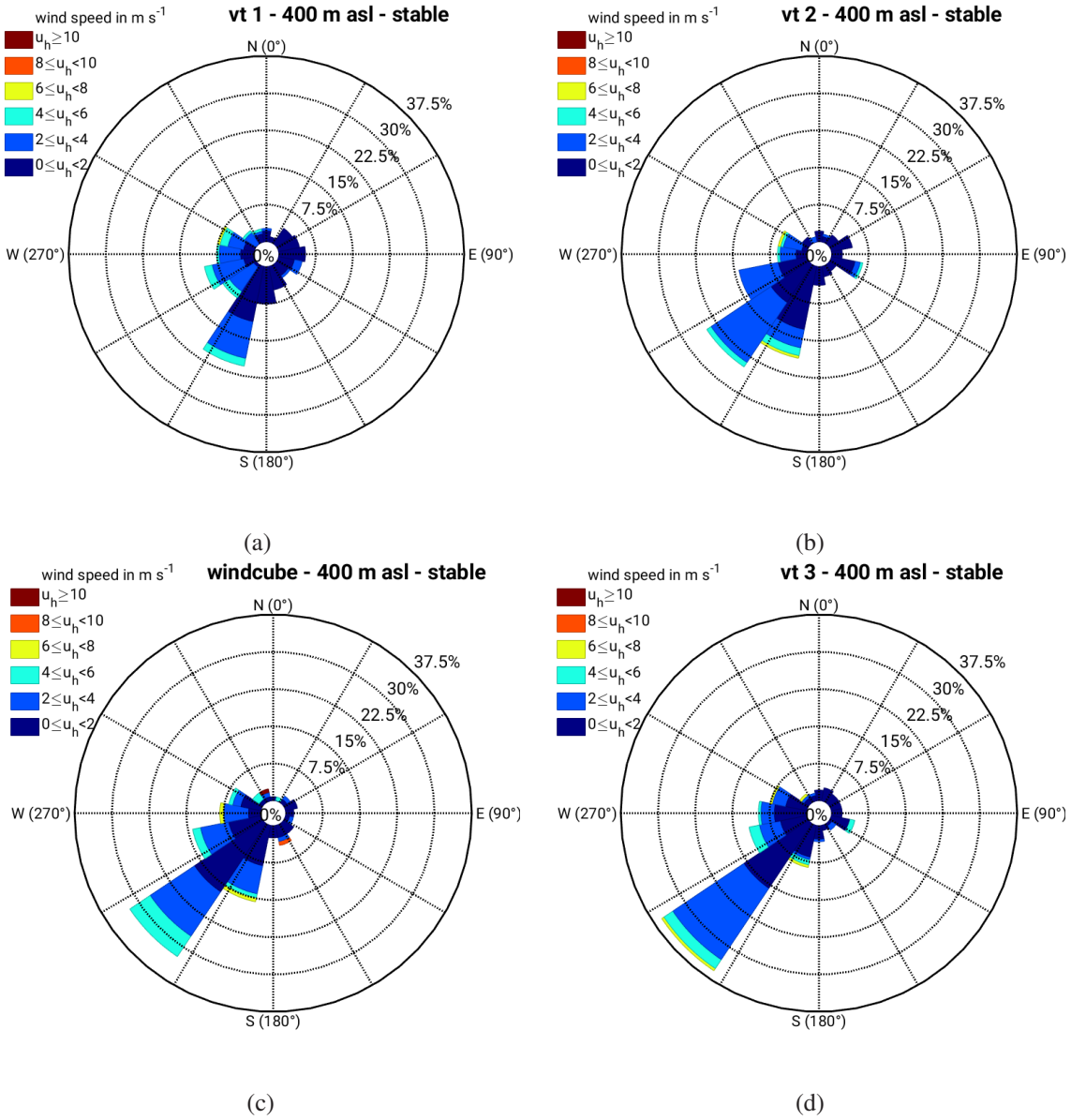

Figure 5.15: Wind roses at 400 m asl under stable conditions in the Stuttgart basin, at the Windcube (c) and at the opening of the basin at VTs 1 to 3 (a, b, d). Wind directions are divided into 16 sectors of 22.5° width and horizontal wind speed in 2 m s^{-1} bins. Data from 17 days are shown.

horizontal flow. These strong down-valley winds in the Neckar valley are caused by the straight and deep valley, upstream of the VTs (Fig. 3.1).

Under unstable/neutral conditions, no pronounced wind direction can be distinguished in the wind roses at 400 m asl at the different sites (Fig. 5.17). In the Stuttgart basin, at its outflow into the Neckar valley and in the Neckar valley itself, northwesterly wind dominates, i.e. the wind direction distributions are similar to the ones at 685 m asl (Fig. 5.14c,d), indicating a downward mixing of momentum in the CBL due to convection, which masks the possible evolution of thermally driven slope and valley winds.

In summary, thermally driven winds are observed at all locations at 400 m asl under stable conditions, while the ambient wind at 685 m asl is similar at all sites. This means that a decoupling of the flow between 400 m asl and 685 m asl takes place. Under unstable/neutral conditions no

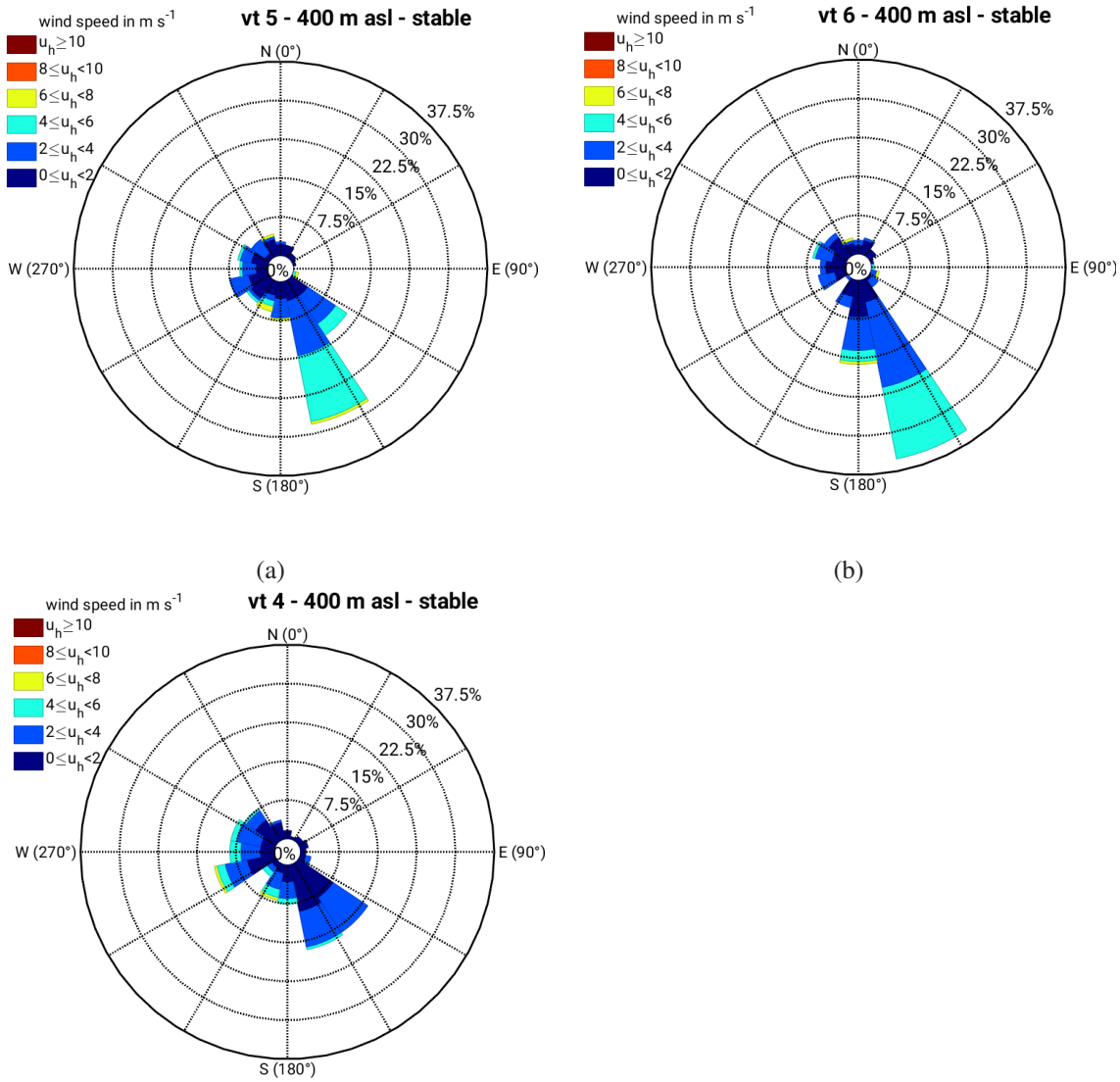

Figure 5.16: Wind roses at 400 m asl under stable conditions in the Neckar valley, at VTs 4 to 6 (c, a, b). Wind directions are divided into 16 sectors of 22.5° width and horizontal wind speed in 2 m s^{-1} bins. Data from 17 days are shown.

thermally driven wind can be distinguished in the measurement data. The flow at 685 m asl and 400 m asl is rather similar, which indicates a coupling between both levels.

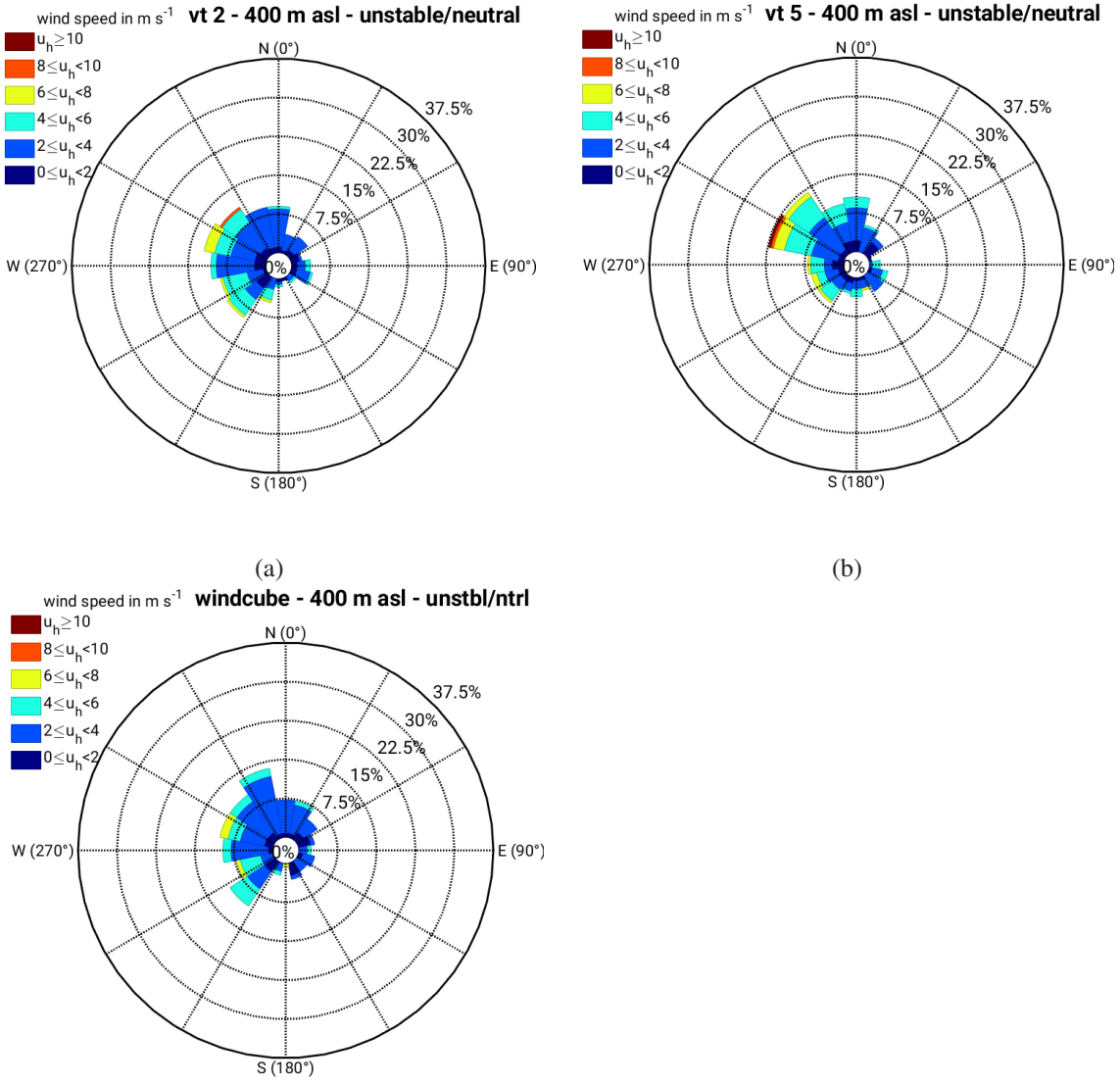

Figure 5.17: Wind roses at 400 m asl under unstable/neutral conditions at the Windcube (c) and VTs 2 and 5 (a, b). Wind directions are divided into 16 sectors of 22.5° width and horizontal wind speed in 2 m s^{-1} bins. Data from 17 days are shown.

5.2.4 Relationship between ambient and low-level wind

The regular occurrence of down-valley winds under stable stratification and a general decoupling of the flow between at higher and lower level is described in Sect. 5.2.3. As a wind rose only shows the distribution of the horizontal wind at one level, the relationship between the two levels cannot be investigated. This is done in the following using scatterplots of the wind direction at 400 m asl and 685 m asl. In Fig. 5.18 the relationship between the ambient and low-level wind directions under stable stratification are shown, taking into account the horizontal wind speed. At weak ambient wind ($\leq 4\,\mathrm{m\,s^{-1}}$, Figs. 5.18a,c,e) the low-level wind directions generally accumulate around the down-valley direction at all locations, regardless of the ambient wind direction. At the Windcube site (Figs.5.18a), the low-level wind directions lie mainly within an 90° sector around the down-valley direction. At VT 2 (Fig.5.18c), the low-level wind directions are more narrowly distributed around the down-valley direction than at the Windcube site, most occur within a sector of 60° around down-valley. Some values are also scattered around the diagonal and very few occur close to the up-valley wind direction. At VT 5 (Fig.5.18e), most wind directions at the lower level are centred narrowly around the down-valley direction, within a 45° sector. For ambient wind directions between 0° and 90°, low-level wind is sometimes clearly from the up-valley direction. At all three VTs, few values lie close to the diagonal, i.e. the low-level wind is similar to the ambient wind.

Overall, the decoupling of the flow at 400 m asl from the ambient wind at 685 m asl occurs independent of the ambient wind direction, as long as the ambient wind speed is relatively weak (($\leq 4\,\mathrm{m\,s^{-1}}$). This changes when considering the stronger ambient wind speeds as well (Figs. 5.18b,d,f). Although the majority of low-level winds are still down-valley, much more values are closer to the diagonal now. At the Windcube site (Fig. 5.18b), the low-level wind directions mainly are between southwest and north, in the sector between the down-valley direction and the diagonal. At VT 2 (Fig. 5.18d) the low-level wind directions under stronger ambient wind are mainly accumulated along a line parallel to but below the diagonal, i.e. the wind directions at low level are rotated cyclonically by around 45° compared to the ambient wind. Also at VT 5 (Fig. 5.18f), the low-level wind directions at higher ambient wind speeds accumulate at directions rotated around 45° cyclonically compared to the ambient wind. This is the case mainly at ambient wind directions between southwest (225°) and north (360°). For ambient wind directions between southeast (135°) and southwest, the low-level winds are still in the down-valley direction, even at stronger ambient wind. For stronger ambient winds from east-southeast (112.5°) to north, more up-valley winds occur. For ambient wind directions between east-southeast and southeast the low-level wind direction jumps by 180° between up-valley and down-valley direction.

The relationship between ambient and low-level wind directions at weak and strong ambient wind during stable stratification shows that thermally driven down-valley winds are favourable when the ambient wind is weak. This is likely related to stronger vertical wind shear with stronger ambient wind, which causes shear-induced turbulence and thus vertical mixing and momentum transport. This leads to similar wind directions at the higher and the lower level, with a cyclonic shift of the low-level wind. The cyclonic rotation of the low-level wind is caused by surface friction which decreases the wind speed and thereby the Coriolis force (Sect. 2.1). At weak ambient winds, the flow at the two layers is decoupled due to thermally driven circulations controlling the lower level

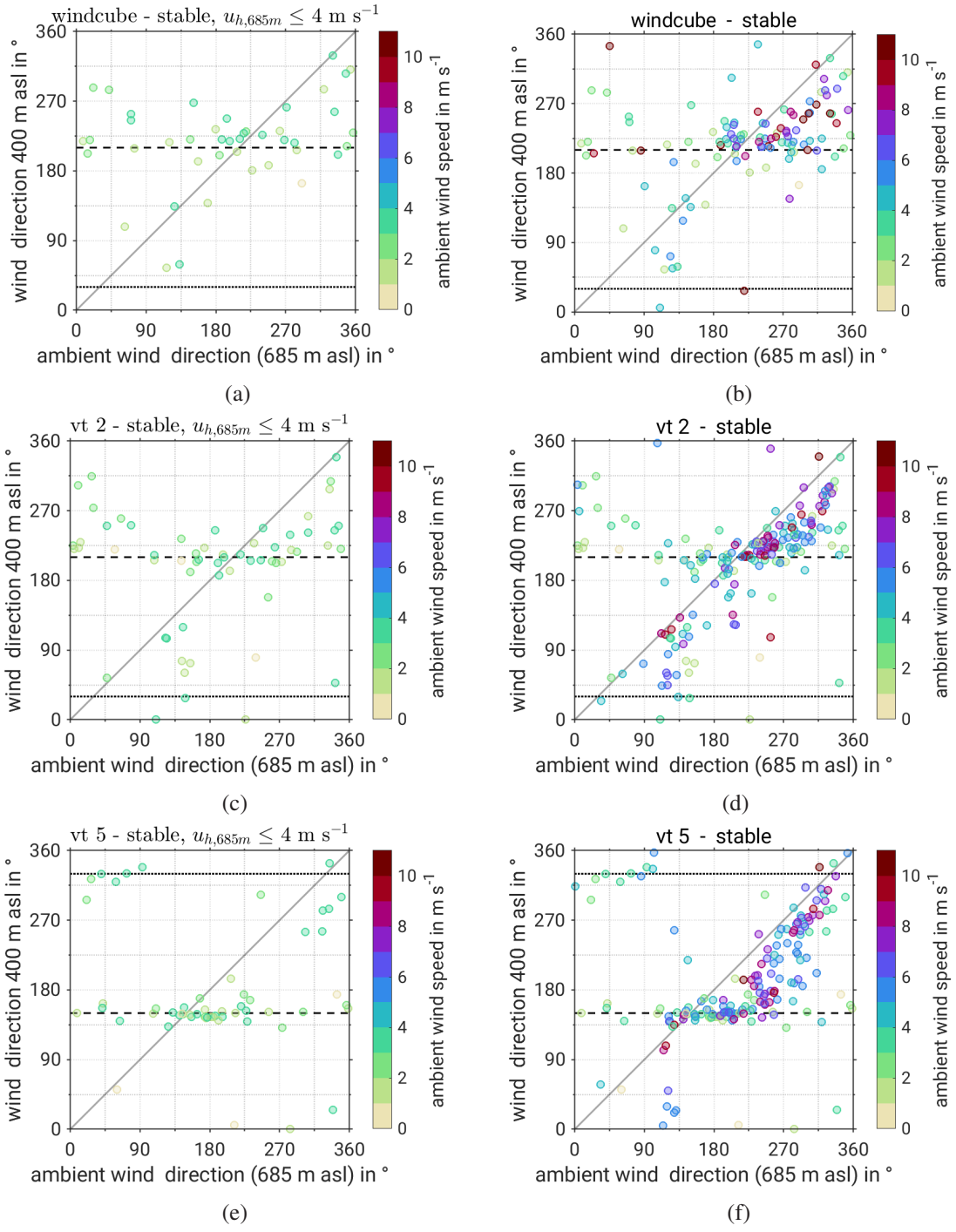

Figure 5.18: Relationship between the wind directions of ambient and low-level wind under stable conditions at the Windcube site (a,b), VT 2 (c,d) and VT 5 (e,f). The plots relate the ambient wind direction at 685 m asl on the x-axis to the wind at the topographically influenced level at 400 m asl on the y-axis. Horizontal wind speed of the ambient wind is denoted by the colours. The figures in the left column only display cases with ambient wind speed smaller than 4 m s^{-1}, the figures on the right show all cases. Dashed horizontal lines indicate the down-valley direction, dotted lines the up-valley direction. Markers on the grey diagonal line indicate that wind directions are the same at both levels.

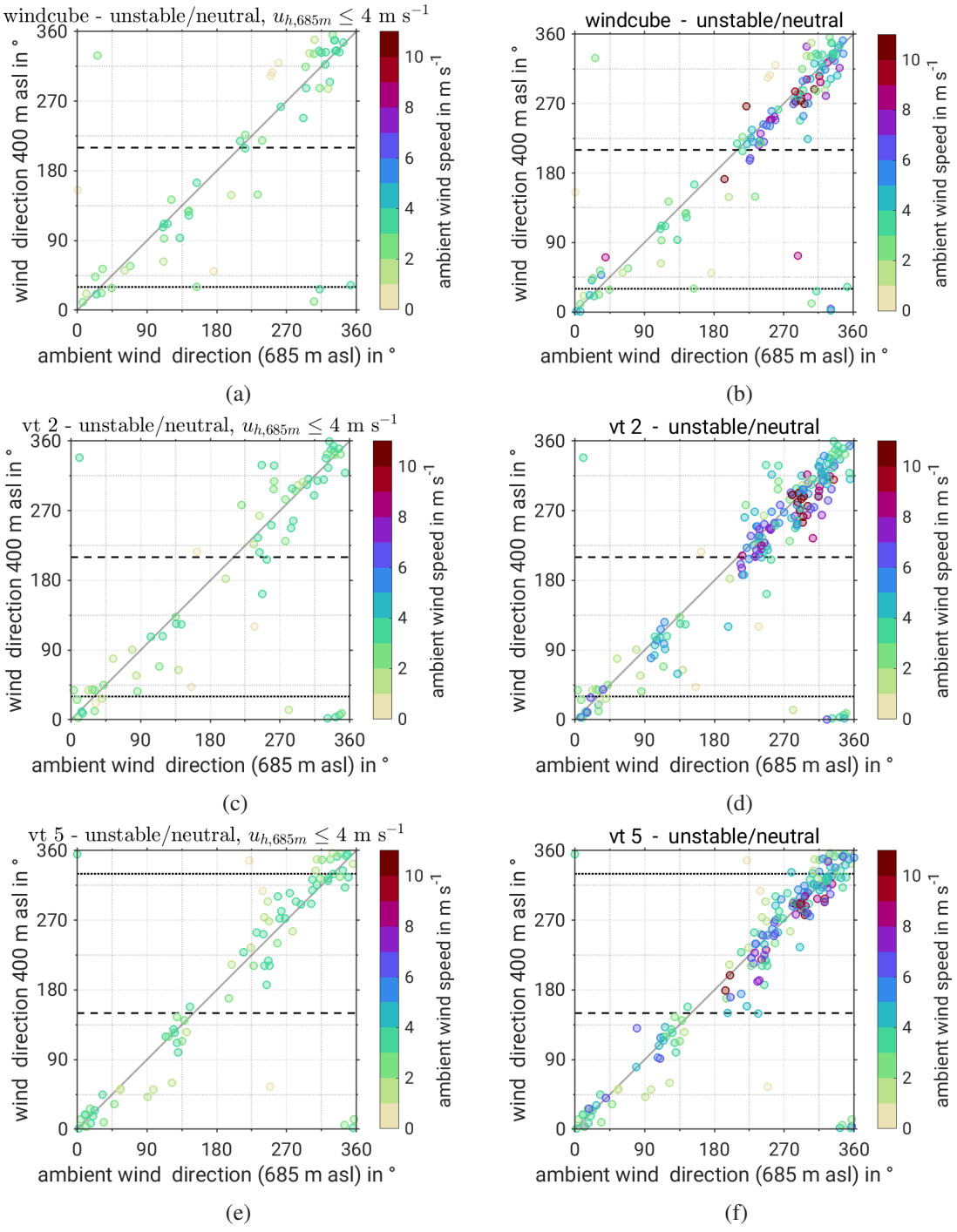

Figure 5.19: Relationship between the wind directions of ambient and low-level wind under unstable/neutral stratification at the Windcube (top), VT 2 (middle) and VT 5 (bottom). The plots relate the ambient wind direction at 685 m asl on the x-axis to the wind at the topographically influenced level at 400 m asl on the y-axis. Horizontal wind speed of the ambient wind is denoted by the colours. The figures in the left column only display cases with ambient wind speed smaller than 4 m s^{-1}, the figures on the right show all cases. Dashed horizontal lines indicate the down-valley direction, dotted lines the up-valley direction. Markers on the grey diagonal line indicate that wind directions are the same at both levels.

wind, but at stronger ambient winds the winds are coupled between the two layers due to shear induced turbulence. At VT 5 up-valley winds occur under stable conditions. These appear at a cyclonic rotation relative to the ambient wind as well, which means they are probably related to pressure driven channelling (Sect. 2.3).

To investigate the relationship between the ambient and low-level wind under unstable/neutral conditions, scatterplots for the same locations are shown in Fig. 5.19. At all locations and independent of the wind speed the values accumulate around the diagonal. The wind directions are similar at the low and higher level and no influence of the topography is visible. The similarity of the ambient and low-level winds shows that during unstable/neutral stratification momentum is well mixed within the CBL and the flow is coupled due to buoyancy induced turbulence, in agreement with the results from the wind roses analysis.

5.2.5 Dependency of the topographic influence on the bulk Richardson number

In the previous analysis, the static stability (i.e. the potential temperature difference) is considered for the analysis of the relationship between the low-level wind and the ambient wind. Under stable conditions, down-valley wind generally occurs for weak ambient wind speed, while for stronger ambient wind speed the flow in the valleys is coupled to the layer aloft. In order to investigate if this coupling under stable stratification is associated with dynamically produced turbulence, the relationship between the low-level and ambient wind direction is investigated using the bulk Richardson number (Sect. 2.1.4). The bulk Richardson number is calculated between 400 and 685 m asl using horizontal wind speed from the VTs and potential temperature from the MWR. The analysis is done separately for the Neckar valley at VT 5 and for the Stuttgart basin at VT 2 and the Windcube site.

Figure 5.20 displays the relationship between the two wind directions at 400 m asl and 685 m asl of VT 5 in the Neckar valley, with the colour indicating the bulk Richardson number. When the bulk Richardson number is negative, i.e. the stratification is statically unstable, low-level and ambient wind direction are quite similar, which agrees well with the relationship found for unstable/neutral conditions (Fig. 5.19). At bulk Richardson numbers larger than zero, which means statically stable stratification, the relationship between the wind directions depends on the strength of the static stability and the vertical wind shear.

For bulk Richardson numbers between 0 and 1.25, the wind directions are generally similar at the two height levels, but the low-level wind directions are rotated cyclonically and turn towards the down-valley direction. The low-level wind directions for bulk Richardson numbers between 1.25 and 2 are mainly down-valley, with some cases of up-valley wind when the ambient wind blows from 0° to 135° and a couple of outliers. When the bulk Richardson number is larger than 2 the low-level wind direction is down-valley, except for very few outliers.

As expected, the degree of coupling between the flow at low and higher levels depends on the value of the bulk Richardson number. For the conditions at VT 5, a critical value of the bulk Richardson number is around 1.25. For bulk Richardson numbers below 1.25, the low-level flow is coupled with the ambient flow. As for bulk Richardson numbers between 0 and 1.25 the at-

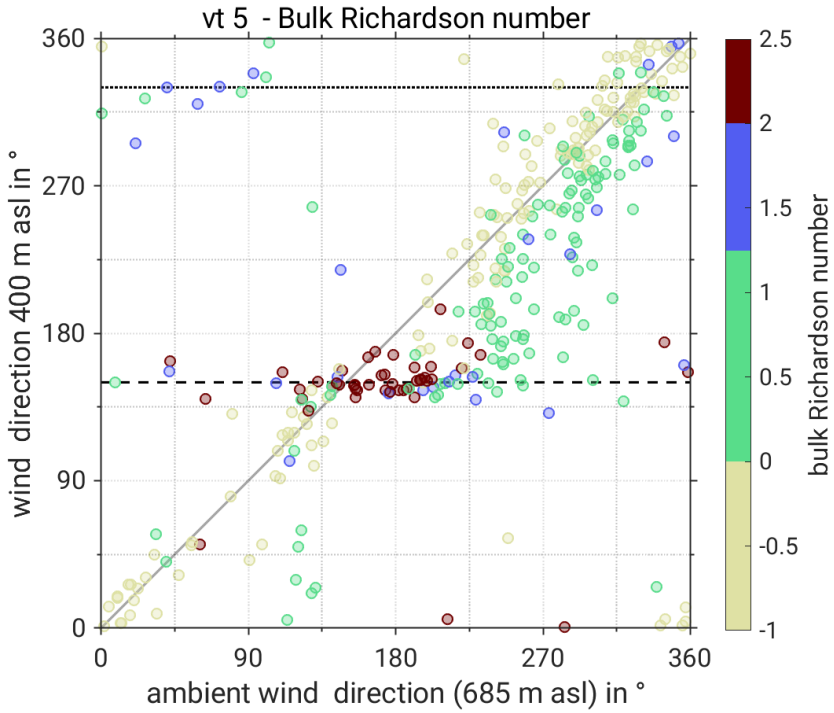

Figure 5.20: Relationship between the wind directions of ambient (x-axis) and low-level wind (y-axis) at VT 5. The colours denote the bulk Richardson number. The dashed horizontal line indicates the down-valley direction in the Neckar valley, the dotted line the up-valley direction. Markers on the grey diagonal line indicate that wind directions are the same at both levels.

mosphere is statically stable, shear-driven turbulence must cause the vertical mixing, for negative bulk Richardson numbers buoyancy-driven turbulence dominates the vertical mixing process. For bulk Richardson numbers between 0 and 2, influences from the ambient flow as well as from the topography are visible.

The few cases of up-valley wind occur for positive bulk Richardson numbers smaller than 2, while for bulk Richardson numbers greater than 2 only down-valley winds are observed. As described in Sect. 5.2.4 the up-valley winds are probably caused by pressure driven channelling (Sect. 2.3), which depends on the along-valley pressure gradient. If the synoptic pressure gradient is low, the ambient wind speed will also be low and vertical wind shear is likely to be small. Therefore, the bulk Richardson number becomes larger at low ambient wind speed (Eq. 2.3). The up-valley winds at VT 5 occur under statically stable stratification, i.e. an expected thermally induced pressure gradient points in the opposite direction to the synoptic pressure gradient. At low ambient wind speed the synoptic pressure gradient is small and can be exceeded by thermally induced pressure gradients. This might be the reason that no up-valley winds occur at bulk Richardson numbers greater than 2. In some cases also down-valley winds might be caused or enhanced by pressure driven channelling, but the visible effects on the wind direction relation in these cases are the same as for thermally driven down-valley winds and therefore the underlying forces cannot be distinguished.

For statically unstable conditions, no up-valley wind cases are observed as already described in Sects. 5.2.3 and 5.2.4. This indicates that under unstable conditions, the temperature and thus pressure gradients induced by the moderate terrain around Stuttgart are not sufficient for thermally

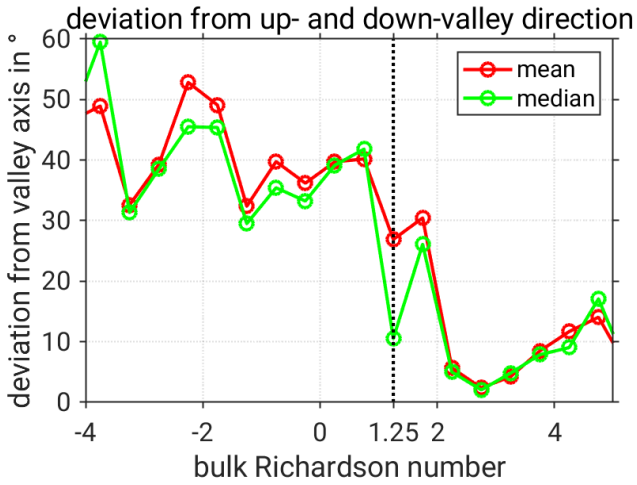

Figure 5.21: Deviation of the low-level wind from the valley axis depending on the bulk Richardson number. Mean and median of the absolute deviation from the valley axis (up- or down-valley direction) at VT 5 plotted against the bulk Richardson number in bins of 0.5. The critical bulk Richardson number found here is marked by the dotted line.

driven flows to develop. Instead turbulent mixing in the CBL couples the flow at low levels to the flow aloft by downward momentum transport.

Another more quantitative way of illustrating the influence of the topography on the flow in dependence of the bulk Richardson number is shown in Fig. 5.21. The figure shows the mean and median absolute deviation of the low-level wind from the valley axis (up- or down-valley direction). For negative bulk Richardson numbers and for values up to 1.25, the deviations from the valley axis show high values around 40°. At bulk Richardson numbers greater than 1.25 the deviations decrease and stay small at around 10° for values larger than 2. This means that the critical bulk Richardson number is higher than 0.25, which is a common value in literature and is often used (see Sect. 2.1.4). The reason for this is probably that the critical Richardson number of 0.25 is an empirically derived value for the gradient Richardson number. The bulk Richardson number used here is an approximation of the gradient Richardson number and is calculated from differences over two layers which are 285 m apart, instead of local gradients (Eq. 2.3). Therefore, the critical value for the gradient Richardson number is not necessarily the same for the bulk Richardson number. The deviations from the valley axis in Fig. 5.21 suggest that here the critical bulk Richardson number, above which the flow is dynamically stable, is around 1.25.

The dependence of the wind direction relationship on the bulk Richardson number at VT 2 and the Windcube (Fig. 5.22) is generally similar to the the observations at VT 5 in the Neckar valley. At negative Richardson numbers ambient and low-level wind direction are quite similar, i.e. winds are coupled between the two layers by buoyancy driven turbulence. For positive bulk Richardson numbers the low-level wind directions approach the down-valley direction. For bulk Richardson numbers between 0 and 1.25 the low-level wind directions are still similar to the ambient wind directions, but rotated cyclonically and begin to turn to the down-valley direction, i.e. influences from the valley are visible, but downward momentum transport is the dominating influence. For bulk Richardson numbers greater than 1.25 the majority of the low-level wind directions is down-valley, independent from the ambient wind direction, which indicates the abundance of thermally

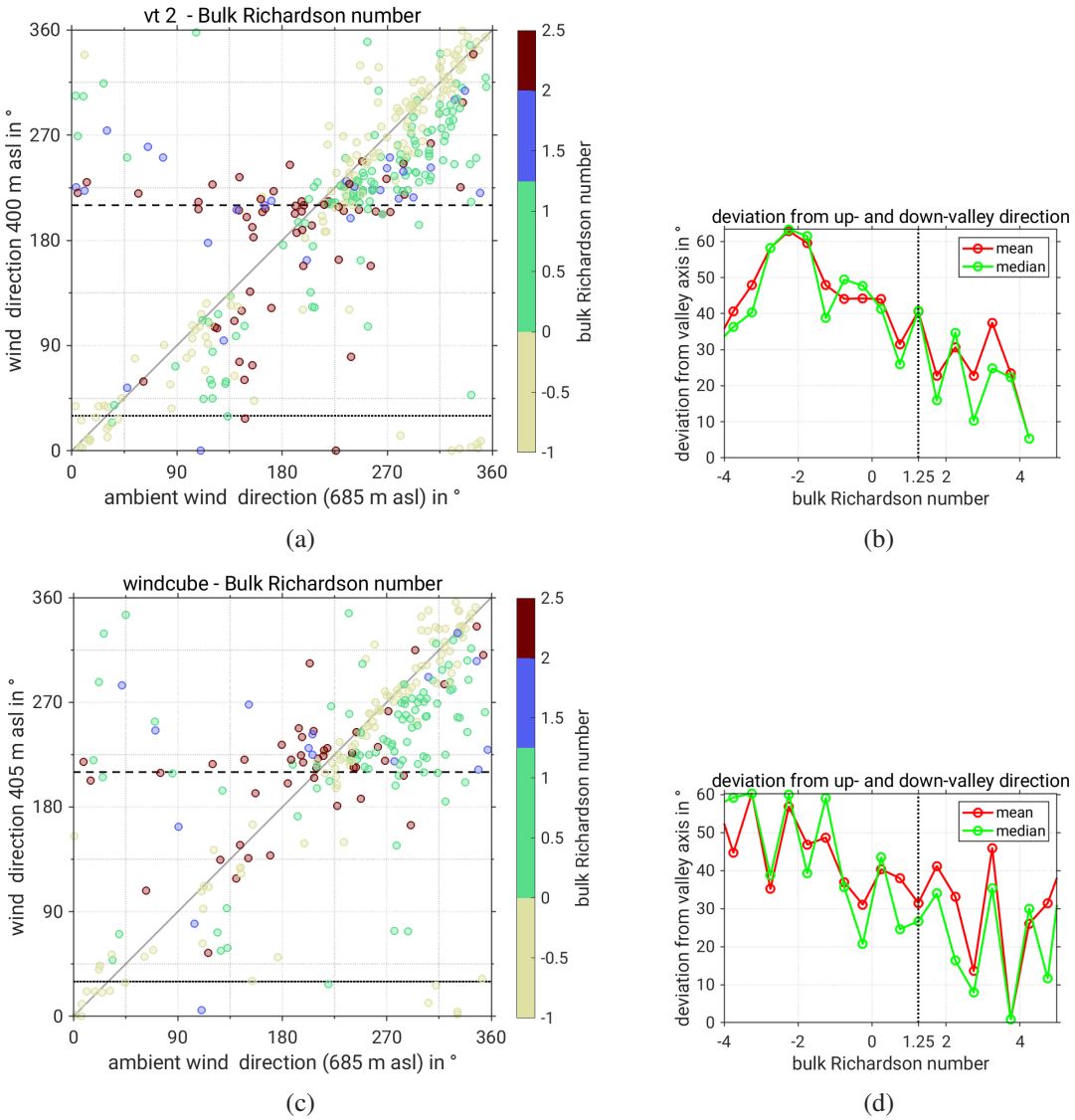

Figure 5.22: Dependence of the low-level wind on the Richardson number at VT 2 (a,b) and the Windcube (c,d) site in the Stuttgart basin. The relationship between ambient and low-level wind is displayed on the left, with the dashed and dotted line denoting approximate down- and up-valley direction. The mean and median of the absolute deviation from the valley axis is displayed on the right.

driven down-valley winds at higher bulk Richardson numbers and a decoupling of the flow between the two levels. However, although the major part of the low-level wind directions are down-valley, many values deviate from the down-valley direction strongly. This is probably caused by the topography, as the more roundly shaped Stuttgart basin does not channel the flow as well as the Neckar valley (see Fig. 3.1). At the location of VT 2, at the opening of the basin, the flow might also be influenced by the flow in the Neckar valley. At both sites no up-valley winds are observed, which is probably also related to the topography. The up-valley winds in the Neckar valley are likely to be caused by pressure driven channelling, which occurs mainly in straight valleys (Sect. 2.3). The round shape of the Stuttgart basin makes pressure driven channelling unlikely.

The deviation of the low-level wind from the approximate valley axis in the Stuttgart basin is displayed in Fig. 5.22 for VT 2 (b) and the Windcube (d). As expected the deviation is large

for negative bulk Richardson numbers and decreases for positive values. However, for positive Richardson numbers the deviations from the valley axis are still much larger than at VT 5 in the Neckar valley (Fig. 5.21). In general the dependence of the low-level wind direction on the bulk Richardson number in the Stuttgart basin is much less clear than in the Neckar valley. A critical value for the bulk Richardson number therefore cannot be clearly defined for the Stuttgart basin. However, the relationship of the low-level wind to the ambient wind (Fig. 5.22a, 5.22c) indicates that for bulk Richardson numbers of around 1.25 the dominating mechanism controlling the low-level flow changes from downward momentum transport to thermally driven pressure gradients. Therefore, the critical Richardson number in the Stuttgart basin is assumed to be around 1.25, and is thus similar to the one for the Neckar valley.

6 Summary and conclusions

In this thesis, the flow in the ABL over Stuttgart, a city in complex terrain, is investigated in detail, using profiles of the horizontal wind retrieved from dual-Doppler lidar measurements, so-called virtual towers (VTs). The orography of the investigation area is characterised by the Stuttgart basin which is joined by the Nesenbach valley in the southwest and opens to the larger Neckar valley in the northeast. The mean ridge height is at around 520 m asl, i.e. around 250 m above the valley bottoms. The wind field in the ABL is crucial for urban climate and air pollution, as it controls the transport of heat, moisture, aerosols and trace gases. In particular in cities in complex terrain, like Stuttgart, the interaction of processes on different scales, ranging from microscale flow disturbance of single buildings over topographically induced mesoscale circulations to the large-scale synoptic flow determines the conditions and evolution of the urban ABL. Although Stuttgart is well known for bad air quality issues, detailed observational studies of the wind field in the urban ABL in and around Stuttgart are still missing. This is why a comprehensive measurement campaign was conducted in summer 2017 within the framework of the $[UC]^2$ project. Information on horizontal wind profiles are retrieved from 6 VTs with 68 measurement heights between 30 m to 2000 m above ground level. These data are used to identify characteristic flow patterns which occur in the urban ABL of Stuttgart, to assess how the flow is affected by the topography, and how it depends on large scale wind and atmospheric stratification. Three VTs each were set up along cross sections through the 2 km wide Neckar valley and the narrower opening of the Stuttgart basin to the Neckar valley. Additionally a third profiling Doppler lidar was measuring wind profiles in the Stuttgart basin and a MWR was used to obtain information on atmospheric stratification.

Three objectives have been addressed in this study, with one being more technical:

1. The first objective is the proof of concept of the VT method in complex urban terrain and to find out how the data has to be processed to retrieve reliable data. Before the lidar data could be used for the analysis of the horizontal wind field, an intense processing and quality control is conducted. First, the radial velocity measurements for each lidar corresponding to VTs are selected by the lidar beam direction and the distance from the devices. Secondly, the radial velocity data at the VTs are filtered in three ways: by setting a maximum threshold for radial velocity to remove unrealistically high values, by applying a minimum signal-to-noise ratio threshold to remove data with low backscatter signal, and outliers are rejected using a median absolute deviation threshold. 19 % of the raw data are filtered out by these filtering steps. Thirdly, the radial velocities are averaged over measurement intervals and horizontal wind is calculated. To increase the quality of the horizontal wind values only measurements from intervals with a minimum data availability are taken into account, which leads to the

removal of additional 11 % of the data. The resulting wind profiles show good agreement with other wind measurements of a profiling lidar and radiosondes.

2. The second objective is, to determine the flow characteristics in the ABL near Stuttgart and to investigate how they are influenced by the orography. To get a detailed view of the flow patterns, which can be expected in the ABL, a case study under fair weather conditions is analysed. During daytime a CBL forms up the highest measurement heights, in which the horizontal wind is rather constant with height. After sunset, a surface inversion develops reaching up to 700 m above the valley bottoms. The flow above ridge height is rather homogeneous throughout the investigation area, while pronounced spatial differences occur below the ridge height due to the impact of the topography. Down-valley winds are observed in the Stuttgart basin and in the Neckar valley and a weak outflow occurs at the opening of the Stuttgart basin into the Neckar valley. Above the ridge height an LLJ forms in the second half of the night. This means that during nighttime, the flow below the ridge height is decoupled from the flow aloft and induced by the topography, while during the day coupling throughout the CBL is observed.

3. The third objective is to investigate how the flow depends on the large-scale wind and the atmospheric stratification. Motivated by the results of the case study, the topographic influence on the horizontal wind field is investigated statistically, using all available VT data, combined with temperature profiles from the MWR. The height dependence of the topographic influence is investigated based on the horizontal variability of the wind in the area. To get an objective measure of the horizontal variability of the wind, profiles of spatial standard deviations are calculated. The larger the spatial standard deviation is, the larger is the horizontal variability of the wind field. Using spatial standard deviations, it is found that during nighttime under stable stratification the topographic influences are strongest below the ridge height and quickly decrease with height above the ridge height. During daytime, under convective conditions, no considerable topographic influences could be observed, due to vertical mixing in the CBL. Based on this analysis two height levels where chosen for the further investigation of the topographic influence: a lower level below ridge height, where the wind is strongly topographically influenced (400 m asl), and a level at higher altitude where the wind reflects the large scale flow, which is controlled by synoptic conditions and nearly unaffected by the topography (685 m asl).

   Wind roses are analysed for these two layers at all locations distinguishing between stable and unstable/neutral conditions. In the lower level under stable conditions, thermally driven down-valley winds are common at all locations. The VTs at the sides of the valleys show some impacts from the slopes. Under neutral and unstable stratification no considerable topographic influences could be recognised in the CBL. Comparing the wind directions at the two heights shows that the thermally driven down-valley winds under stable stratification mainly occur when the ambient wind is small. When the ambient wind is stronger, shear induced turbulence likely leads to enhanced vertical mixing of momentum and coupling of the low-level and ambient wind. A few cases with up-valley wind occur in the Neckar valley under stable conditions, probably caused by pressure driven channelling with northerly to

easterly ambient winds. Under unstable and neutral stratification no major influences of the topography could be observed. Most of the time wind directions are similar at ambient and low level, as momentum in the CBL is well mixed.

The relationship between the low-level and ambient wind direction strongly depends on the bulk Richardson number. For the Neckar valley at VT 5 it is shown, that a critical bulk Richardson number is 1.25. For bulk Richardson numbers smaller than 1.25 the flow is coupled by turbulence. For negative bulk Richardson numbers the turbulence is buoyancy-induced, whereas for positive values shear-induced turbulence causes the coupling. For bulk Richardson numbers larger than 1.25 the flow is decoupled between low-level and ambient wind. At the low level, mainly down-valley winds occur independent from the ambient wind direction, besides of some cases of pressure driven up-valley wind. In the Stuttgart basin at the Windcube site and at the basin opening at VT 2, a dependence of the coupling on the bulk Richardson number is observed as well. Probably linked to the topography of the basin, the dependence is less clear than in the Neckar valley. Nevertheless, a critical value of the bulk Richardson number seems to be similar as in the Neckar valley.

In this thesis it is shown that VTs from dual-Doppler lidar measurements are a suitable method to investigate the horizontal wind field over complex terrain. By positioning several VTs at locations of interest in an investigation area, it is possible to analyse the evolution of the horizontal wind field spatially and temporally. The possibilities of VT method are only limited by geometric limitations of the lidars and enable measurements in the ABL in regions that are difficult to access with traditional in situ measurements, like over urban terrain. Thermally driven down-valley winds are found to be a common phenomenon in the area of Stuttgart during stable stratification. Down-valley winds at the Nesenbach valley and outflow at the opening of the Stuttgart basin result in ventilation of the basin. Ventilation of the Stuttgart basin is likely to have a considerable influence on the air quality in the city by removing pollutants. The effects of the ventilation by down-valley winds on the air quality could be further examined by combining the VT measurements with aerosol or pollutant measurements to estimate the relevance of outflow situations for the urban climate.

Bibliography

Adler, B., 2014: Boundary-layer processes producing mesoscale water-vapour variability over a mountainous island. Ph.D. thesis.

Adler, B., O. Kiseleva, N. Kalthoff, and A. Wieser, 2019: Comparison of convective boundary layer characteristics from aircraft and wind lidar observations. *Journal of Atmospheric and Oceanic Technology*, **36 (7)**, 1381–1399.

Allwine, K. J., J. H. Shinn, G. E. Streit, K. L. Clawson, and M. Brown, 2002: Overview of urban 2000: A multiscale field study of dispersion through an urban environment. *Bulletin of the American Meteorological Society*, **83 (4)**, 521–536.

Barlow, J. F., 2014: Progress in observing and modelling the urban boundary layer. *Urban Climate*, **10**, 216–240.

Barr, K., 2008: *WindTracer WTX - Installation and Maintenance Manual*. Lockheed Martin.

Bingöl, F., J. Mann, and D. Foussekis, 2009: Conically scanning lidar error in complex terrain. *Meteorologische Zeitschrift*, **18 (2)**, 189–195.

Blackadar, A. K., 1957: Boundary layer wind maxima and their significance for the growth of nocturnal inversions. *Bulletin of the American Meteorological Society*, **38 (5)**, 283–290.

Calhoun, R., R. Heap, M. Princevac, R. Newsom, H. Fernando, and D. Ligon, 2006: Virtual towers using coherent doppler lidar during the joint urban 2003 dispersion experiment. *Journal of Applied meteorology and climatology*, **45 (8)**, 1116–1126.

Choukulkar, A., W. A. Brewer, S. P. Sandberg, A. Weickmann, T. A. Bonin, R. M. Hardesty, J. K. Lundquist, R. Delgado, G. V. Iungo, R. Ashton, et al., 2017: Evaluation of single and multiple doppler lidar techniques to measure complex flow during the xpia field campaign. *Atmospheric Measurement Techniques*, **10 (1)**.

Collier, C. G., F. Davies, K. E. Bozier, A. R. Holt, D. R. Middleton, G. N. Pearson, S. Siemen, D. V. Willetts, G. J. Upton, and R. I. Young, 2005: Dual-doppler lidar measurements for improving dispersion models. *Bulletin of the American Meteorological Society*, **86 (6)**, 825–838.

Crewell, S. and U. Löhnert, 2007: Accuracy of boundary layer temperature profiles retrieved with multifrequency multiangle microwave radiometry. *IEEE Transactions on Geoscience and Remote Sensing*, **45 (7)**, 2195–2201.

Damian, T., 2012: Messung des windprofils an virtuellen masten unter anwendung des dual-doppler verfahrens. Diploma thesis.

Damian, T., A. Wieser, K. Träumner, U. Corsmeier, and C. Kottmeier, 2014: Nocturnal low-level jet evolution in a broad valley observed by dual doppler lidar. *Meteorologische Zeitschrift*, **23 (3)**, 305–313.

Drechsel, S., G. J. Mayr, M. Chong, M. Weissmann, A. Dörnbrack, and R. Calhoun, 2009: Three-dimensional wind retrieval: Application of muscat to dual-doppler lidar. *Journal of Atmospheric and Oceanic Technology*, **26 (3)**, 635–646.

Grund, C. J., R. M. Banta, J. L. George, J. N. Howell, M. J. Post, R. A. Richter, and A. M. Weickmann, 2001: High-resolution doppler lidar for boundary layer and cloud research. *Journal of Atmospheric and Oceanic Technology*, **18 (3)**, 376–393.

imk-radar.de, 2019: Radarbilder Archiv, Radar-Info. `https://www.imk-radar.de/Radarbilder/viewer/archiv-browser-v2.html`.

Kalthoff, N., B. Adler, A. Wieser, M. Kohler, K. Träumner, J. Handwerker, U. Corsmeier, S. Khodayar, D. Lambert, A. Kopmann, et al., 2013: Kitcube–a mobile observation platform for convection studies deployed during hymex. *Meteorologische Zeitschrift*, **22 (6)**, 633–647.

Kalthoff, N., H.-J. Binder, M. Kossmann, R. Vögtlin, U. Corsmeier, F. Fiedler, and H. Schlager, 1998: Temporal evolution and spatial variation of the boundary layer over complex terrain. *Atmospheric Environment*, **32 (7)**, 1179–1194.

Kossmann, M., R. Vögtlin, U. Corsmeier, B. Vogel, F. Fiedler, H.-J. Binder, N. Kalthoff, and F. Beyrich, 1998: Aspects of the convective boundary layer structure over complex terrain. *Atmospheric Environment*, **32 (7)**, 1323–1348.

Lareau, N. P., E. Crosman, C. D. Whiteman, J. D. Horel, S. W. Hoch, W. O. Brown, and T. W. Horst, 2013: The persistent cold-air pool study. *Bulletin of the American Meteorological Society*, **94 (1)**, 51–63.

Löhnert, U. and S. Crewell, 2003: Accuracy of cloud liquid water path from ground-based microwave radiometry 1. dependency on cloud model statistics. *Radio Science*, **38 (3)**.

Löhnert, U., D. Turner, and S. Crewell, 2009: Ground-based temperature and humidity profiling using spectral infrared and microwave observations. part i: Simulated retrieval performance in clear-sky conditions. *Journal of Applied Meteorology and Climatology*, **48 (5)**, 1017–1032.

Machiwal, D. and M. K. Jha, 2012: *Hydrologic time series analysis: theory and practice*. Springer Science & Business Media, Dordrecht, 301 pp.

Maronga, B., G. Gross, S. Raasch, S. Banzhaf, R. Forkel, W. Heldens, F. Kanani-Sühring, A. Matzarakis, M. Mauder, D. Pavlik, et al., 2019: Development of a new urban climate model based on the model palm–project overview, planned work, and first achievements. *Meteorologische Zeitschrift*, **28 (2)**, 105–119.

Newman, J. F., T. A. Bonin, P. M. Klein, S. Wharton, and R. K. Newsom, 2016: Testing and validation of multi-lidar scanning strategies for wind energy applications. *Wind Energy*, **19 (12)**, 2239–2254.

Newsom, R. K., D. Ligon, R. Calhoun, R. Heap, E. Cregan, and M. Princevac, 2005: Retrieval of microscale wind and temperature fields from single-and dual-doppler lidar data. *Journal of applied meteorology*, **44 (9)**, 1324–1345.

Pauscher, L., N. Vasiljevic, D. Callies, G. Lea, J. Mann, T. Klaas, J. Hieronimus, J. Gottschall, A. Schwesig, M. Kühn, et al., 2016: An inter-comparison study of multi-and dbs lidar measurements in complex terrain. *Remote Sensing*, **8 (9)**, 782.

Rose, T., S. Crewell, U. Löhnert, and C. Simmer, 2005: A network suitable microwave radiometer for operational monitoring of the cloudy atmosphere. *Atmospheric Research*, **75 (3)**, 183–200.

Rothermel, J., C. Kessinger, and D. L. Davis, 1985: Dual-doppler lidar measurement of winds in the jaws experiment. *Journal of Atmospheric and Oceanic Technology*, **2 (2)**, 138–147.

Röhner, L. and K. Träumner, 2013: Aspects of convective boundary layer turbulence measured by a dual-doppler lidar system. *Journal of Atmospheric and Oceanic Technology*, **30 (9)**, 2132–2142.

Schädler, G. and A. Lohmeyer, 1996: *Kaltluft-und Windfeld-Berechnungen für den Raum Stuttgart im Zusammenhang mit der Planung für das Projekt "Stuttgart 21"*. Landeshauptstadt Stuttgart, Amt für Umweltschutz, Abt. Stadtklimatologie.

Scherer, D., F. Ament, S. Emeis, U. Fehrenbach, B. Leitl, K. Scherber, C. Schneider, and U. Vogt, 2019a: Three-dimensional observation of atmospheric processes in cities. *Meteorologische Zeitschrift*, **28 (2)**, 121–138.

Scherer, D., F. Antretter, S. Bender, J. Cortekar, S. Emeis, U. Fehrenbach, G. Gross, G. Halbig, J. Hasse, B. Maronga, S. Raasch, and K. Scherber, 2019b: Urban climate under change [uc]^2–a national research programme for developing a building-resolving atmospheric model for entire city regions. *Meteorologische Zeitschrift*, **28 (2)**, 95–104.

Stawiarski, C., K. Träumner, C. Knigge, and R. Calhoun, 2013: Scopes and challenges of dual-doppler lidar wind measurements–an error analysis. *Journal of Atmospheric and Oceanic Technology*, **30 (9)**, 2044–2062.

Steyn, D. G., J. Bottenheim, and R. Thomson, 1997: Overview of tropospheric ozone in the lower fraser valley, and the pacific'93 field study. *Atmospheric Environment*, **31 (14)**, 2025–2035.

Steyn, D. G., S. F. J. De Wekker, M. Kossmann, and A. Martilli, 2013: Boundary layers and air quality in mountainous terrain. *Mountain Weather Research and Forecasting: Recent Progress and Current Challenges*, Chow, F. K., S. F. De Wekker, and B. J. Snyder, Eds., Springer Netherlands, Dordrecht, 261–289.

Stull, R. B., 1988: *An introduction to boundary layer meteorology*, Vol. 2. Kluwer Academic Publishers, Dordrecht, 666 pp.

Träumner, K., T. Damian, C. Stawiarski, and A. Wieser, 2015: Turbulent structures and coherence in the atmospheric surface layer. *Boundary-Layer Meteorology*, **154 (1)**, 1–25.

Vogt, U., 1999: *Messungen der Kaltluftströme und Luftverunreinigungs-Vertikalprofile im Plangebiet "Stuttgart 21": Zusammenfassung der Ergebnisse der ersten Messkampagne*. Landeshauptstadt Stuttgart, Amt für Umweltschutz, Abt. Stadtklimatologie.

Werner, C., 2005: Doppler wind lidar. *Lidar: Range-Resolved Optical Remote Sensing of the Atmosphere*, Weitkamp, C., Ed., Springer New York, New York, 325–354.

wetter3.de, 2018a: Archiv-Version des Animationstools (GFS). `http://www1.wetter3.de/archiv_gfs_dt.html`, accessed: 2018-09-21.

———, 2018b: DWD Analyse-Archiv. `http://www1.wetter3.de/archiv_dwd_dt.html`, accessed: 2018-09-21.

Whiteman, C. D., 2000: *Mountain meteorology: fundamentals and applications*. Oxford University Press, New York, 355 pp.

Whiteman, C. D. and J. C. Doran, 1993: The relationship between overlying synoptic-scale flows and winds within a valley. *Journal of Applied Meteorology*, **32 (11)**, 1669–1682.

Acknowledgement

First of all, I would like to thank my supervisor Bianca Adler for her excellent support and mentoring, always taking time for discussions on new results or further proceeding. Also I am very grateful to Norbert Kalthoff for his supervision and helpful advice.
I would like to thank my advisor Prof. Christoph Kottmeier for his valuable feedback and new scientific suggestions. Also I am thankful to my second advisor Prof. Michael Kunz for critical, but constructive feedback and showing room for further improvement.
I would like to thank the members of the working group Land Surfaces and Boundary Layer, and the technical staff, for support and conduction of the measurements used for this thesis.
Many thanks to my fellow students, especially to Felix, Christoph, Freia and Sera for various discussions and mental support.
Last but not at all least, I would like to thank my Family. Throughout my studies I experienced great support from my parents and I am deeply grateful for this. Finally I am deeply grateful to my fiancée, for supporting and encouraging me at all times.

Declaration of Authorship

I hereby declare that the thesis submitted is my own unaided work. All direct or indirect sources used are acknowledged as references. I am aware that the thesis in digital form can be examined for the use of unauthorized aid and to determine wether the thesis as a whole or parts incorporated in it may be deemed as plagiarism.
For the comparison of my work with existing sources I agree that it shall be entered in a database where it shall also remain after examination, to enable comparison with future theses submitted. Further rights of reproduction and usage, however, are not granted here. This paper was not previously presented to another examination board and has not been published.

Karlsruhe, 28 August 2019

Niklas Wittkamp